Optically Excited and Multiply Charged Semiconductor Quantum Dots Modeled by Empirical Tight Binding

DISSERTATION

Presented in Partial Fulfillment of the Requirements for

the Degree Doctor of Philosophy in the

Graduate School of The Ohio State University

By

Seungwon Lee, B.S., M.S.

* * * * *

The Ohio State University

2002

Dissertation Committee:

Prof. John. W. Wilkins, Adviser

Prof. Paul R. Berger

Prof. Eric Braaten

Prof. David Stroud

Approved by

Adviser
Department Of Physics

© Copyright by

Seungwon Lee

2002

ABSTRACT

The effects of quantum confinement and many-body interactions on the optical and transport properties of semiconductor quantum dots are investigated within the framework of the empirical tight-binding model. The exciton levels of optically excited dots and the electron and hole addition energies of multiply charged dots are described by incorporating many-body interactions, electron-hole dipole moments, and polarization of the dot environment into the tight-binding model. We choose Si quantum dots as an example of an indirect gap semiconductor, and InAs and CdSe dots as examples of typical III-V and II-VI direct-gap semiconductors. To mimic chemically synthesized quantum dots, the dot structure is modeled as a spherical and unstrained crystallite with the surface dangling bonds truncated.

Electron and hole single-particle energies are significantly improved by optimizing tight-binding parameters and by extending tight-binding basis orbitals to give the best description of the lowest conduction and the highest valence bands. For Si dots, the exciton gaps calculated with the parameters, optimized to give the good effective mass of the lowest conduction band near its minimum, agree well with experimental gaps. For InAs dots, the inclusion of spin-orbit coupling and d orbitals in a single-particle Hamiltonian increases a single-particle gap as much as 0.2 eV, yielding better agreement with experiments in terms of several low-lying bright-exciton energies and addition energies.

Quantitatively, tight-binding treatments of Coulomb interactions are reliable for dots with radii larger than 15–20 Å. In direct-gap semiconductor InAs and CdSe quantum dots, the exchange interaction can be long-ranged, extending over the whole dot when there is no local orthogonality between the electron and hole wave functions. In contrast, for Si quantum dots the extra phase factor due to the indirect gap effectively limits the range to about 15 Å, independent of the dot size.

For optically excited quantum dots, calcualted exciton gaps of Si and CdSe dots with radius 10–40 Å and the three lowest bright exciton energies of InAs dots with radius larger than 20 Å agree well with photoluminescence experiments. For multiply charged dots, calculated low-lying addition energies of InAs dots with radius 10–40 Å are in good agreement with scanning tunneling miscroscope experiments.

Dedicated to my family

ACKNOWLEDGMENTS

Keep away from people who try to belittle your ambitions. Small people always do that, but the really great make you feel that you, too, can become great.

-Mark Twain

John Wilkins and Lars Jönsson deserve much credit for what I have accomplished through the years of my graduate studies. I thank John and Lars for their helpful advice and valuable discussions. I also would like to thank my collaborators, Garnett Bryant, Jeongnim Kim, and Gerhard Klimeck, for their valuable input into this work.

I would like to thank the following for their help and encouragement: Sanghun An, Junjik Bae, Selemon Bekele, Eric Braaten, Stuart Brand, Jeehyun Choi, Alex Choy, Kathy Coen, Daniel Corciorva, Saeid Davatolhagh, Adom Durst, Kent Fisher, Ernest Fong, Avik Ghosh, Dan Goldbaum, Richard Hennig, Jiangping Hu, Yungok Im, Yu Jia, Youngmin Kim, Seiyon Kim, Wonpil Lee, Hyungsik Lim, Seongyeon Lim, Ivan Medvedev, Dianne Milanovich, Tatyana Mishurova, Aditi Mitra, Joel Moore, Niru Nahar, Christopher Neu, Karen Nippert, Shelley Palmer, Kibok Park, Arun Ravindran, David Richie, Roger Sakhel, Tatiana Stantcheva, David Stroud, Jennifer Tate, Nigussie Tirfessa, Dallas Trinkle, Anna Valeva, Jordan Vincent, Dennis Walker, Casey Watson, Jiangeng Xue, Xinguang Zhu, Fenghua Zong, Yury Zuev.

I acknowledge the financial support of the NSF, DOE, UCSB ITP Graduate Fellowship, and OSU Presidential Fellowship. I also acknowledge the computational support of the NCSA, NERSC, and OSC supercomputer centers. I would like to thank the hospitality of the UCSB ITP during year 2000 and the UIUC NCSA during year 2001-2002.

Finally, I thank the endless support of my family: my husband Kent Harbaugh, my mom Chunja Park, my dad Sujeong Lee, my sisters Jiwon Lee and Bowon Lee, my mom-in-law Judianne Harbaugh, and my sisters-in-law Joellen Fone and Samantha Jacobs.

VITA

2 April 1973	Born in Namwon, Korea
February 1995	B.S. Physics Education, Seoul National University, Korea
February 1997	M.S. Physics, Seoul National University, Korea
June 2001	M.S. Physics, Ohio State University

PUBLICATIONS

Research Publications

"Electron-hole correlations in semiconductor quantum dots with tight-binding wave functions," Seungwon Lee, Lars Jönsson, John W. Wilkins, Garnett W. Bryant and Gerhard Klimeck, Physical Reivew B **63**, 195318 (2001).

"Electron-hole correlations and optical excitonic gaps in quantum-dot quantum-wells: Tight-binding approach," Rui-Hua Xie, Garnett W. Bryant, Seungwon Lee and W. Jaskolski, Physical Review B **65**, 235306 (2002).

FIELDS OF STUDY

Major Field: Physics

TABLE OF CONTENTS

Page

Abstract ii

Dedication iv

Acknowledgments v

Vita vii

List of Tables x

List of Figures xii

Chapters:

1. Introduction 1

   1.1 Quantum Dots 4
   1.2 Experimental Approaches 8
      1.2.1 Optical Excitation 8
      1.2.2 Electrical Excitation 9
   1.3 Theoretical Approaches 11
      1.3.1 Effective-Mass Approximation 11
      1.3.2 Pseudo-Potential Model 13
      1.3.3 Tight-Binding Model 14

2. Single-Particle Levels of Quantum Dots 16

   2.1 Single-Particle Hamiltonian 17
   2.2 Single-Particle Energies and Wave Functions 25

3. Optically Excited Quantum Dots 29

3.1 Electron-Hole Hamiltonian 31
3.2 Dielectric Function 35
3.3 Coulomb Interactions 36
3.3.1 Coulomb and Exchange Integrals 38
3.3.2 Choice of Basis Orbitals 45
3.3.3 Reliability of Coulomb Interaction Calculations 46
3.4 Exchange Interactions 51
3.5 Oscillator Strengths 57
3.6 Exciton Levels 63
3.6.1 Si Quantum Dots 64
3.6.2 CdSe Quantum Dots 65
3.6.3 InAs Quantum Dots 68
3.7 Discussion 80

4. Multiply Charged Quantum Dots 84

4.1 Model 86
4.2 Charging Energies 91
4.3 Zero-Current Energy Gap 94
4.4 Electron and Hole Addition Energies 95
4.5 Discussion 99

5. Conclusions 101

Appendices:

A. Electron and Hole Levels 105

Bibliography 107

LIST OF TABLES

Table **Page**

2.1 Tight-binding parameters for Si, CdSe, and InAs 21

2.2 Indirect band gap and effective masses of Si bands 22

2.3 Direct band gaps and effective masses of CdSe and InAs bands 22

2.4 Compositions of electron wave functions in terms of orbital types for Si and CdSe quantum dots 28

2.5 Compositions of electron wave functions in terms of orbital types for InAs quantum dots 28

3.1 Computation methods for Coulomb and exchange integrals 43

3.2 On-site unscreened Coulomb and exchange integrals 44

3.3 On-site screened Coulomb integrals 44

3.4 Nearest-neighbor screened Coulomb integrals 45

3.5 On-site unscreened Coulomb and exchange integrals with various basis orbitals 47

3.6 Nearest-neighbor unscreened Coulomb and exchange integrals with various basis orbitals 48

3.7 Local dipole moments between basis orbitals 63

3.8 Compositions of the first three bright-exciton levels, and the dominant angular momenta of the exciton envelope functions 76

4.1 Main contributions to addition energy spacings 97

LIST OF FIGURES

Figure **Page**

1.1 Band edges of quantum dots embedded in a larger-gap material . . . 6

1.2 Effect of dimensionalities on the density of states 7

1.3 Quantum-dot shapes and sizes with various fabrication methods . . . 7

1.4 Double-barrier tunneling junction configuration 10

2.1 Spin-orbit coupling effect on InAs bulk band structure 23

2.2 Effect of d orbitals on InAs bulk band structure 24

2.3 Single-particle energy gaps vs. dot radius 27

3.1 Dielectric function of Si quantum dots as a function of distance between two particles 37

3.2 Radial function of Slater-type orbitals 39

3.3 Sensitivity of Coulomb energies to the choice of basis orbitals 50

3.4 Exchange energy of Si quantum dots vs. cutoff distance 58

3.5 Exchange energy of CdSe quantum dots vs. cutoff distance 59

3.6 Exchange energy of InAs quantum dots vs. cutoff distance 60

3.7 Exchange charge density distributions 61

3.8 Exciton gap of Si quantum dots vs. dot radius 66

3.9 Coulomb shift vs. quantum dot radius 67

3.10 Exciton gap and single-particle gap of CdSe quantum dots vs. dot radius 69

3.11 Coulomb, exchange, and correlation energies for CdSe quantum dots vs. dot radius 70

3.12 Exciton absorption spectra of InAs quantum dots with various radii . 73

3.13 Exciton absorption spectra of InAs quantum dots calculated with various tight-binding models 74

3.14 Lowest bright-exciton energies of InAs quantum dots vs. dot radius . 75

3.15 Three lowest bright exciton energies of InAs quantum dots vs. dot radius 81

3.16 First three bright exciton level spacings of InAs quantum dots 82

4.1 Differential conductance spectra of quantum dots 85

4.2 Polarized charges at the surface between the dot and its surrounding 88

4.3 Coulomb interactions responsible for self-polarization energies and polarized Coulomb energies 89

4.4 Polarization of a charged quantum dot and the dot environment . . . 92

4.5 Zero-current energy gaps and charging energies for the gaps of InAs quantum dots vs. dot radius 96

4.6 Electron and hole addition energy spacings of InAs quantum dots vs. dot radius 98

CHAPTER 1

INTRODUCTION

What one fool can understand, others can. - Richard P. Feynman

Recent advances in semiconductor quantum dot fabrications have opened up a rich opportunity to study zero-dimensional quantum systems of various sizes, shapes, and materials [1, 2, 3, 4]. Quantum confinement and enhanced many-body interactions in the quantum dots lead to optical and transport properties that are dramatically different from those of higher dimensional and bigger systems [3, 4, 5, 6]. To utilize the unique properties, many applications such as low-threshold lasers, single-electron devices, memories, detectors, single photon emitters, and quantum information devices have been proposed, and are being developed [7, 8, 9, 10, 11, 12]. Hence, the accurate modeling of the quantum confinement and many-body interactions is not only of fundamental interest, but is also important to help tailor quantum dots for a specific application.

Various theoretical approaches are used to study the quantum dots, ranging from first principle calculations to empirical models [13, 14, 15, 16, 17, 18, 19, 20, 21, 22, 23]. Due to the generally high computational demand of the first principle calculations, empirical models are widely employed to study quantum dots with sizes comparable

to experimental dots. The three empirical models primarily used are the multiband effective-mass approximation [16], the pseudo-potential model [18, 19], and the tight-binding model [20, 21, 22, 23]. The effective-mass approximation treats quantum dots as a confined bulk system, while the pseudo-potential and tight-binding models include atomistic descriptions of ionic potentials in the dot. The distinction between the two atomistic models lies in the degree of atomic detail included in the model. Within the tight-binding model, the atomistic detail is limited to a small basis set, while in the pseudo-potential model a detailed local variation of wave functions is described with a large basis set. Therefore, the tight-binding model is computationally less costly than the pseudo-potential model. The tight-binding model is a good candidate for the study of relatively big, complicated systems where both the computational efficiency and atomistic description are required. An example of such a system is vertically stacked, self-assembled quantum dots which contain not only millions of atoms but also a thin barrier and sharp edges and points [24]. Because of the computational efficiency of this atomistic model, we choose the tight-binding model to study quantum dots.

Modeling chemically synthesized quantum dots is a good starting point to test the applicability of the tight-binding model to quantum dots. The chemically synthesized dots are unstrained and spherical due to the flexible surrounding materials [3]. The dot sizes are easily controlled by changing chemical-synthesis conditions [25]. The simple tuning of the dot size enables the study of size dependent properties without involving such complexities as strains and shapes. In this work, we examine the accuracy of the tight-binding model in describing the optical and transport properties of chemically synthesized quantum dots with a wide range of sizes.

Recently, two types of complementary experiments have provided a comprehensive picture of the many-body levels of quantum dots [26, 27, 28, 29]. First, photoluminescence excitation (PLE) experiments manifest exciton levels by optically creating electron-hole pairs [26, 27]. Second, scanning tunneling microscope (STM) experiments probe individual electron (or hole) levels by consecutively charging the dot with one electron (or one hole) at a time [28, 29]. Both the electron-hole pair creation and the electron (or hole) addition probe the single-particle levels of the dots. However, different perturbative interactions are inherent in each experiment. The electron-hole pair creation involves electron-hole interactions, while the electron (or hole) addition induces the extra-charge-carrier interactions and the polarization of the dot environment. Furthermore, the electron-hole pair creation is an optically selective process. In spherical dots, the optical selection rules are determined by almost exact conservation of angular momenta.

Motivated by the two types of experiments, we study the many-body levels of optically excited and multiply charged semiconductor quantum dots in the framework of the empirical tight-binding model. We choose Si, CdSe, and InAs dots as examples of an indirect-gap material, and typical II-VI and III-V direct-gap materials, respectively. To represent chemically synthesized dots, the dot structure is modeled as an unstrained and spherical crystallite with perfect surface passivation. We incorporate electron-hole interactions and dipole transitions into the tight-binding model to investigate the electron-hole pair levels of the optically excited dots. The electron and hole addition energies of the multiply charged dots are described by the sum of single-particle energies and charging energies. The present model includes three

types of charging energies: (i) self-polarization energies, (ii) charge-carrier Coulomb energies, and (iii) electron-removal work functions.

The remainder of the dissertation is structured as follows. In the remainder of this chapter, we provide a brief overview of quantum dots, the two types of experiments, and the three empirical models primarily used for quantum-dot studies. In Chapter 2, we discuss the present tight-binding model for the single-particle levels of Si, CdSe, and InAs dots. Chapter 3 describes the electron-hole pair levels of optically excited quantum dots. In Chapter 4, we model the electron and hole addition energies of multiply charged quantum dots. Finally, Chapter 5 provides a brief summary of the key results of the present work and a final remark on future work directions.

1.1 Quantum Dots

Quantum dots are nanometer-scale, three-dimensionally confined systems. With respect to system sizes, quantum dots are intermediate between molecular and bulk systems. Hence, the structure of the dot shows both molecular and bulk features. The interior of the quantum dot contains a crystal structure which resembles a bulk crystal. However, the periodicity of the crystal is violated near the dot surface before the dot size reaches an infinite volume limit. Quantum dots are surrounded by foreign materials whose conduction and valence band edges are different from those of the dots. If the conduction and valence band edges of the surrounding material are higher and lower than those of the dots as shown in Fig. 1.1, both electrons and holes can be confined in the dots.

The three-dimensional quantum confinement of electrons in semiconductor quantum dots leads to discrete electronic levels with their spacings typically exceeding

room temperature. Figure 1.2 shows the evolution of the density of states as the effective dimensionality of systems reduces. As more dimensions are confined, the density of states becomes less continuous, and eventually becomes delta-function like in the zero-dimensional quantum dots. Because of its discrete level structure, the quantum dot is often referred to as an artificial atom.

Because of the discrete level structures of quantum dots, the electrical and optical properties of the quantum dots are qualitatively different from those of higher-dimensional systems such as bulk, quantum-well, and quantum-wire systems. For example, electrons confined in quantum dots exhibit slow intersubband relaxation times due to a reduced electron-phonon interaction. Furthermore, optical excitations and electrical transport in quantum dots depend strongly on the dot sizes. As the size is reduced, the electronic excitation energies increase due to the increase of electron kinetic energies. For instance, the absorption onset of CdSe quantum dots vary from deep red (1.7 eV) to green (2.4 eV) when the size decreases from 200 to 20 Å [25]. Thanks to their unique and size tunable properties, quantum dots are proposed as building units of various nano-devices such as low-threshold lasers, novel single-electron devices, memories, detectors, single-photon emitters, and quantum information devices.

Quantum dots are fabricated typically by one of the three different methods: (i) a combined method of lithography and epitaxy, (ii) Stranski-Krastanow epitaxy, and (iii) a chemical synthesis. Figure 1.3 illustrates the general shapes and sizes of the quantum dots produced by the three methods. The combined method of lithography and epitaxy generates a vertical quantum dot whose vertical size is much smaller than its lateral sizes. Typically, the vertical size is on the order of 10 nm while the lateral

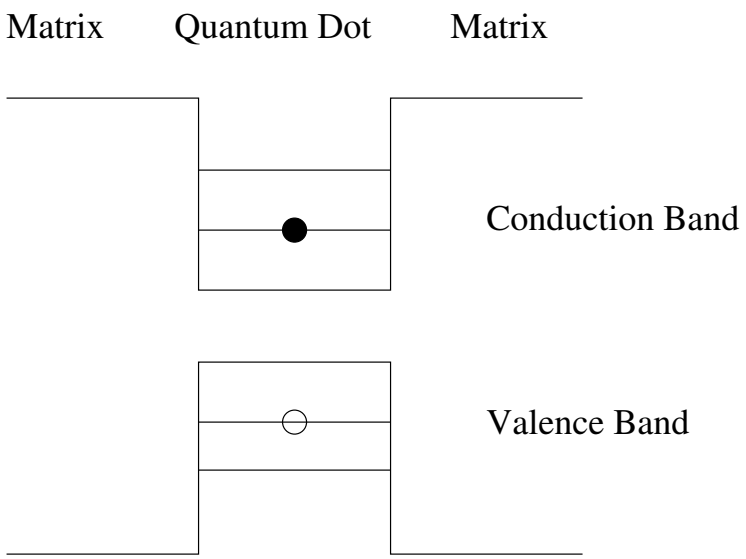

Figure 1.1: Schematic diagram of band edges of the quantum dot embedded in a larger-gap material. The higher conduction band edge of the surrounding matrix provides a barrier potential to confine electrons in the dot, while the lower valence band edge of the matrix confines holes.

size is on the order of 100 nm. The Stranski-Krastanow epitaxy uses the strain induced by a lattice mismatch between a dot and a surrounding material [30]. A typical example of this kind of dot is an InAs dot embedded in GaAs. Because the lattice constant of InAs is 7.2 % larger than GaAs, only a thin layer of InAs can grow on a GaAs substrate before the layer breaks up into small islands, forming self-assembled InAs quantum dots. The self-assembled dots are strained, and consequently pyramid or lens shaped. In the chemical synthesis, the dangling bonds at the dot surfaces is passivated with a variety of organic and inorganic ligands [25, 26, 31]. Due to the flexibility of the ligands, chemically synthesized dots are unstrained and spherical.

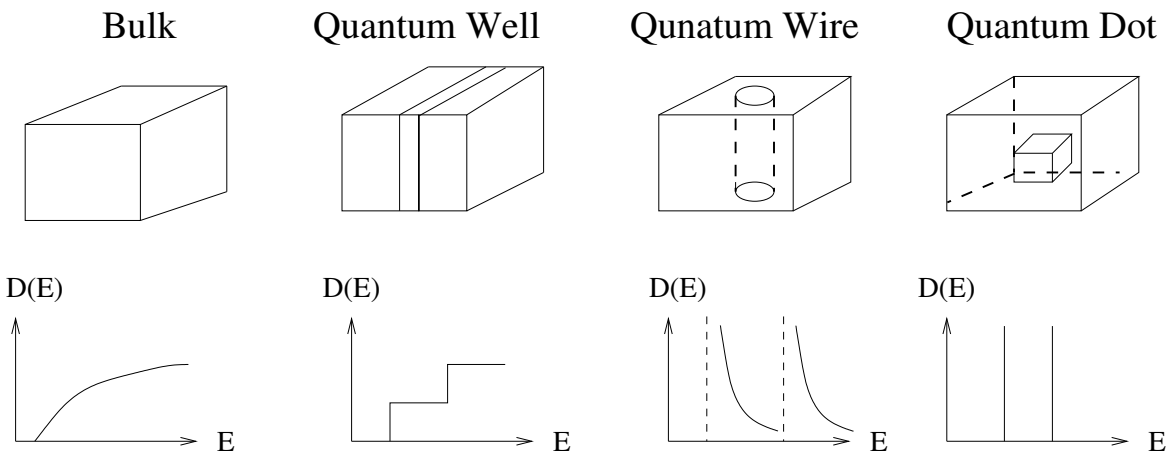

Figure 1.2: Density of states for various dimensional systems ranging from three-dimensional bulk systems to zero-dimensional quantum dots. As more dimensions are confined, the continuities of the density of states become weaker, and eventually disappear in the quantum dot.

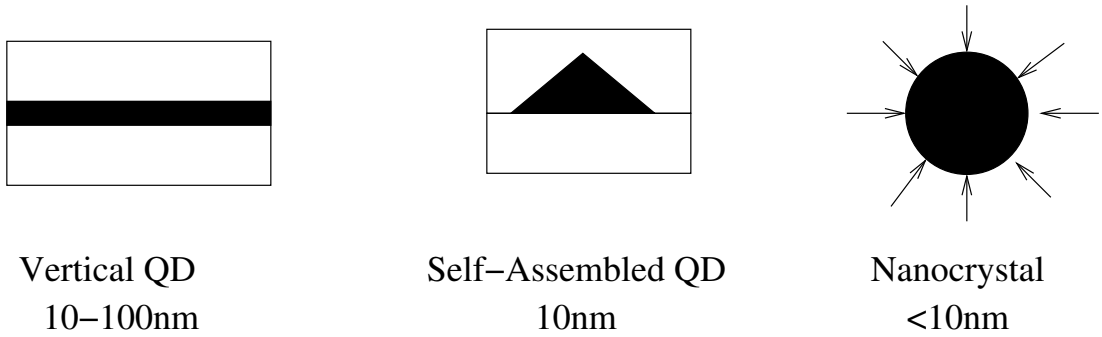

Figure 1.3: Typical shapes and sizes of quantum dots fabricated by three different methods. The vertical quantum dot is produced by the combination of lithography and epitaxy. The pyramid-shaped self-assembled dot is the product of the Stranski-Krastanow epitaxy. The spherical nanocrystal surrounded by a flexible glass matrix is fabricated by a chemical synthesis.

1.2 Experimental Approaches

In this section, we present the main ideas and examples of the two experimental approaches primarily used to study many-body level structures of quantum dots: optical excitation and electrical excitation. The two types of experiments provide the different aspects of the level structures, yielding a comprehensive picture of the structure.

1.2.1 Optical Excitation

The optical excitation of quantum dots is a process of creating electron-hole pairs in the quantum dots. The created electron-hole pair forms a bound state due to the attractive Coulomb interaction between the electron and hole. The bound state is called an exciton. To create excitons requires meeting two conditions. First, a photon energy of an optical excitation source should match the energy required to create an exciton due to the conservation of energies. Second, the total angular momentum of an exciton should be the same as that of an absorbed photon, i.e. one, due to the conservation of angular momenta. Therefore, the measurement of the response of quantum dots to the optical excitation such as absorption and emission measurements reveals the exciton level structures of the dots.

One widely used method for the measurement of the response of optically excited quantum dots is a photoluminescence excitation experiment [26, 27]. When an ensemble of quantum dots is excited by a laser, a wide size distribution of the quantum dots broadens absorption spectra so that resolving the exciton levels of individual quantum dots is difficult. The photoluminescence excitation is developed to eliminate the broadening due to the size distribution. In the photoluminescence excitation

experiment, the detection energies of photoluminescence are fixed and laser-excitation energies are varied. If the excitation energies match the energies required to create excitons, photons are absorbed and excitons are created. The created excitons eventually relax to exciton levels near the band edges, recombine, and emit photoluminescence. Therefore, detecting photoluminescence as a function of the laser-excitation energies is an indirect way of measuring absorption spectra. The main difference between the photoluminescence excitation and absorption measurements is that the photoluminescence excitation experiment filters dot sizes by narrowing the photoluminescence detection energies.

1.2.2 Electrical Excitation

The electrical excitation of quantum dots is a process of consecutively charging the quantum dots with one electron or one hole at a time. If the Fermi energy of the material surrounding the dot is resonant with the energy required to add one electron into the dot, an electron can be added to the dot, causing the dot to become negatively charged. Similarly, if the Fermi energy of the surrounding material is resonant with the negative of the energy required to remove one electron from the dot, an electron can be removed from the dot, causing the dot to become positively charged. Removing an electron can be seen as adding a hole. We call the energies required to add an electron and a hole *an electron and hole addition energy*, respectively. The electron and hole addition energies are composed of single-particle energies of quantum dots and charging energies for the charge-carrier transfer. Therefore, the measurement of the response of quantum dots to the electrical excitation manifests individual electron and hole level structures as well as charging energies.

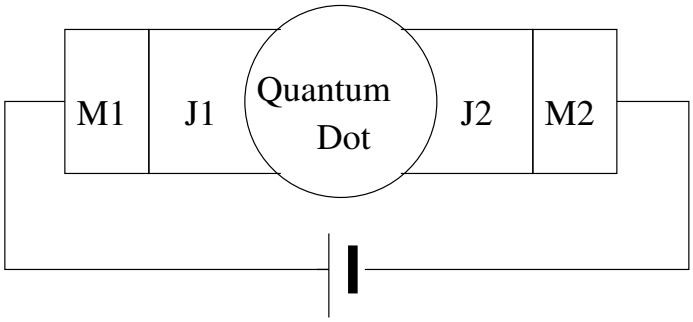

Figure 1.4: Schematic diagram of a double-barrier tunneling junction configuration composed of a quantum dot, two metal leads (M1 and M2), and two insulating junctions (J1 and J2).

One example of the measurement of the response of electrically excited quantum dots is that of tunneling current between a metal lead and a quantum dot which are separated by an insulating junction. In the experiment, the quantum dot is a part of a double-barrier tunneling junction configuration as illustrated in Fig. 1.4. Typically, the configuration is realized either by a transistor-type configuration [5, 6] or by a scanning tunneling microscope [28, 32]. Measured tunneling spectra exhibit a region of suppressed tunneling current followed by a series of steps due to the discrete levels of quantum dots and the Coulomb blockade for charge-carrier transfer. The beginning of the step in the tunneling spectra, i.e. the peak of the differential conductance of tunneling current, indicates that the tunneling condition to add electrons or holes into a dot is met. Hence, the electron and hole addition energies are equivalent to the bias voltages which cause conductance peaks.

1.3 Theoretical Approaches

In this section, we discuss the basic ideas and applications of three theoretical models primarily used to study quantum dots: (i) the effective-mass approximation, (ii) the pseudo-potential model, and (iii) the tight-binding model. Since quantum dots are intermediate between molecular and bulk systems, to treat the quantum dot as one of the two extreme systems is a natural starting point. The effective-mass approximation treats the dot as a confined bulk system, while the pseudo-potential model and the tight-binding model treat the dot as a collection of atoms.

1.3.1 Effective-Mass Approximation

The effective-mass approximation models a single-particle Hamiltonian with the dispersion relations of bulk bands near the minimum and maximum. The kinetic energy of the single-particle Hamiltonian is described by replacing a bare electron mass with an effective mass. The effective mass m^* is obtained from the band curvature near the minimum and maximum when the dispersion relation $E(k)$ of the band is given:

$$\frac{1}{m^*} = \frac{1}{\hbar^2} \left. \frac{\partial^2 E(k)}{\partial k^2} \right|_{k=0}. \tag{1.1}$$

In the simplest case where the coupling between the lowest conduction and the highest valence bands is negligible, the effective Hamiltonians of low-lying electron and hole levels in quantum dots can be separately written as

$$H_e = -\frac{\hbar^2 \nabla^2}{2m_e^*} + V_e(r) + E_g, \tag{1.2}$$

$$H_h = -\frac{\hbar^2 \nabla^2}{2m_h^*} + V_h(r), \tag{1.3}$$

where m_e^* and m_h^* are the electron and hole effective masses. E_g is a bulk band gap, i.e. the energy difference between the bottom of the lowest conduction band and the top of the highest valence band. The confinement of the quantum dot is imposed in the potential $V(r)$. In a spherical quantum dot, the confining potential can be written as

$$V(r) = V_o \, \Theta(r - R), \tag{1.4}$$

where $\Theta(r - R)$ is the step function and R is the dot radius. The constant V_o is determined by a band offset between the dot and the surrounding material.

The single-band effective-mass approximation can be improved by including more bands and by allowing couplings between different bands. For example, the Luttinger-Kohn Hamiltonian includes the contributions from the second and third highest valence bands to the hole Hamiltonian [33]. This new Hamiltonian also includes the couplings between the three valence bands, i.e. heavy-hole, light-hole, and spin-split hole bands. Luttinger-Kohn model can be further improved by including the couplings between the conduction and valence bands [34]. When the coupling is included, the single-particle Hamiltonian is no longer divided into the electron and hole Hamiltonians. The coupling between the conduction and valence bands is important especially in modeling narrow-gap semiconductor quantum dots [26].

The accuracy of the effective-mass approximation has inherent limitations due to nonparabolic bulk bands away from Γ and the lack of atomistic descriptions of the Hamiltonian. Since the Hamiltonian is constructed based on the parabolic dispersion relations of bands near Γ, this approximation is valid only if relevant bands near Γ can be approximated as parabolic curves, and relevant properties are attributed to single-particle levels near Γ. Furthermore, since the effective-mass approximation does not

contain the atomistic description of ionic potentials in the Hamiltonian, it cannot provide an accurate description of quantum systems with complex surfaces and thin barriers. The low-lying electron and holes states of quantum dots appear near Γ as the dot size increases. Therefore, the effective-mass approximation is applicable to relatively large quantum dots with interior properties outweighing surface properties.

1.3.2 Pseudo-Potential Model

The pseudo-potential model approximates a real potential due to ions and core electrons with a pseudo-potential given by the condition that both potentials provide a similar description of electron wave functions outside the core region. Within the pseudo-potential model, the nodal features of the wave functions in the core region are ignored. This approximation is reasonable when relevant properties are determined by the variation of the wave function outside the core region. The typical basis orbitals of the pseudo-potential model are plane waves. The pseudo-potential Hamiltonian H and wave function $\psi(\mathbf{r})$ are written as

$$H = -\frac{\hbar^2\nabla^2}{2m} + \sum_i V_{\rm ps}(\mathbf{r} - \mathbf{R_i}) \tag{1.5}$$

$$\psi(\mathbf{r}) = \sum_{\mathbf{k}} c_{\mathbf{k}} \exp(i\mathbf{k}\cdot\mathbf{r}), \tag{1.6}$$

where $\mathbf{R}_i$ is the position vector of ion-core sites, and $V_{\rm ps}$ is the pseudo-potential.

The basic idea of the pseudo-potential model can be applied to quantum-dot studies by representing the ionic potentials of the dot and the surrounding material with corresponding pseudo-potentials. In the pseudo-potential model, a barrier potential treated as a step function in the effective-mass approximation is atomistically described by the difference between the pseudo-potentials of the dot and the surrounding materials. Since a single-particle Hamiltonian is composed of atomistic

pseudo-potentials in this model, a single-particle wave function contains a detailed description of the variation between core sites. Due to the atomistic detail included in the pseudo-potential model, the calculations of single-particle energies and wave functions with this model are computationally much more demanding than the effective-mass approximation. Therefore, the application of this model has been limited to the studies of relatively small dots with radius smaller than 25 Å [18, 35]. However, the progress in computer facilities and numerical algorithms will steadily extend the application of this model to bigger quantum dots.

1.3.3 Tight-Binding Model

The tight-binding model approximates electron wave functions in solids by linear combinations of atomic orbitals of valence electrons in atoms. This approximation is based on the assumption that electrons in solids are tightly bound to their ions as in atoms. This approach is opposite to the free electron model which assumes that electrons move freely in solids so that their wave functions can be described by plane waves. Conceptually, the assumption of the tightly bound electrons limits a scope of the applicability of the tight-binding model within insulating materials and the valence bands of semiconductors. However, it has been shown that the tight-binding model can also successfully describe the electronic properties of transition metals and the conduction bands of semiconductors by relaxing the range of interactions between valence electrons, by empirically adjusting the interaction matrix elements, and by expanding a basis set.

Similar to the pseudo-potential model, the tight-binding model provides an atomistic description of the single-particle Hamiltonian and wave function of quantum

dots. In the tight-binding model, the single-particle Hamiltonian consists of the interactions between valence electrons in presence of ionic potentials. The basis orbitals of the tight-binding model are atomic orbitals of the valence electrons in quantum dots which are not necessarily the same as the atomic orbitals of the valence electrons in atoms. The Hamiltonian matrix elements between the basis orbitals can be determined by either an *ab initio* or empirical method. In the *ab initio* approach, the matrix elements are calculated with the real atomic orbitals and ionic potentials. In contrast, the empirical tight-binding model treats the matrix elements as fitting parameters. As an intermediate approach, there is a semi-empirical tight-binding model where the Hamiltonian matrix elements are determined by the combinations of atomistic calculations and empirical fittings.

The tight-binding model is computationally less demanding than the pseudo-potential model due to its smaller number of basis orbitals. Typically, the number of basis orbitals in the tight-binding model is one or two orders of magnitude smaller than that in the pseudo-potential model. Due to its computational efficiency, the tight-binding model can be used to study a wide range of dot sizes. This advantage is one key reason that we choose the tight-binding model to study the electrical and optical properties of quantum dots. The construction of the single-particle Hamiltonian of quantum dots and the calculation of single-particle energies and wave functions within the tight-binding model are discussed in detail in Chap. 2.

CHAPTER 2

SINGLE-PARTICLE LEVELS OF QUANTUM DOTS

If you have an important point to make, don't try to be subtle or clever. Use a pile driver. Hit the point once. Then come back and hit it again. Then hit it a third time - a tremendous whack. -Winston Churchill, Sir

Although ideally many-body levels of quantum dots should be obtained from many-body Hamiltonian, it is very difficult to directly solve the many-body Hamiltonian due to the large number of electrons involved in the Hamiltonian. Hence, we divide the Hamiltonian into two groups: a noninteracting single-particle term and an interaction term. The single-particle Hamiltonian can be viewed as the effective Hamiltonian of one electron in the presence of other electrons and ions. This chapter describes the construction of the effective single-particle Hamiltonian for Si, CdSe, and InAs quantum dots within the empirical tight-binding model and presents major features of electron energies and wave functions calculated with that Hamiltonian.

To imitate a chemically synthesized quantum dot which is almost unstrained and spherical with flexible-ligand passivation, we model the dot as an unstrained, spherical crystallite with perfect surface passivation. Experimental Si and InAs dots are based on the zinc-blende structure, while experimental CdSe dots on the wurtzite

structure. Therefore, we model Si and InAs dots as the zinc-blende crystallite. We also model CdSe dots as the zinc-blende structure since the small value of the crystal-splitting (25 meV) in CdSe makes it reasonable to approximate this wurtzite material as a zinc-blende material. Dangling bonds on the surface are removed by explicitly shifting the energies of the corresponding hybrids well above the band gap. This treatment imitates a chemically synthesized dot whose surface is efficiently passivated by hydrogen or ligand molecules.

2.1 Single-Particle Hamiltonian

Within the tight-binding model, the effective single-particle Hamiltonian of a quantum dot results from projecting the full Hamiltonian onto a limited basis set of atomic orbitals and imposing a cutoff on the range of the matrix elements between the orbitals:

$$H_{\text{single}} = \sum_{i,\gamma,\sigma,\sigma'} u_{i\gamma\sigma\sigma'} |i\gamma\sigma\rangle\langle i\gamma\sigma'| + \sum_{i\neq j,\gamma,\gamma',\sigma,\sigma'} t_{ij\gamma\gamma'\sigma\sigma'} |i\gamma\sigma\rangle\langle j\gamma'\sigma'|, \tag{2.1}$$

The tight-binding basis orbital $|i\gamma\sigma\rangle$ is indexed by atomic-site index i, orbital-type index γ, and spin index σ. The symbols $u_{i\gamma\sigma\sigma'}$ and $t_{ij\gamma\gamma'\sigma}$ are the matrix elements between the tight-binding basis orbitals, and are usually referred to as tight-binding parameters. The parameter $u_{i\gamma\sigma\sigma'}$ accounts for the interaction between the basis orbitals on the same ions, while $t_{ij\gamma\gamma'\sigma}$ is that between the basis orbitals on different ions.

The simplest tight-binding model that can reproduce the major features of the lowest conduction and the highest valence bands [36] involves only onsite and nearest-neighbor matrix elements between sp^3s^* basis orbitals. Within the nearest-neighbor sp^3s^* model, the band energies at the high symmetry points are well described [36].

The s^* orbital, first introduced by Vogl *et al.* [36] to mimic band-structure effects of d bands, improves the conduction bands near X [36].

We choose tight-binding parameters optimized to mimic at the 10 meV level those bands – lowest conduction and highest valence – most responsible for the low energy excitation spectra of quantum dots. In the empirical tight-binding model, the parameters $u_{i\gamma\sigma\sigma'}$ and $t_{ij\gamma\gamma'\sigma\sigma'}$ are fitted to a relevant data base given by first-principle calculations and experiments. Since a data base for quantum dots is very limited today, a bulk data base such as the bulk band structures predicted by first-principle calculations and measured by experiments [37] is generally used for target values of the fitting. Especially, the band gap, the band curvatures near the minima or maxima of the lowest conduction and the highest valence bands are important target values since low-lying electron levels of quantum dots originate from the band edges. We choose the parameters that can reproduce the gap at the 10 meV level and the effective masses as well as possible. Table 2.1 lists the parameters used for Si, CdSe, and InAs dots. Tables 2.2 and 2.3 list the band gaps and effective masses given by the parameters.

Especially for Si dots, we use two sets of parameters optimized differently: (i) one set optimized to give good band energies at the high symmetry points but not optimized to give good effective masses, (ii) the other set optimized to give good effective masses as well as good band energies, to examine to what extent the good effective masses improve the electron levels of quantum dots. We first use the tight-binding parameters of Vogl *et al.* [36]. Their parameters are fitted to only the energies of the Γ and X points, and consequently give poor effective masses. To improve the effective mass of Si, we also use parameters optimized with a genetic algorithm to

give better effective masses near the minimum of the lowest conduction band [38, 39]. Using a genetic algorithm, Klimeck *et al.* provided parameter sets optimized separately for the conduction and valence bands [38]. Note that good effective masses for both conduction and valence band are impossible to obtain simultaneously with one parameter set within the nearest-neighbor sp^3s^* tight-binding model [38]. As a result, the conduction- and valence-electron wave functions, being generated from different Hamiltonians, are not orthogonal. Even though the orthogonality has not been enforced, the overlaps between the single-particle wave functions from the two Hamiltonians are at most 0.001. Thus, we can use these two different parameter sets to verify how important a role the effective masses play in the level structures of quantum dots. Table 2.2 lists the resulting effective masses of the lowest conduction and the highest valence bands with the parameters of Vogl *et al.* and those with the two parameter sets of Klimeck *et al.* The effective masses given by the parameters of Klimeck *et al.* agree much better with experimental values than those of Vogl *et al.* Especially, the electron transverse effective mass is improved the most by the parameters of Klimeck *et al.*

For InAs dots, (i) to improve valence electron levels we include spin-orbit coupling within the same sp^3s^* basis set and (ii) to improve conduction electron levels we extend the basis set to $sp^3d^5s^*$. The InAs bulk band structure is challenging to describe. It has a narrow band gap (0.42 eV) and a large spin-orbit splitting energy (0.38 eV), yielding a complicated valence band structure: a highly anisotropic heavy-hole band, a highly nonparabolic light-hole band, and a spin-split band. The inclusion of spin-orbit coupling improves the description of the valence bands. The inclusion of d orbitals improves the dispersion relations and symmetry characters of the Bloch

functions of the lowest conduction band near X and L points [40]. The inclusion of d orbitals also upgrades the s^* orbital, originally introduced to imitate d orbitals in the sp^3s^* model, to a excited s orbital that is more physical. Hence, the better description of the bulk bands with spin-orbit coupling and d orbitals included should improve the electron levels of InAs dots. Tight-binding parameters used for the sp^3s^* model including spin-orbit coupling and the $sp^3d^5s^*$ model including spin-orbit coupling are listed in Table 2.1.

Figures 2.1 and 2.2 present the effects of the inclusion of spin-orbit coupling and d orbitals on the bulk InAs band structure by comparing the bands calculated with the three tight-binding models used for InAs dots: the sp^3s^* models (i) excluding and (ii) including spin-orbit coupling, and (iii) the $sp^3d^5s^*$ model including spin-orbit coupling. Figure 2.1 compares the band structures between the sp^3s^* models including and excluding spin-orbit coupling. When the spin-orbit coupling is excluded, the highest valence bands are six-fold at the Γ point. The bands are composed of four-fold heavy-hole bands and two-fold light-hole bands. In contrast, the inclusion of the spin-orbit coupling splits the highest valence bands to three types of bands: (i) two-fold heavy-hole, (ii) two-fold light-hole, and (iii) two-fold spin-split bands, as shown in Fig. 2.1. Figure 2.2 compares the band structures between the sp^3s^* and the $sp^3d^5s^*$ models. Both models include spin-orbit coupling. Near the Γ point, the band curvatures and energies of the two models are almost identical. However, as k points move away from Γ, the $sp^3d^5s^*$ bands deviate from the sp^3s^* bands. The deviation yields larger conduction and smaller valence band curvatures in the $sp^3d^5s^*$ model.

Parameter	Si^A	Si^B	Si^C	CdSe	$InAs^A$	$InAs^B$	$InAs^C$
E_s^a	-4.200	-3.060	-4.777	-9.630	-7.983	-9.656	-5.980
E_s^c	-4.200	-3.060	-4.777	0.030	-1.808	-2.113	0.333
E_p^a	1.715	1.675	1.674	1.470	0.532	-0.016	3.581
E_p^c	1.715	1.675	1.674	4.730	3.827	4.569	6.494
E_d^a, E_d^c	0.000	0.000	0.000	0.000	0.000	0.000	12.195
$E_{s^*}^a$	6.685	4.756	8.697	7.530	12.583	9.138	17.841
$E_{s^*}^c$	6.685	4.756	8.697	5.720	7.921	4.772	17.841
$V_{ss\sigma}$	-2.075	-2.029	-2.116	-1.160	-1.067	1.252	-1.479
$V_{s^*s^*\sigma}$	0.000	0.000	0.000	0.000	0.000	0.000	-3.851
$V_{s_a s_c^* \sigma}$	0.000	0.000	0.000	0.000	0.000	0.000	-2.132
$V_{s_a^* s_c \sigma}$	0.000	0.000	0.000	0.000	0.000	0.000	-1.222
$V_{s_a p_c \sigma}$	2.481	3.566	2.479	1.979	1.909	1.156	2.316
$V_{s_c p_a \sigma}$	2.481	3.566	2.479	2.399	2.306	2.829	2.801
$V_{s_a^* p_c \sigma}$	2.327	2.595	2.656	1.321	2.531	1.889	2.647
$V_{s_c^* p_a \sigma}$	2.327	2.595	2.656	1.078	1.989	1.662	1.901
$V_{s_a d_c \sigma}$	0.000	0.000	0.000	0.000	0.000	0.000	-2.583
$V_{s_c d_a \sigma}$	0.000	0.000	0.000	0.000	0.000	0.000	-2.450
$V_{s_a^* d_c \sigma}$	0.000	0.000	0.000	0.000	0.000	0.000	-0.850
$V_{s_c^* d_a \sigma}$	0.000	0.000	0.000	0.000	0.000	0.000	-0.837
$V_{pp\sigma}$	2.716	11.338	2.878	3.340	3.035	2.570	4.119
$V_{pp\pi}$	-0.715	-5.041	-0.811	-0.680	-0.982	-0.977	-1.369
$V_{p_a d_c \sigma}$	0.000	0.000	0.000	0.000	0.000	0.000	-2.122
$V_{p_c d_a \sigma}$	0.000	0.000	0.000	0.000	0.000	0.000	-2.058
$V_{p_a d_c \pi}$	0.000	0.000	0.000	0.000	0.000	0.000	1.546
$V_{p_c d_a \pi}$	0.000	0.000	0.000	0.000	0.000	0.000	1.711
$V_{dd\sigma}$	0.000	0.000	0.000	0.000	0.000	0.000	-1.201
$V_{dd\pi}$	0.000	0.000	0.000	0.000	0.000	0.000	2.182
$V_{dd\delta}$	0.000	0.000	0.000	0.000	0.000	0.000	-1.779
Δ_a	0.000	0.000	0.000	0.000	0.000	0.376	0.529
Δ_c	0.000	0.000	0.000	0.000	0.000	0.510	0.374

Table 2.1: Tight-binding parameters for Si, CdSe, and InAs in units of eV. E_γ denotes the on-site parameter of orbital γ, and $V_{\gamma,\gamma'\beta}$ denotes the nearest-neighbor off-site parameter between two orbitals γ and γ' with bonding orientation β [41]. Δ_i refers to the spin-orbit splitting energy of atom i. The indexes a and c refer to anion and cation, respectively. Si^A is a parameter set taken from Ref. [36]. Si^B and Si^C are parameter sets optimized for conduction and valence levels, respectively[38]. $CdSe^A$ is a parameter set taken from Ref. [42]. $InAs^A$ and $InAs^B$ are parameter sets for the sp^3s^* model excluding and including spin-orbit coupling, while $InAs^C$ is that for the $sp^3d^5s^*$ model including spin-orbit coupling.

	E_{gap}	m_{cl}	m_{ct}	m_{lh}	m_{hh}
Vogl *et al.*	1.17	0.73	1.61	0.18	0.39
Klimeck *et al.*	1.17	0.91	0.30	0.15	0.55
Experiment	1.17	0.92	0.19	0.15	0.54

Table 2.2: Indirect band gap E_{gap} and effective masses of Si bands with the tight-binding parameters of Vogl *et al.* [36] and those of Klimeck *et al* [38]. The units of the gap and effective masses are eV and the free electron mass, respectively. m_{cl} and m_{ct} denote the longitudinal and transverse effective masses of the lowest conduction band near the X point. m_{lh} and m_{hh} are the effective masses at Γ of the light- and heavy-hole bands, respectively. The hole masses are averages of the three directions given in Ref. [38]. The experimental data are taken from Ref. [37].

	E_{gap}	m_c	m_v			
CdSe^A	1.90	0.13	0.41			
Data Base	1.90	0.11	0.44			
	E_{gap}	m_c	$m_{hh}[001]$	$m_{hh}[011]$	$m_{hh}[111]$	m_{lh}
InAs^A	0.37	0.025	0.27	0.27	0.57	0.022
InAs^B	0.42	0.025	0.35	0.64	0.86	0.028
InAs^C	0.42	0.024	0.32	0.65	0.95	0.029
Data Base	0.37/0.42	0.024	0.34	0.64	0.88	0.026

Table 2.3: Direct band gap E_{gap} and effective masses of CdSe and InAs bands given by the tight-binding parameters listed in Table 2.1. The units of the gaps and effective masses are eV and the free electron mass, respectively. The corresponding quantities either measured by experiments or predicted by other theoretical models are taken from Ref. [37] for comparison. Note that the parameter set InAs^A is fitted to the band gap (0.37 eV) at the room temperature, while the sets InAs^B and InAs^C are to the gap (0.42 eV) at 4.2 K. m_c and m_v denote the averaged effective masses of the lowest conduction band and the highest valence band (including both heavy- and light-hole bands) near Γ, respectively. $m_{hh}[lmn]$ is an heavy-hole effective mass in k direction $[lmn]$ near Γ, while m_{lh} is an averaged light-hole effective mass.

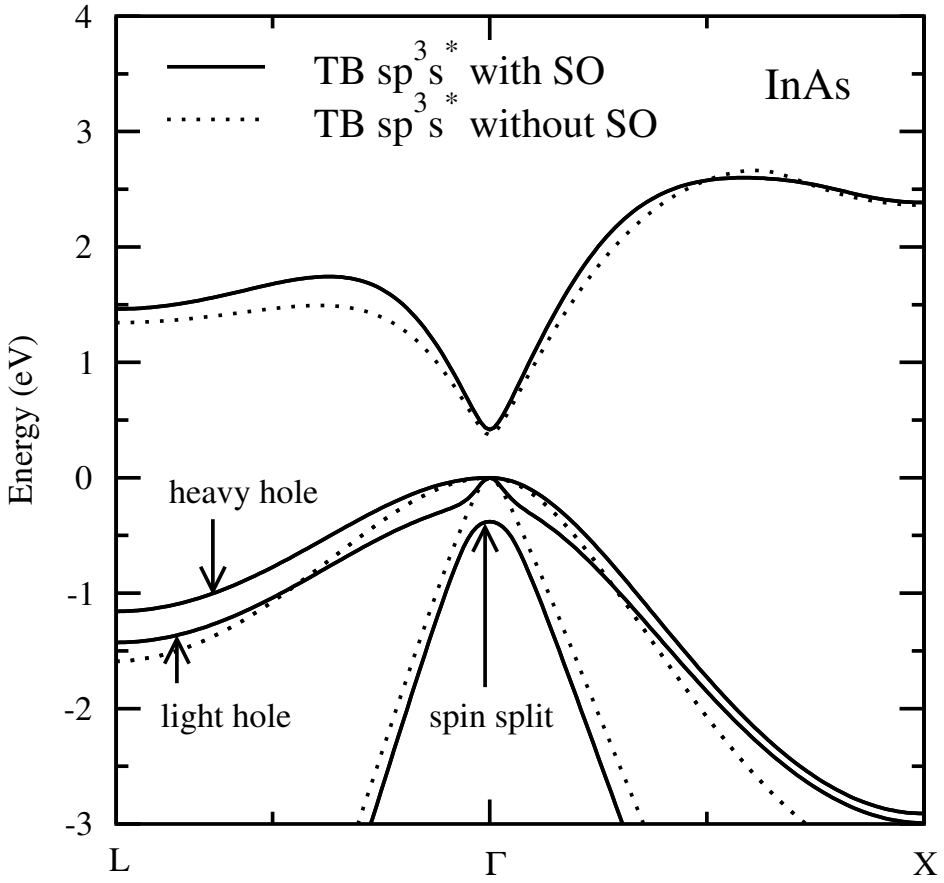

Figure 2.1: InAs bulk band structures calculated with the sp^3s^* tight-binding (TB) model including and excluding spin-orbit coupling. The solid lines depict the bulk band structure of the sp^3s^* model including spin-orbit coupling, while the dotted lines correspond to that of the sp^3s^* model excluding spin-orbit coupling. The parameters used for the two models are listed in Table 2.1. The inclusion of the spin-orbit coupling splits the highest valence bands to the heavy-hole, light-hole, and spin-split bands.

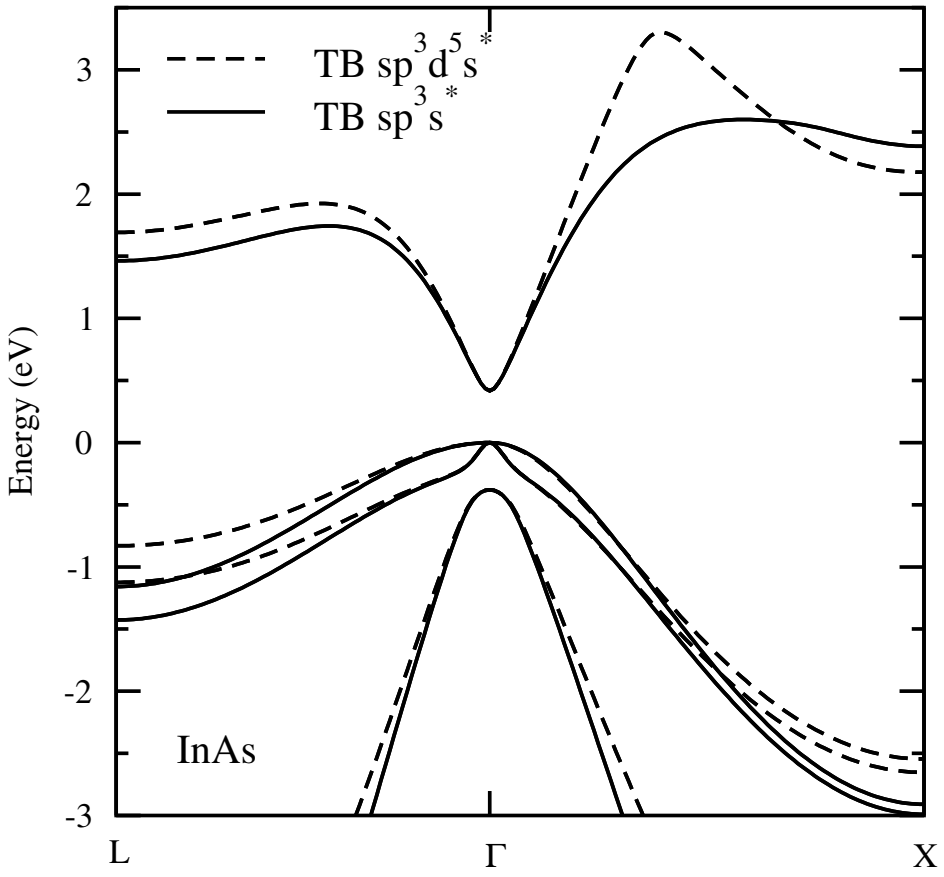

Figure 2.2: InAs bulk band structures calculated with the sp^3s^* and $sp^3d^5s^*$ tight-binding (TB) model. Both models include spin-orbit coupling. The solid lines depict the bulk band structure of the $sp^3d^5s^*$ model with parameters taken from Ref. [40], while the dashed lines correspond to that of the sp^3s^* model with parameters optimized by a genetic algorithm [38]. Near the Γ point, the band curvatures and energies of the two models are almost identical. However, the deviation of the $sp^3d^5s^*$ bands from the sp^3s^* bands becomes bigger, away from the Γ point. The deviation yields larger conduction and smaller valence band curvatures in the $sp^3d^5s^*$ model.

2.2 Single-Particle Energies and Wave Functions

In contrast to the particle-in-box expectation that the level spacing is inversely proportional to the square of the box size R, single-particle energy gaps of Si, CdSe, and InAs dots scale as $R^{-1.83}$, $R^{-1.23}$, and $R^{-1.15}$ in the fitting with the function $aR^{-n} + E_{\text{gap}}^{\text{bulk}}$, respectively. $E_{\text{gap}}^{\text{bulk}}$ denotes the bulk band gap of each material. Figure 2.3 shows the size dependences of the single-particle energy gaps. Pseudo-potential calculations show that the gaps scale as $R^{-1.20}$, $R^{-1.64}$, and $R^{-1.01}$ for Si [43], CdSe [44], and InAs [18] dots, respectively. Although the scaling behaviors of the gaps given by the tight-binding and the pseudo-potential models are different, both models suggest that the scaling exponent n is smaller than 2. As the size increases, the single-particle gaps ultimately approach the bulk band gaps, which are 1.2 eV, 1.8 eV, and 0.4 eV for Si, CdSe, and InAs, respectively.

Within the sp^3s^* model, the valence wave functions are mainly p-like in terms of dominant basis orbital types, while the conduction wave functions are s-like for direct-gap semiconductors and a mixture of s- and p-like for indirect-gap semiconductors. Tables 2.4 and 2.5 list the orbital-type distributions of the electron wave functions of Si, CdSe, and InAs dots. For all three dot materials, p orbitals constitute $> 95\%$ of the valence wave functions which are similar to a bonding p-like bulk valence band. For indirect-gap Si dots, p and s^* orbitals constitute about 80% of the conduction wave function reminiscent of the sp hybrid bulk conduction band near the X point. In contrast, the conduction wave functions of InAs and CdSe dots are mainly composed of s orbitals. This is consistent with the anti-bonding s-like bulk conduction band of InAs and CdSe.

As the single-particle Hamiltonian for InAs dots changes from the sp^3s^* to $sp^3d^5s^*$ model, the large fractions of s and p orbitals in electron wave functions shift to s^* and d, yielding a better description of the wave function symmetries [40]. Table 2.5 compares the composition of several electron wave functions in terms of orbital types between the sp^3s^* and $sp^3d^5s^*$ models. In several low-lying conduction wave functions, the large fraction of the s orbital shifts to s^* and d, while in valence wave functions, the large fraction of p shifts to d. The orbital fraction shifts are attributed to the introduction of the couplings between s and s^*, between s and d, and between p and d. In contrast to these large shifts, only small changes are observed in the p orbital fraction of the conduction wave functions, and s- and s^*-orbital fractions of the valence wave functions. The compositions of the electron wave functions are similar to those of bulk Bloch wave functions near the band edges [40]. The Bloch function compositions obtained by the $sp^3d^5s^*$ tight-binding model show good agreement with self-consistent pseudo-potential calculations [40, 45].

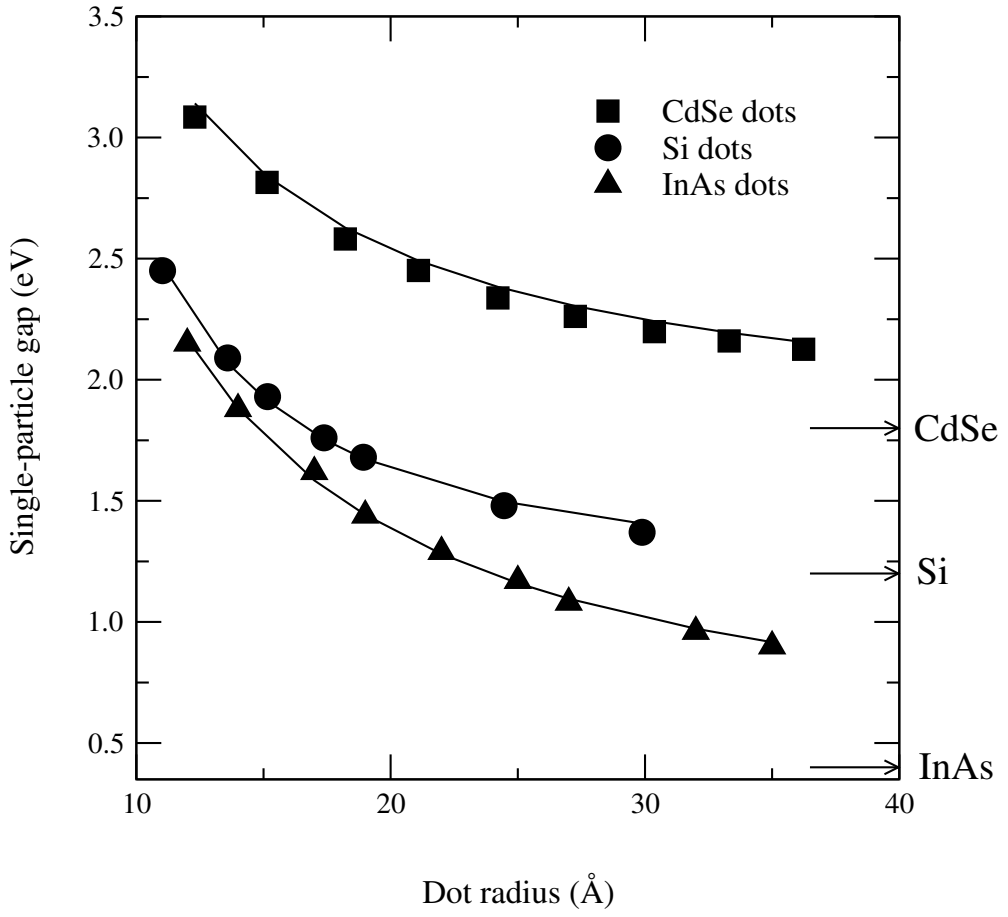

Figure 2.3: Single-particle energy gaps of Si, CdSe, and InAs quantum dots versus the dot radius. The Si, CdSe, and InAs gaps are calculated with tight-binding parameter sets of Si^B, CdSe^A, and InAs^C listed in Table 2.1, respectively. The solid lines are $(aR^{-n} + E_{\rm gap}^{\rm bulk})$ fits with n=1.83, 1.23, and 1.15 for Si, CdSe, and InAs gaps, respectively. $E_{\rm gap}^{\rm bulk}$ is the bulk band gap. The correlation coefficients of the fits are > 0.99. The arrows indicate the bulk band gaps of Si, CdSe, and InAs.

Si				CdSe			
Level	s	p	s^*	Level	s	p	s^*
c_1	0.177	0.452	0.371	c_1	0.850	0.139	0.011
c_2	0.185	0.444	0.371	c_2	0.739	0.233	0.029
v_1	0.027	0.962	0.011	v_1	0.047	0.950	0.003
v_2	0.002	0.996	0.002	v_2	0.007	0.993	0.001

Table 2.4: Compositions of electron wave functions in terms of orbital types for Si and CdSe quantum dots with radius 14 Å. The calculated fraction of the wave function in orbital type γ is the sum of the tight-binding coefficient squares $|c_{i\gamma\sigma}|^2$ over all atomic sites i and spins σ. The levels c_n and v_n are the nth lowest conduction and the nth highest valence levels, respectively.

InAs	sp^3s^* model			$sp^3d^5s^*$ model			
Level	s	p	s^*	s	p	d	s^*
c_1	0.802	0.172	0.026	0.563	0.177	0.023	0.238
c_2	0.445	0.380	0.175	0.438	0.309	0.040	0.212
c_6	0.624	0.313	0.063	0.342	0.464	0.105	0.089
v_1	0.004	0.994	0.002	0.005	0.821	0.173	0.001
v_2	0.041	0.953	0.006	0.034	0.785	0.174	0.007

Table 2.5: Compositions of electron wave functions in terms of orbital types for an InAs quantum dot with radius 14 Å. The calculated fraction of the wave function in orbital type γ is the sum of the tight-binding coefficient squares $|c_{i\gamma\sigma}|^2$ over all atomic sites i and spins σ. The levels c_n and v_n are the nth lowest conduction and the nth highest valence electron levels, respectively. The compositions of the electron wave functions between the $sp^3d^5s^*$ and the sp^3s^* tight-binding models are compared.

CHAPTER 3

OPTICALLY EXCITED QUANTUM DOTS

In science one tries to tell people, in such a way as to be understood by everyone, something that no one ever knew before. But in poetry, it's the exact opposite.

-Paul Dirac

In this chapter, we investigate the exciton levels of optically excited quantum dots by incorporating electron-hole interactions and electron-hole dipole transitions into the tight-binding model, and address four important questions regarding the modeling of the exciton levels.

First, how sensitive are calculated exciton energies to specific choices of atomic basis orbitals? Since tight-binding matrix elements for a single-particle Hamiltonian are empirically optimized without introducing any specific atomic orbitals, there is no direct way to calculate other matrix elements such as Coulomb, exchange, and dipole-moment matrix elements. Therefore, calculations involving the electron-hole interactions and dipole moments require a selection of specific atomic orbitals that cannot be explicitly related to the tight-binding parameters. Hence, we need to test to what degree specific choices of orbitals affects exciton energies. We choose two reasonable sets of atomic orbitals to represent the tight-binding basis orbitals:

(i) Slater-type orbitals and (ii) Gaussian-type orbitals. We compare electron-hole interaction matrix elements modeled with the two types of orbitals. We also develop a scaling scheme to quantify the effects of the choices of atomic orbitals on electron-hole Coulomb energies.

Second, what is the range of the electron-hole exchange interaction in quantum dots? A recent pseudo-potential study showed that electron-hole exchange interactions can extend over a whole dot due to the lack of local orthogonality between electron and hole wave functions [46]. We investigate in detail the effective range of the exchange interaction by applying a cutoff range to the Coulomb potential, following the approach of Franceschetti and co-workers [46]. The origin of the characteristic range of the exchange interaction is revealed by the analysis of the exchange charge density of the electron-hole pair.

Third, how large is the correlation effect of the electron-hole configuration interactions on low-lying exciton energies? The coupling between electron-hole configurations yields exciton states composed of many different electron-hole configurations. To examine the correlation effect of the couplings on exciton energies, we apply both configuration interaction scheme and perturbation theory. By comparing exciton energies calculated with the two schemes, we can obtain correlation energies contributing to the exciton energies.

Finally, how well does the tight-binding model describe the size-dependence of exciton energies? Tight-binding parameters used for a single-particle Hamiltonian of quantum dots are fitted to bulk band structures. Therefore, there is no direct connection between the parameters and quantum-dot properties. The only adjustment

applied to the single-particle Hamiltonian of quantum dots is the energy shift of dangling bonds at the dot surface. Hence, it is important to examine how transferable bulk tight-binding parameters are to describe the single-particle Hamiltonian of a quantum dot. The good description of electron-hole interactions and dipole moments is also required to accurately predict exciton energies. We compare several low-lying bright exciton energies with PLE experimental data to verify the tight-binding model for exciton energies of quantum dots.

3.1 Electron-Hole Hamiltonian

To describe an effective electron-hole Hamiltonian of a quantum dot, we choose a product of an electron and hole wave functions as a basis set $|eh\rangle$ of the effective Hamiltonian. The electron and hole wave functions are related to the single-particle wave functions calculated from the single-particle Hamiltonian described in Chap. 2 (see Appendix A).

The projection of the electron-hole basis set $|eh\rangle$ into a spatial $\mathbf{r}$ and spin σ space according to Eqs. A.4 and A.5 is

$$\langle \mathbf{r}_e, \sigma_e; \mathbf{r}_h, \sigma_h | eh \rangle \equiv \psi_e(\mathbf{r}_e, \sigma_e)\psi_h(\mathbf{r}_h, \sigma_h) \tag{3.1}$$

$$= \sum_{i\gamma\sigma_e} c_{e;i\gamma\sigma_e}\phi_{i\gamma}(\mathbf{r}_e)\chi_{\sigma_e} \sum_{i'\gamma'\sigma_h} c_{h;i'\gamma'\sigma_h}\phi^*_{i'\gamma'}(\mathbf{r}_h)\chi^*_{-\sigma_h}, \tag{3.2}$$

where $\psi_e(\mathbf{r}_e, \sigma_e)$ and $\psi_h(\mathbf{r}_h, \sigma_h)$ are an electron and hole wave functions, respectively. Within the electron and hole wave functions, the coefficients c_{e} and c_{h} describe global variations of the wave functions from one atomic site to another atomic site, while the tight-binding basis orbital $\phi_{i\gamma}(\mathbf{r})$ describes a local variation of the wave function near atomic site i with orbital-type γ. The global variation described by the coefficients is called an *envelope function*. The function χ_σ represents a spin state. In a special case

where a single-particle Hamiltonian excludes spin-orbit coupling, the spatial part of the electron-hole pair wave functions can be separated from its spin part:

$$\psi_e(\mathbf{r}_e, \sigma_e)\psi_h(\mathbf{r}_h, \sigma_h) = \psi_e(\mathbf{r}_e)\psi_h(\mathbf{r}_h)\chi_{\sigma_e}\chi_{\sigma_h}. \tag{3.3}$$

An effective electron-hole Hamiltonian consists of a non-interaction part and an interaction part.

$$H_{\mathrm{e-h}} = H_{non-int} + H_{int} \tag{3.4}$$

The non-interaction part of the electron-hole Hamiltonian can be written in terms of the electron-hole basis set and its eigenvalues as follows.

$$H_{non-int} = \sum_{eh}(E_e + E_h)|eh\rangle\langle eh|, \tag{3.5}$$

where E_e and E_h are the electron and hole energies, which are defined in Eqs. A.1 and A.2, respectively.

Projecting an electron-hole Coulomb J and exchange K interactions onto the basis set $|eh\rangle$ yields the interaction part of the electron-hole Hamiltonian:

$$H_{int} = J + K, \tag{3.6}$$

$$J = -e^2 \sum_{e'h'eh} |e'h'\rangle\langle eh| \sum_{\sigma,\sigma'} \int\int \mathrm{d}^3r'\mathrm{d}^3r \frac{\psi^*_{e'}(\mathbf{r}', \sigma)\psi_e(\mathbf{r}', \sigma)\psi^*_{h'}(\mathbf{r}, \sigma')\psi_h(\mathbf{r}, \sigma')}{\epsilon(|\mathbf{r}' - \mathbf{r}|, R)\ |\mathbf{r}' - \mathbf{r}|}, \tag{3.7}$$

$$K = e^2 \sum_{e'h'eh} |e'h'\rangle\langle eh| \sum_{\sigma,\sigma'} \int\int \mathrm{d}^3r'\mathrm{d}^3r \frac{\psi^*_{e'}(\mathbf{r}', \sigma)\psi^*_{h'}(\mathbf{r}', -\sigma)\psi_e(\mathbf{r}, \sigma')\psi_h(\mathbf{r}, -\sigma')}{\epsilon(|\mathbf{r}' - \mathbf{r}|, R)\ |\mathbf{r}' - \mathbf{r}|}, \tag{3.8}$$

where e is the elementary charge. The Coulomb interaction J describes the scattering of the electron from e to e' and the hole from h to h', whereas the exchange interaction K describes the recombination of a pair e, h at $\mathbf{r}$ and the recreation of a pair e', h'

at $\mathbf{r}'$. Both the Coulomb and exchange interactions are screened with a dielectric function, which is a function of quantum dot radius R and separation $|\mathbf{r}-\mathbf{r}'|$ between two particles. The model for the dielectric function is described in Chap. 3.2

Different spin selection rules are applied to the Coulomb and exchange interactions. In the Coulomb interaction, electron and hole spins are conserved. In contrast, the spins of an electron and a hole, which interact via the exchange interaction, should be opposite. Specifically, the spin selection rules are

$$\sigma_e = \sigma_{e'} \text{ and } \sigma_h = \sigma_{h'}, \qquad \text{for } \langle e'h'|J|eh\rangle, \tag{3.9}$$

$$\sigma_e = -\sigma_h \text{ and } \sigma_{e'} = -\sigma_{h'}, \qquad \text{for } \langle e'h'|K|eh\rangle. \tag{3.10}$$

The matrix elements of the electron-hole interaction Hamiltonian can be rewritten in terms of integrals over the tight-binding basis orbitals by replacing the electron and hole wave functions with Eqs. A.4 and A.5:

$$\begin{aligned}
\langle e'h'|J|eh\rangle &= -e^2 \sum_{n_1,n_2,n_3,n_4,\sigma,\sigma'} c^*_{e';n_1,\sigma} c_{e;n_2,\sigma} c^*_{h';n_3,\sigma'} c_{h;n_4,\sigma'} \\
&\quad \times \int\int \mathrm{d}^3r'\mathrm{d}^3r \frac{\phi^*_{n_1}(\mathbf{r}')\phi_{n_2}(\mathbf{r}')\phi^*_{n_3}(\mathbf{r})\phi_{n_4}(\mathbf{r})}{\epsilon(|\mathbf{r}'-\mathbf{r}|,R)\ |\mathbf{r}'-\mathbf{r}|}, \qquad (3.11)\\
\langle e'h'|K|eh\rangle &= e^2 \sum_{n_1,n_2,n_3,n_4,\sigma,\sigma'} c^*_{e';n_1,\sigma} c^*_{h';n_2,-\sigma} c_{e;n_3,\sigma'} c_{h;n_4,-\sigma'} \\
&\quad \times \int\int \mathrm{d}^3r'\mathrm{d}^3r \frac{\phi^*_{n_1}(\mathbf{r}')\phi_{n_2}(\mathbf{r}')\phi^*_{n_3}(\mathbf{r})\phi_{n_4}(\mathbf{r})}{\epsilon(|\mathbf{r}'-\mathbf{r}|,R)\ |\mathbf{r}'-\mathbf{r}|}. \qquad (3.12)
\end{aligned}$$

Among the four involving basis orbitals in the integrals, two orbitals come from the electron wave functions and the other two come from the hole wave functions. We define the common integral appearing in both Coulomb and exchange integrals as $\omega(n_1, n_2; n_3, n_4)$:

$$\omega(n_1,n_2;n_3,n_4) \equiv \int\int \mathrm{d}^3r'\mathrm{d}^3r \frac{\phi^*_{n_1}(\mathbf{r}')\phi_{n_2}(\mathbf{r}')\phi^*_{n_3}(\mathbf{r})\phi_{n_4}(\mathbf{r})}{\epsilon(|\mathbf{r}'-\mathbf{r}|,R)\ |\mathbf{r}'-\mathbf{r}|}. \tag{3.13}$$

We approximate the Coulomb and exchange interaction matrix elements by considering only integrals involving at most two distinct basis orbitals. This approximation is reasonable since the integrals involving more than two different orbitals are typically small compared to the kept integrals [20, 47]. After applying this approximation, we have two types of integrals,

$$\omega_{\text{coul}}(n, n') \equiv \omega(n, n; n', n') \tag{3.14}$$

$$\omega_{\text{exch}}(n, n') \equiv \omega(n, n'; n, n') = \omega(n, n'; n'n) \tag{3.15}$$

We define the first type of integrals as a Coulomb integral, where a basis orbital scatter to the same basis orbital through the Coulomb interaction. In the second type of integrals defined as an exchange integral, a basis orbital scatter to a different basis orbital. In terms of a charge density, the Coulomb integrals form a charge density at $\mathbf{r}$ and $\mathbf{r}'$ with the same basis orbitals, whereas two different basis orbitals form charge densities in the exchange integrals. The last equality in Eq. (3.15) is true when the basis orbitals are real as they are in this work.

To make our notations clear, note that the Coulomb and exchange *integrals* (w_{coul} and w_{exch}) are the interactions between the tight-binding basis orbitals, while the Coulomb and exchange *interactions* (J and K) are interactions between the electron and hole wave functions. In fact, the Coulomb interaction has contributions from both Coulomb and exchange integrals as does the exchange interaction.

Finally, we write the Coulomb and exchange interaction matrix elements in terms of the Coulomb and exchange integrals:

$$\begin{aligned}\langle e'h'|J|eh\rangle &= -e^2 \sum_{n,n',\sigma,\sigma'} c^*_{e';n,\sigma} c_{e;n,\sigma} c^*_{h';n',\sigma'} c_{h;n',\sigma'} \omega_{\text{coul}}(n, n') \\ &\quad -e^2 \sum_{n,n',\sigma,\sigma'} c^*_{e';n,\sigma} c_{e;n',\sigma} c^*_{h';n,\sigma'} c_{h;n',\sigma'} \omega_{\text{exch}}(n, n')\end{aligned}$$

$$
\begin{aligned}
& -e^2 \sum_{n,n',\sigma,\sigma'} c^*_{e';n,\sigma} c_{e;n',\sigma} c^*_{h';n',\sigma'} c_{h;n,\sigma'} \omega_{\text{exch}}(n,n'), && (3.16) \\
\langle e'h'|K|eh\rangle \;=\; & e^2 \sum_{n,n',\sigma,\sigma'} c^*_{e';n,\sigma} c^*_{h';n,\sigma} c_{e;n',\sigma'} c_{h;n',\sigma'} \omega_{\text{coul}}(n,n') \\
& +e^2 \sum_{n,n',\sigma,\sigma'} c^*_{e';n,\sigma} c^*_{h';n',\sigma} c_{e;n,\sigma'} c_{h;n',\sigma'} \omega_{\text{exch}}(n,n') \\
& +e^2 \sum_{n,n',\sigma,\sigma'} c^*_{e';n,\sigma} c^*_{h';n',\sigma} c_{e;n',\sigma'} c_{h;n,\sigma'} \omega_{\text{exch}}(n,n'). && (3.17)
\end{aligned}
$$

3.2 Dielectric Function

We use a distance- and size-dependent dielectric function to screen the Coulomb and exchange interactions of electron-hole pairs. The distance dependence of the dielectric function is approximated by the Thomas-Fermi model generalized for semiconductors [48], while the size dependence is given by the Penn model generalized for quantum dots [49, 50]. These models are semi-classical approximations of the dielectric function from the bulk limit. The distance dependence describes the screening of short-range interactions, whereas the size dependence determines the screening of long-range interactions.

The distance dependence of the dielectric function is obtained by imposing a cutoff distance r_0 on the Thomas-Fermi screening and by fixing a long-distance limit of the dielectric function with a static dielectric constant ϵ_0 within the Thomas-Fermi model [48]:

$$
\epsilon(r) = \begin{cases} \epsilon_0 \; qr_0/[\sinh q(r_0 - r) + qr], & : \quad r \le r_0 \\ \epsilon_0, & : \quad r \ge r_0. \end{cases} \tag{3.18}
$$

The cutoff distance r_0 is determined by

$$
\sinh qr_0/qr_0 = \epsilon_0, \tag{3.19}
$$

where the Thomas-Fermi wave vector q is $2\sqrt[3]{3n_0}\sqrt[6]{\pi}$, and n_0 is the density of electrons in uniform potentials.

The size dependence of the dielectric function is modeled by the Penn model generalized for quantum dots [49, 50] where continuous energy levels of the bulk are replaced with discrete energy levels of quantum dots. Within the model, the size-dependent dielectric function for quantum dots at a low-frequency limit and a long-distance limit is given by [50]:

$$\epsilon_0^{\rm dot}(R) \;=\; 1 + (\epsilon_0^{\rm bulk} - 1)\frac{(E_{\rm gap}^{\rm bulk} + \Delta)^2}{[E_{\rm gap}^{\rm dot}(R) + \Delta]^2}, \tag{3.20}$$

where $\epsilon_0^{\rm bulk}$ is a low-frequency limit of bulk dielectric constants. The shift Δ denotes $E_2 - E_{\rm gap}^{\rm bulk}$, where E_2 is the energy of the first pronounced peak in a bulk absorption spectrum. The energies $E_{\rm gap}^{\rm bulk}$ and $E_{\rm gap}^{\rm dot}(R)$ are the single-particle gaps for bulk and a dot with radius R, respectively.

By replacing the long-distance limit of the dielectric function in Eq. (3.18) with the size-dependent dielectric function given by Eq. (3.20), we combine these two models and obtain a distance- and size-dependent dielectric function for quantum dots:

$$\epsilon(r,R) = \begin{cases} \epsilon_0^{\rm dot}(R)\ qr_0/[\sinh q(r_0 - r) + qr], & : \quad r \le r_0 \\ \epsilon_0^{\rm dot}(R), & : \quad r \ge r_0. \end{cases} \tag{3.21}$$

The cutoff distance r_0 for the Thomas-Fermi screening is typically ~ 2 Å. The dielectric function $\epsilon_0^{\rm dot}(r)$ for Si quantum dots with dot radius 10 Å is shown in Fig. (3.1).

3.3 Coulomb Interactions

To calculate the Coulomb interactions, we need a real-space description of the tight-binding basis orbitals. However, the empirical tight-binding model has an inherent difficulty determining the tight-binding basis orbitals in real space. The real-space description of the basis orbitals is not provided since the tight-binding matrix elements are determined by fitting to the bulk band structure without introducing

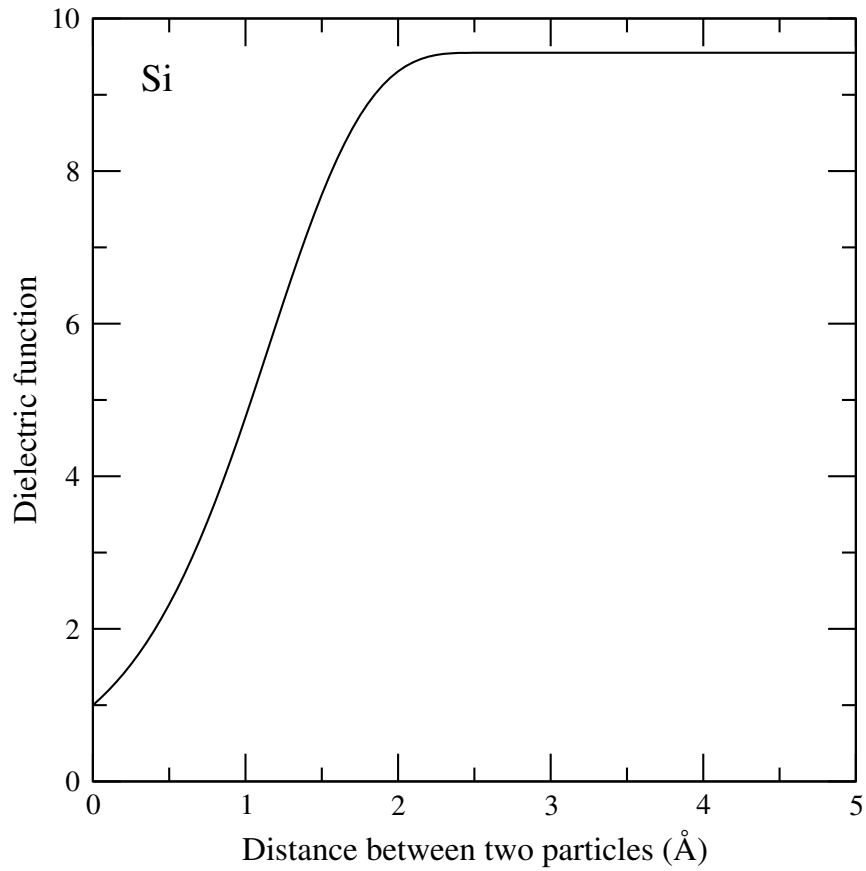

Figure 3.1: Dielectric function as a function of the distance r between two particles for Si quantum dots with radius 10 Å. The dielectric function is given by Eq. 3.21.

explicit basis orbitals. Since there is no easy way to extract basis orbitals from the empirically chosen tight-binding parameters, the choice of basis orbitals is largely arbitrary. Therefore, we test to what degree the choice of orbitals affects the electron-hole Coulomb interactions.

3.3.1 Coulomb and Exchange Integrals

To calculate the Coulomb and exchange interactions, we first evaluate their basic components, the Coulomb and exchange integrals, by modeling the tight-binding orbitals with atomic Slater orbitals [51], following Martin *et al* [47]. The Slater orbitals are single-exponential functions with the exponent given by the Slater rules [51] designed to yield a good approximation of effective ion radii and the ionization energies. In Slater orbitals, the radial part of the wave function is written as

$$R(r) = r^a \exp(-br), \tag{3.22}$$

where the constant a and b are determined by the Slater rules [51]. The Slater rules are specially designed for occupied orbitals such as s and p orbitals of valence electrons in semiconductors. Therefore, the Slater rules should be modified for excited states d and s^* orbitals. As an extent of the Slater rules, we model a d orbital by promoting one valence electron in the s or p orbitals to a d orbital in the same shell. Similarly, an s orbital is obtained by exciting one valence electron to an s orbital in the next shell. Figure (3.2) shows the radial parts of the s, p, d and s^* Slater-type orbitals for Si. The s and p Slater orbitals are well localized, whereas the excited d and s^* are loosely localized to overlap with orbitals centered on several neighbors.

The excited d^5 and s^* orbitals are treated as the same orbital in the Coulomb and exchange integrals to reduce the computational time. This approximation is

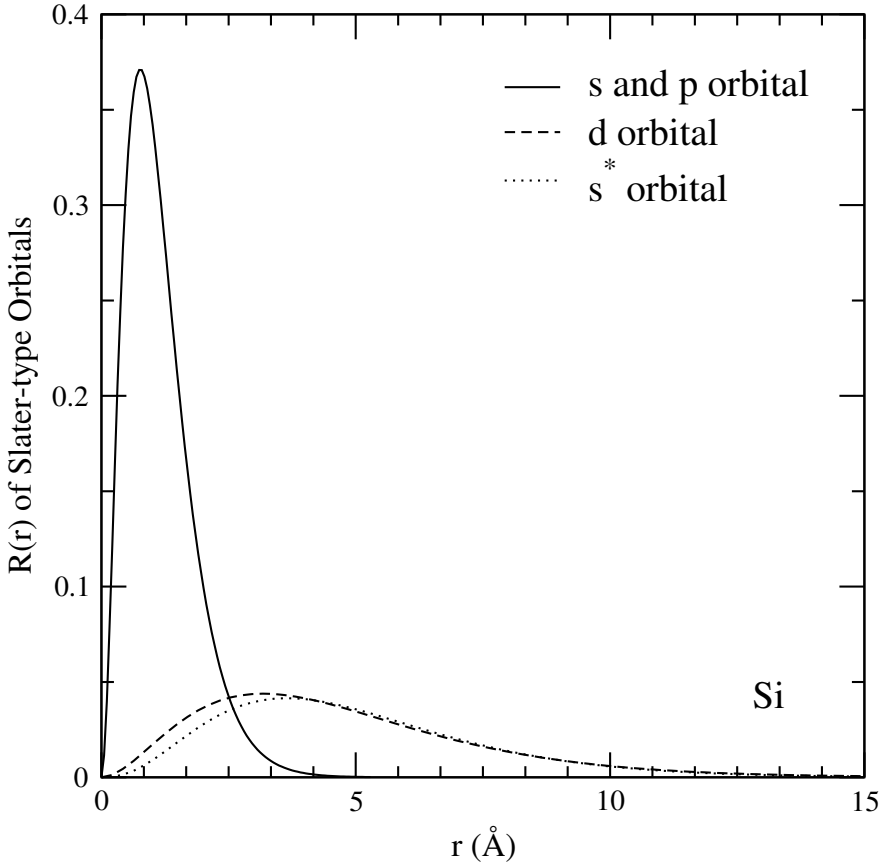

Figure 3.2: Radial parts of s, p, d and s^* Slater-type orbitals for Si. The effective radius of the s and p orbitals is 1 Å. In contrast to the well localized s and p orbitals, the excited d and s^* orbitals are widely spread across a couple of lattice constants.

reasonable for the two following reasons. First, the radial distribution of the d^5 and s^* orbitals is similar as shown in Fig. 3.2. Second, the difference of the angular distribution between the d^5 and s^* orbitals can be suppressed by averaging out the angular distributions of the d^5 orbitals with the sum of those of the five d orbitals:

$$|\phi_{d^5}|^2 \equiv \sum_{i=1}^{5} |\phi_{d_i}|^2. \tag{3.23}$$

On-site Coulomb and exchange integrals, in which both orbitals are centered on the same atom, are calculated using a Monte Carlo method with importance sampling for the radial integrations. The uncertainty of the Monte Carlo results is within 1%. The angular part is integrated exactly by expansion in spherical harmonics. However, the section 3.3.2 shows that the integral values must be considered to be uncertain to about 20-30% due to the arbitrariness of the orbital choice and the effects of orthogonalization.

Off-site exchange integrals, where the two orbitals are centered on two different atom sites, are negligible even for nearest-neighbor integrals. These integrals decrease quickly as the distance between atom sites increases, due to the localization and orthogonality of the orbitals. In particular, we show in the section 3.3.2 that even nearest-neighbor exchange integrals are negligible due to the effect of orthogonalization between off-site hybrids. Therefore, in this work we neglect off-site exchange integrals beyond the nearest-neighbor integrals for the calculations of the Coulomb and exchange matrix elements.

Regarding off-site Coulomb integrals, we first estimate these integrals with the Ohno formula [52] modified to include screening,

$$\omega_{\mathrm{Coul}}(n, n') \equiv \omega_{\mathrm{Coul}}(i\gamma, i'\gamma')$$

$$= \frac{1}{\epsilon(|\mathbf{R}_i - \mathbf{R}_{i'}|, R)} \frac{1}{\sqrt{\omega^0_{\mathrm{Coul}}(i\gamma, i\gamma')^{-2} + |\mathbf{R}_i - \mathbf{R}_{i'}|^2}}. \tag{3.24}$$

The tight-binding orbital index n is replaced with atom-site index i and orbital-type index γ for clarity. The vectors $\mathbf{R}_i$ and $\mathbf{R}_{i'}$ are atom site vectors. The symbol $\omega^0_{\mathrm{Coul}}(i\gamma, i\gamma')$ is an unscreened on-site Coulomb integral, where the superscript 0 designates an unscreened quantity. For the case of binary compounds, $\omega^0_{\mathrm{Coul}}(i\gamma, i\gamma')$ is replaced by the average over the two different atoms. The integrals are effectively screened by the dielectric constant $\epsilon(|\mathbf{R}_i - \mathbf{R}_{i'}|, R)$. This approximation is based on the assumption that the effective separation between two particles in an integral can be represented by the distance between atomic sites in which two orbitals of the integral are centered. Adding the screening effect is the only modification to the original Ohno formula.

The modified Ohno formula is reasonable for the integrals whose two orbitals are centered on distant atom sites, because the details of the charge distributions of the distant orbitals are not important. In the large-distance limit, the two orbitals become effectively point charges. However, as the two orbitals of the integrals are from closer atom sites, the details of spatial distributions of the two orbitals and dielectric function become more important. To test the validity of the modified Ohno formula in the case that two orbitals are on close atom sites, we calculated the off-site Coulomb integrals with a Monte Carlo method within 1% uncertainty and compared these values with those from the modified Ohno formula.

The modified Ohno formula severely underestimates the off-site integrals as the distance between two atom sites becomes as small as the nearest-neighbor distance. For example, the Coulomb integral between the orbitals from nearest neighbors in a Si quantum dot with radius 19Å given by the Ohno formula is 0.58 eV, while the

Monte Carlo calculation gives 2.35 eV. For next-nearest neighbors, the Ohno formula and the Monte Carlo calculation give 0.38 and 0.58 eV, respectively, and for the third-nearest neighbors 0.33 and 0.36 eV. The difference between the results from the Ohno formula and the Monte Carlo calculation becomes smaller as the distance between the two atom sites becomes larger.

A big discrepancy between the Ohno formula and the Monte Carlo calculations for the nearest-neighbor integrals results from the fact that the spatial overlap of the nearest-neighbor orbitals is as big as that of the orbitals on the same atom site. In addition, the spatial dependence of the dielectric function is not fully taken into account in the modified Ohno formula. This approximation becomes critical when the range of variations in the dielectric function is comparable to the effective distance between orbitals. In that case, the effective dielectric function cannot be represented by $\epsilon(|\mathbf{R}_i - \mathbf{R}_{i'}|, R)$. In light of the limit of the modified Ohno formula, we use the Monte Carlo values for the on-site and the nearest-neighbor integrals and the Ohno formula for the rest of off-site integrals. For clarity, we summarize the methods we used for computation of the Coulomb and exchange integrals in Table 3.1.

As new basis orbitals for the Coulomb and exchange integrals, we prepare four hybridized sp^3 orbitals along the bonding directions in a zinc-blende structure as the basis orbitals of the integrals. The four hybridized sp^3 orbitals for anion atoms are

$$\begin{aligned}
|sp^3_a\rangle &\equiv \frac{1}{2}(|s\rangle + |p_x\rangle + |p_y\rangle + |p_z\rangle), \\
|sp^3_b\rangle &\equiv \frac{1}{2}(|s\rangle + |p_x\rangle - |p_y\rangle - |p_z\rangle), \\
|sp^3_c\rangle &\equiv \frac{1}{2}(|s\rangle - |p_x\rangle + |p_y\rangle - |p_z\rangle), \\
|sp^3_d\rangle &\equiv \frac{1}{2}(|s\rangle - |p_x\rangle - |p_y\rangle + |p_z\rangle).
\end{aligned} \tag{3.25}$$

	on-site	NN	beyond NN
Coulomb	Monte Carlo	Monte Carlo	Ohno formula
exchange	Monte Carlo	neglected	neglected

Table 3.1: Methods for the computations of the Coulomb and exchange integrals with respect to a site-to-site distance. NN stands for nearest-neighbors.

For cation atoms, the four hybridized orbitals are

$$\begin{aligned}
|sp_a^3\rangle &\equiv \frac{1}{2}(|s\rangle - |p_x\rangle - |p_y\rangle - |p_z\rangle), \\
|sp_b^3\rangle &\equiv \frac{1}{2}(|s\rangle - |p_x\rangle + |p_y\rangle + |p_z\rangle), \\
|sp_c^3\rangle &\equiv \frac{1}{2}(|s\rangle + |p_x\rangle - |p_y\rangle + |p_z\rangle), \\
|sp_d^3\rangle &\equiv \frac{1}{2}(|s\rangle + |p_x\rangle + |p_y\rangle - |p_z\rangle).
\end{aligned} \tag{3.26}$$

Calculated Coulomb and exchange integrals based on the hybridized sp^3 orbitals and s^* orbital are listed in Tables 3.2, 3.3, and 3.4. The calculated unscreened integrals are used in the modified Ohno formula to calculate off-site screened Coulomb integrals. The comparison between the unscreened and screened on-site Coulomb integrals shows that the screening effect is significant even for on-site integrals. This is because the cutoff radius of Thomas-Fermi screening r_0 is ~ 2 Å and it is comparable to the spatial extension of the basis orbitals. With a simple analysis, we find that the effective screening of on-site Coulomb integrals is generally about half the long-range screening given by $\epsilon_0^{\rm dot}(R)$. Based on this observation, we use half of the long-range dielectric constant to screen the on-site exchange integrals.

Element	Integral type	(sp^3_a, sp^3_a)	(sp^3_a, sp^3_b)	(sp^3_a, s^*)	(s^*, s^*)
Si	Coulomb	11.88	8.49	2.87	2.27
Si	exchange	11.88	0.78	0.024	2.27
In	Coulomb	7.82	5.67	2.30	1.36
In	exchange	7.82	0.47	0.024	1.36
As	Coulomb	12.13	9.26	2.34	1.73
As	exchange	12.13	0.47	0.028	1.73
Cd	Coulomb	6.59	5.06	1.77	1.44
Cd	exchange	6.59	0.74	0.017	1.44
Se	Coulomb	12.85	9.70	2.97	2.38
Se	exchange	12.85	0.95	0.030	2.38

Table 3.2: On-site unscreened Coulomb and exchange integrals defined in Eqs. (3.14) and (3.15) for the sp^3s^* basis set, in units of eV. Integrals for the sp^3 orbitals are calculated based on the hybridized orbitals defined in Eqs. (3.25) and (3.26).

Element	(sp^3_a, sp^3_a)	(sp^3_a, sp^3_b)	(sp^3_a, s^*)	(s^*, s^*)
Si	3.16 (1.26)	1.67 (0.91)	0.32 (0.31)	0.26 (0.24)
In	1.26 (0.80)	0.77 (0.58)	0.24 (0.24)	0.17 (0.14)
As	2.33 (1.24)	1.33 (0.95)	0.28 (0.24)	0.23 (0.18)
Cd	1.86 (1.29)	1.20 (0.99)	0.35 (0.35)	0.28 (0.28)
Se	4.74 (2.51)	2.76 (1.89)	0.58 (0.58)	0.48 (0.46)

Table 3.3: On-site screened Coulomb integrals of the sp^3 hybridized orbitals and s^* orbital for the Si dot with radius R=19 Å, InAs with R=21 Å, and CdSe with R=21 Å, in unites of eV. The integrals are screened by the dielectric function in Eq. (3.21), which is a function of electron-hole separation and of quantum-dot radius. For comparison, the values in parentheses are the integrals obtained from full screening with the dielectric constant in the long-distance limit $\epsilon_0^{\rm dot}(R)$.

Si	Si bonding	Si non-bonding
Si bonding	2.35 (0.58)	0.95 (0.53)
Si non-bonding	0.95 (0.53)	0.55 (0.53)
InAs	In bonding	In non-bonding
As bonding	1.43 (0.54)	0.61 (0.54)
As non-bonding	0.81 (0.53)	0.42 (0.53)
CdSe	Cd bonding	Cd non-bonding
Se bonding	2.41 (1.03)	1.03 (1.02)
Se non-bonding	1.62 (1.02)	0.79 (1.00)

Table 3.4: Nearest-neighbor screened Coulomb integrals of the hybridized sp^3 orbitals for the Si dot with radius R=19 Å, InAs with R=21 Å, and CdSe with R=21 Å, in units of eV. The integrals are screened by the dielectric function in Eq. (3.21). The values given by the modified Ohno formula Eq. (3.24) are listed within parentheses.

3.3.2 Choice of Basis Orbitals

In principle, Coulomb and exchange integrals calculated with a particular set of basis orbitals change as we choose different basis orbitals. Therefore, the sensitivity of Coulomb and exchange integrals to the choice of basis orbitals need to be checked. An alternative set of basis orbitals is that given by the standard quantum chemistry Gaussian-based commercial packages [53]. Two important questions can be answered by a comparison between integrals obtained from Gaussian-type orbitals and Slater orbitals: what is the typical variation in the integral values for two reasonable choices of orbitals; and what is the effect of using nonorthogonal bond hybrids rather than properly orthogonalized hybrids? The underlying assumption in the tight-binding approach is that the orbitals on different sites are orthogonal.

Table 3.5 shows a comparison between orthogonal Gaussian-type orbitals, nonorthogonal Gaussian-type orbitals, and nonorthogonal Slater orbitals for on-site unscreened

Coulomb and exchange integrals [54]. Typically, the Coulomb integrals of the nonorthogonal Gaussian-type and the nonorthogonal Slater orbitals differ by 10%, whereas the exchange integrals (an order of magnitude smaller than Coulomb integrals) differ by 20-50%. Orthogonalization generally gives an additional 10% change. The use of nonorthogonal Slater orbitals can therefore be estimated to imply 20% overall uncertainty in the on-site integrals.

A similar comparison for nearest-neighbor integrals is shown in Table 3.6. Here the difference between the nonorthogonal Gaussian-type and the nonorthogonal Slater orbitals is less than 10%, but orthogonalization can yield a lowering of up to 30% in the Coulomb integrals between bonding orbitals. The most dramatic effect, however, is that the exchange integrals essentially become negligible when orthogonalized hybrids are used. Notably, nonorthogonal hybrids cannot be used for the bonding-bonding off-site exchange integrals, since these integrals are quite large without orthogonalization but are reduced by a factor of 20–30 after orthogonalization.

In conclusion, the dominant Coulomb integrals obtained from the Slater orbitals can be considered accurate only to 20-30% due to the sensitivity to different functional representations and to effect of orthogonalization. Further, proper orthogonalization reveals that all off-site exchange integrals can be neglected, including those between bonding hybrids.

3.3.3 Reliability of Coulomb Interaction Calculations

In the section 3.3.2, we find that the variation of on-site and nearest-neighbor Coulomb and exchange integrals with reasonable choices of basis orbitals are within

Integral type	O-GTO	NO-GTO	NO-SO
$\omega^0_{\text{Coul}}(a,a)$ of Si	11.95	11.65	11.91
$\omega^0_{\text{Coul}}(a,b)$ of Si	9.44	8.85	9.00
$\omega^0_{\text{exch}}(a,b)$ of Si	1.06	0.91	0.73
$\omega^0_{\text{Coul}}(a,a)$ of In	7.90	8.52	7.82
$\omega^0_{\text{Coul}}(a,b)$ of In	6.73	6.54	5.67
$\omega^0_{\text{exch}}(a,b)$ of In	0.77	0.67	0.47
$\omega^0_{\text{Coul}}(a,a)$ of As	12.99	12.57	12.13
$\omega^0_{\text{Coul}}(a,b)$ of As	10.00	9.54	9.26
$\omega^0_{\text{exch}}(a,b)$ of As	1.08	0.99	0.47
$\omega^0_{\text{Coul}}(a,a)$ of Cd	7.09	7.81	6.59
$\omega^0_{\text{Coul}}(a,b)$ of Cd	6.08	5.98	5.06
$\omega^0_{\text{exch}}(a,b)$ of Cd	0.70	0.61	0.74
$\omega^0_{\text{Coul}}(a,a)$ of Se	14.14	13.73	12.85
$\omega^0_{\text{Coul}}(a,b)$ of Se	10.80	10.39	9.70
$\omega^0_{\text{exch}}(a,b)$ of Se	1.15	1.08	0.90

Table 3.5: Onsite unscreened Coulomb and exchange integrals with: (O-GTO) Löwdin orthogonalized Gaussian-type hybrids; (NO-GTO) nonorthogonal Gaussian-type hybrids; and (NO-SO) nonorthogonal Slater orbitals. The GTO integrals were calculated with the MOLPRO [53] package using the atomic pseudo-potentials from the Los Alamos group [55]. The NO-SO integrals are from our Monte Carlo calculations. The hybrids a and b are the ones defined as sp^3_a and sp^3_b in Eqs. (3.25) and (3.26)

Si	O-GTO	NO-GTO	NO-SO
$\omega^0_{\text{Coul}}(B,B)$	8.04	10.01	10.60
$\omega^0_{\text{Coul}}(B,N)$	5.96	6.65	6.78
$\omega^0_{\text{Coul}}(N,N)$	4.64	4.67	4.89
$\omega^0_{\text{exch}}(B,B)$	0.27	6.20	
$\omega^0_{\text{exch}}(B,N)$	0.11	0.43	
$\omega^0_{\text{exch}}(N,N)$	0.04	0.32	
InAs	O-GTO	NO-GTO	NO-SO
$\omega^0_{\text{Coul}}(B,B)$	6.94	8.77	9.06
$\omega^0_{\text{Coul}}(B,N)$	5.50	6.39	6.59
$\omega^0_{\text{Coul}}(N,B)$	5.02	5.42	5.43
$\omega^0_{\text{Coul}}(N,N)$	4.12	4.18	4.24
$\omega^0_{\text{exch}}(B,B)$	0.28	4.90	
$\omega^0_{\text{exch}}(B,N)$	0.16	0.59	
$\omega^0_{\text{exch}}(N,B)$	0.04	0.18	
$\omega^0_{\text{exch}}(N,N)$	0.04	0.29	
CdSe	O-GTO	NO-GTO	NO-SO
$\omega^0_{\text{Coul}}(B,B)$	6.94	8.77	9.06
$\omega^0_{\text{Coul}}(B,B)$	6.89	8.66	8.74
$\omega^0_{\text{Coul}}(B,N)$	5.66	6.62	6.84
$\omega^0_{\text{Coul}}(N,B)$	4.85	5.16	5.01
$\omega^0_{\text{Coul}}(N,N)$	4.06	4.11	4.13
$\omega^0_{\text{exch}}(B,B)$	0.27	4.35	
$\omega^0_{\text{exch}}(B,N)$	0.19	0.69	
$\omega^0_{\text{exch}}(N,B)$	0.03	0.13	
$\omega^0_{\text{exch}}(N,N)$	0.04	0.24	

Table 3.6: Nearest-neighbor unscreened Coulomb and exchange integrals with: (O-GTO) Löwdin orthogonalized Gaussian-type hybrids; (NO-GTO) nonorthogonal Gaussian-type hybrids; and (NO-SO) nonorthogonal Slater orbitals. The GTO integrals were calculated with the MOLPRO [53] package using the pseudo-potentials from the Los Alamos group [55] for a two-atom molecule with a bond length given by the bulk value. The SO integrals are from our Monte Carlo calculations. The indices B and N designate the bonding and non-bonding sp^3 hybrids, respectively.

20-30%. The next question we ask is to what degree the electron-hole Coulomb interactions are sensitive to the values of on-site and nearest-neighbor integrals.

We perform this test by scaling the on-site and nearest-neighbor Coulomb and exchange integrals from the values listed in Tables 3.2, 3.3, and 3.4, and calculating the electron-hole Coulomb interactions as a function of the scaling factor. This scaling scheme is an indirect way of testing the sensitivity to the real-space description. Off-site integrals are scaled by replacing the unscreened on-site integrals with the scaled ones in the Ohno formula, Eq. (3.24). Note that the off-site Coulomb integrals are *not* directly scaled by the same factor as the on-site integrals, but change only indirectly through the scaled unscreened on-site integrals in the Ohno formula. Therefore, this scaling scheme in effect changes the atomistic details of the basis orbitals.

Figure 3.3 shows the variation of the Coulomb interaction between the lowest hole and electron states with respect to the scaling factor for the Coulomb and exchange integrals. It shows as a dot size increases, the sensitivity of the Coulomb interaction to the on-site integrals decreases. For example, if the on-site integrals are reduced by 50%, the reduction in the Coulomb energy varies from 20% in the smallest shown dot to only 5% at 30 Å-radius. Since the contribution from the on-site integrals decreases as the dot size increases, the specific model for the real-space functions for the basis orbitals is less critical for larger dots.

The insensitivity of the Coulomb energies to the scaling factor in large quantum dots is due to the long-range character of the Coulomb interaction. We can explain the insensitivity by a closer look at the Ohno formula for the off-site integrals. In the limit of a large distance between two atom sites, the off-site integral becomes

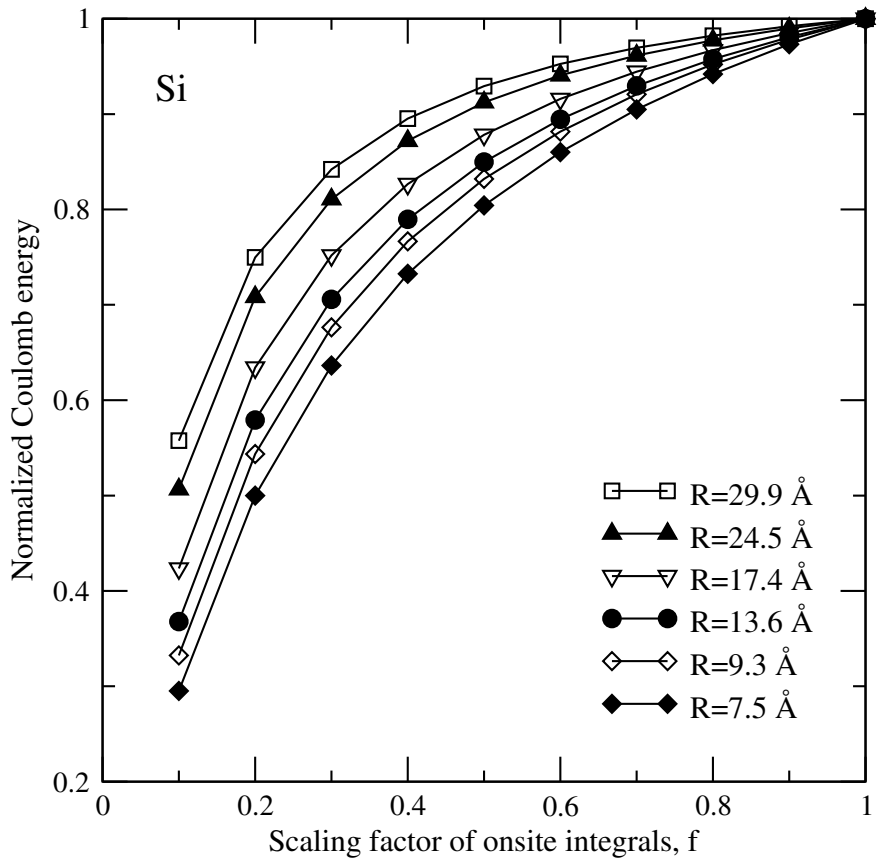

Figure 3.3: Coulomb energy $\langle eh|J(f)|eh\rangle$ as a function of scaling factor f of the on-site and nearest-neighbor integrals. The Coulomb energy with the lowest electron and hole wave functions $|eh\rangle$ is shown for various radii of Si spherical quantum dots, with the on-site integrals scaled by the factor f. That is $\omega \to f\omega$ from the values in Tables 3.2, 3.3, and 3.4. The off-site integrals are only indirectly scaled through the on-site integrals in the Ohno formula, Eq. (3.24). The Coulomb energy is normalized by its value at $f = 1$. As the dot size increases, the Coulomb energy becomes significantly less sensitive to variations in the on-site and nearest-neighbor integrals.

independent of the on-site integral values:

$$\omega^0_{\text{Coul}}(i\gamma, i'\gamma') \approx \frac{1}{|\mathbf{R}_i - \mathbf{R}_{i'}|} - \frac{1}{2\omega^0_{\text{Coul}}(i\gamma, i\gamma')^2 \, |\mathbf{R}_i - \mathbf{R}_{i'}|^3}. \tag{3.27}$$

The off-site integrals become a point-charge interaction, making the atomic-scale details of the basis orbitals irrelevant in this limit. Since more off-site integrals contribute to the Coulomb energy in larger quantum dots, the Coulomb energy becomes insensitive to the atomic details.

The significance of Fig. 3.3 is that it quantifies this qualitative explanation for decreasing sensitivity with increasing dot sizes. For example, with a targeted 10% accuracy in the Coulomb interaction, only a 50% accuracy for the on-site integrals is needed for dots of radius larger than 30 Å, while for dots of 10 Å radius only a 20% error can be afforded in the on-site integrals. The discussion in Chap. 3.3.2 shows that the dominant integrals must be considered uncertain to about 20-30%. The tight-binding description of Coulomb interaction can therefore be considered reliable for dots with radii larger than 15–20Å.

3.4 Exchange Interactions

One of the interesting issues related to the exchange interaction of an electron-hole pair is its effective range. In the effective mass approximation (EMA), the long-range component of the exchange interactions for optically allowed exciton states vanishes for spherical quantum dots due to spherical symmetries of their electron and hole wave functions [1, 56]. According to the EMA calculations, the exchange interaction between the lowest electron and hole state for spherical quantum dots is given by its short-ranged component:

$$\langle eh|K|eh\rangle = C_{\text{exch}} \left(\frac{a_x}{R}\right)^3 E_x, \tag{3.28}$$

where R is the dot radius, E_x and a_x are the bulk exciton exchange splitting and radius, respectively. The dimensionless constant C_{exch} is 2.111 for spherical quantum dots [1, 56]. In contrast to the EMA calculations, pseudo-potential calculations show that there is a long-range component in the exchange interaction for several direct-gap semiconductor quantum dots [46, 57]. Motivated by the discrepancy between the two models, we investigate the effective range of the exchange interactions in detail with the tight-binding model.

To verify the effective range of the exchange interactions, we impose a cutoff range on the Coulomb potential in the exchange interaction and calculate an exchange energy as a function of the cutoff distance. As the cutoff distance increases for a given electron-hole configuration, the exchange interaction eventually saturates to a final value. If this saturation occurs over just a few atomic sites, we call it short ranged, while long ranged exchange implies that the saturation occurs over distances comparable to the dot size. With the step function $\Theta(r)$, we replace the Coulomb potential with a cutoff potential $\Theta(r_c - |\mathbf{r} - \mathbf{r}'|)/|\mathbf{r} - \mathbf{r}'|$ to obtain an exchange energy as a function of cutoff distance r_c. The unscreened exchange energy with the cutoff potential for the electron-hole state $|eh\rangle$ is

$$\begin{aligned}
& \langle eh|K^0(r_c)|eh\rangle \\
= \; & e^2 \sum_{\sigma,\sigma'} \iint \mathrm{d}^3r' \; \mathrm{d}^3r \frac{\psi_e^*(\mathbf{r}',\sigma')\psi_h^*(\mathbf{r}',-\sigma')\psi_e(\mathbf{r},\sigma)\psi_h(\mathbf{r},-\sigma)}{|\mathbf{r}'-\mathbf{r}|} \; \Theta(r_c - |\mathbf{r}'-\mathbf{r}|) \\
\approx \; & e^2 \sum_{n_1,n_2,\sigma,\sigma'} c^*_{e;n_1\sigma} c^*_{h;n_1-\sigma} c_{e;n_2\sigma'} c_{h;n_2-\sigma'} \; \omega^0_{\text{Coul}}(n_1,n_2) \; \Theta(r_c - |\mathbf{R}_{n_1} - \mathbf{R}_{n_2}|) \\
& + 2e^2 \sum_{n_1,n_2,\sigma,\sigma'} c^*_{e;n_1\sigma} c^*_{h;n_2-\sigma} c_{e;n_2\sigma'} c_{h;n_1-\sigma} \; \omega^0_{\text{exch}}(n_1,n_2),
\end{aligned} \tag{3.29}$$

where the superscript 0 refers to the unscreened interaction. In line with the discrete spatial character of the tight-binding model, we make an approximation that replaces

the true cutoff potential with one based on the site indices $\Theta(r_c - |\mathbf{R}_{n_1} - \mathbf{R}_{n_2}|)$. If there is a long-range exchange interaction, it would stem from the first term of Eq. (3.29) which includes the Coulomb integrals. The second term, the sum of exchange integrals, has only onsite integrals, since all off-site exchange integrals are negligible as shown in Chap. 3.3.2.

To understand the physical origin of the long-range exchange, we expand the exchange interaction K^0 in a multipole expansion:

$$\langle eh|K^0|eh\rangle \approx \sum_{i\neq j} \frac{q(\mathbf{R}_i)^*_{eh}\, q(\mathbf{R}_j)_{eh}}{|\mathbf{R}_i - \mathbf{R}_j|} + \mathcal{O}(|\mathbf{R}_i - \mathbf{R}_j|^{-2}) + \text{on-site int.} \quad (3.30)$$

The last term of Eq. (3.30) referred to as the on-site interaction is composed of the contributions of on-site Coulomb and exchange integrals. The 'exchange charge density' $q(\mathbf{R}_i)_{eh}$ at atom site $\mathbf{R}_i$ with site index i is a monopole moment defined as

$$\begin{aligned} q(\mathbf{R}_i)_{eh} &\equiv e^2 \sum_{\sigma} \int \mathrm{d}\Omega_i\ \psi_e(\mathbf{r},\sigma)\psi_h(\mathbf{r},-\sigma) \\ &= e^2 \sum_{\gamma\gamma'\sigma} c_{e;i\gamma\sigma} c_{h;i\gamma'-\sigma} \int \mathrm{d}^3 r\ \phi_{i\gamma}(\mathbf{r})\phi^*_{i\gamma'}(\mathbf{r}) \\ &= e^2 \sum_{\gamma\gamma'\sigma} c_{e;i\gamma\sigma} c_{h;i\gamma'-\sigma} \delta_{\gamma\gamma'} \\ &= e^2 \sum_{\gamma\sigma} c_{e;i\gamma\sigma} c_{h;i\gamma-\sigma}, \end{aligned} \quad (3.31)$$

where $\int \mathrm{d}\Omega_i$ is defined to integrate only the orbitals on the atom site $\mathbf{R}_i$. For clarity, the tight-binding orbital index n is specifically replaced by the atom-site index i and the orbital-type index γ. Note that the final expression for $q(\mathbf{R}_i)_{eh}$ has a sum over only one orbital-type index due to the assumed orthogonality of the tight-binding basis orbitals. The distribution of the exchange charge density determines the long-range character of the exchange interaction. If the exchange charge density is zero, that is, the electron and hole states are locally (on-site) orthogonal, there is no exchange

interaction beyond the on-site contribution according to Eq. (3.30). In contrast, if the exchange charge density is nonzero due to the local nonorthogonality of the electron and hole wave functions from site to site, a long-range exchange interaction is caused by the monopole-monopole interaction.

For Si, Figure 3.4 shows that for the exchange interaction between the lowest electron and hole state, there is a region of strong oscillations below a cutoff distance of 15 Å. The strong oscillations are due to the phase difference between the electron and hole states stemming from their different locations in k-space for an indirect-gap material. The oscillations die out beyond a cutoff distance of about 15 Å, suggesting that the effective range of the exchange interaction in Si quantum dots is around 15 Å regardless of dot size. This short-ranged and oscillatory behavior is universal within the configurations near the band edges.

For the direct-gap InAs and CdSe quantum dots, we calculate the unscreened exchange interaction as a function of cutoff distance for several of the lowest electron-hole configurations. We label the electron and hole states by the dominant angular momentum character of their envelope functions. Here, the envelope function refers to the coefficient of the dominant basis orbital. The s and p basis orbitals are typically dominant in the electron and hole states, respectively. To be clear about our notation, 's-like hole' means that the coefficients of the p basis orbital has s symmetry in real space over the whole dot, whereas 'p-like hole' means that the coefficients of the p basis orbital has p symmetry. For electron states, the coefficients of the s basis orbital are used to label the wave functions. For example, 's-like electron' means that the coefficients of the s basis orbital has s symmetry, while 'p-like electron' has p symmetry in the coefficients of the s orbital. In our calculations, a p-like hole is the lowest hole

state and an s-like hole is the second-lowest hole state, whereas an s-like and p-like electron are the lowest and second-lowest electron state. The order of the lowest and second lowest hole states in terms of their envelope function symmetries are opposite to that predicted by the EMA model [26]. In pseudo-potential calculations [18], the hole wave functions exhibit a strong mixing of different angular momentum envelope functions. The mixing is also observed in the tight-binding wave functions of excited electron and hole states.

As shown in Figures 3.5 and 3.6, direct-gap quantum dots show a qualitatively different behavior of the exchange interaction with respect to the cutoff distance from the behavior for Si. First, since there is no overall phase difference between the electron and hole states, there is no region with oscillations for small cutoff distances. Second, the exchange interaction for a particular electron-hole pair can grow continuously up to the dot radius. The figures show that the exchange interaction of direct-gap materials is generally long ranged, extending over the whole dot.

To understand why some electron-hole configurations have a slowly varying long-range exchange interaction, we analyze the long-range component by a multipole-expansion as written in Eq. (3.30). The leading term of the long-range exchange interaction is the monopole-monopole interaction. Therefore, the distribution of the monopole moment, or the 'exchange charge density' defined in Eq. (3.31), determines the range of the long-range exchange interaction.

The exchange charge density of an electron-hole pair has zero total charge due to the orthogonality between the electron and hole wave functions. There are two ways to satisfy this condition: the electron and hole states are either locally orthogonal, which is enforced in the effective mass theory due to the orthogonality between the

Bloch functions of the valence and conduction bands, or globally orthogonal which is possible in the atomistic pseudo-potential and tight-binding theories. If the former is true, the exchange charge density would be zero at each site and there would be no monopole–monopole interaction. That would make the exchange interaction of the electron-hole pair short ranged. By contrast, without onsite orthogonality the exchange charge density has nonzero values, causing monopole-monopole interactions that lead to significant long-range exchange interactions.

To show that the character of the orthogonality of the electron-hole configuration determines the long-range behavior of the exchange interaction, we plot in Figure 3.7 the exchange charge density of two electron-hole configurations in CdSe that have a long-range exchange interaction. Figure 3.7 shows the exchange charge densities of (a) the s-like electron and s-like hole configuration, and of (b) the p-like electron and s-like hole configuration in a plane going through the center of the dot for CdSe with radius 21 Å. This figure shows that there is no local orthogonality between the electron and hole wave functions. The orthogonality of the electron and hole wave functions are instead satisfied by a p-like global oscillation (case a) or a $2s$-like global oscillation (case b). These shapes of the global oscillations explain why the exchange interaction has growing and decaying regions over global distances as shown in Figures 3.5 and 3.6. Those electron-hole configurations that do not have a long-range exchange interaction have a much smaller exchange charge density than those configurations that do have the long-range exchange interaction. These results show that local nonorthogonality of the electron and hole wave functions leads to a strong

monopole–monopole interaction, and that the global variations in the exchange interaction depend on the particular way in which the exchange charge density globally sums to zero for a specific electron-hole configuration.

3.5 Oscillator Strengths

In this section, we calculate the oscillator strength of the exciton level to determine optically allowed levels. The oscillator strength of the electron-hole basis state $|eh\rangle$ is defined as

$$S(E_{\mathrm{eh}}) = \frac{2m_e}{\hbar} E_{\mathrm{eh}} |\langle \mathrm{eh}|\hat{\mathbf{r}}|0\rangle|^2, \tag{3.32}$$

where m_e is the electron mass. The matrix element $\langle \mathrm{eh}|\hat{\mathbf{r}}|0\rangle$ is the dipole moment between initial state $|0\rangle$ with no electron-hole pair and final state $|\mathrm{eh}\rangle$ with an electron-hole pair. The exciton absorption spectrum is given by

$$\sigma_{\mathrm{abs}}(E) \sim \sum_{\mathrm{eh}} S(E_{\mathrm{eh}}) \delta(E - E_{\mathrm{eh}}). \tag{3.33}$$

To mimic thermal broadening, exciton life times, etc, the exciton absorption peaks are broadened with a Gaussian function:

$$\sigma_{\mathrm{abs}}(E) \sim \sum_{\mathrm{eh}} S(E_{\mathrm{eh}}) \exp\left[-(E - E_{\mathrm{eh}})^2/\sigma^2\right], \tag{3.34}$$

where σ is the linewidth of the Gaussian function, which is set to be 10 meV in this work.

The dipole moment in the oscillator strength is naturally divided into two parts. A single-particle state in the tight-binding model is composed of two functions: (i) an envelope function describing the global variation and (ii) a basis orbital describing the local variation. To match the composition of the state, the dipole moment operator $\hat{\mathbf{r}}$

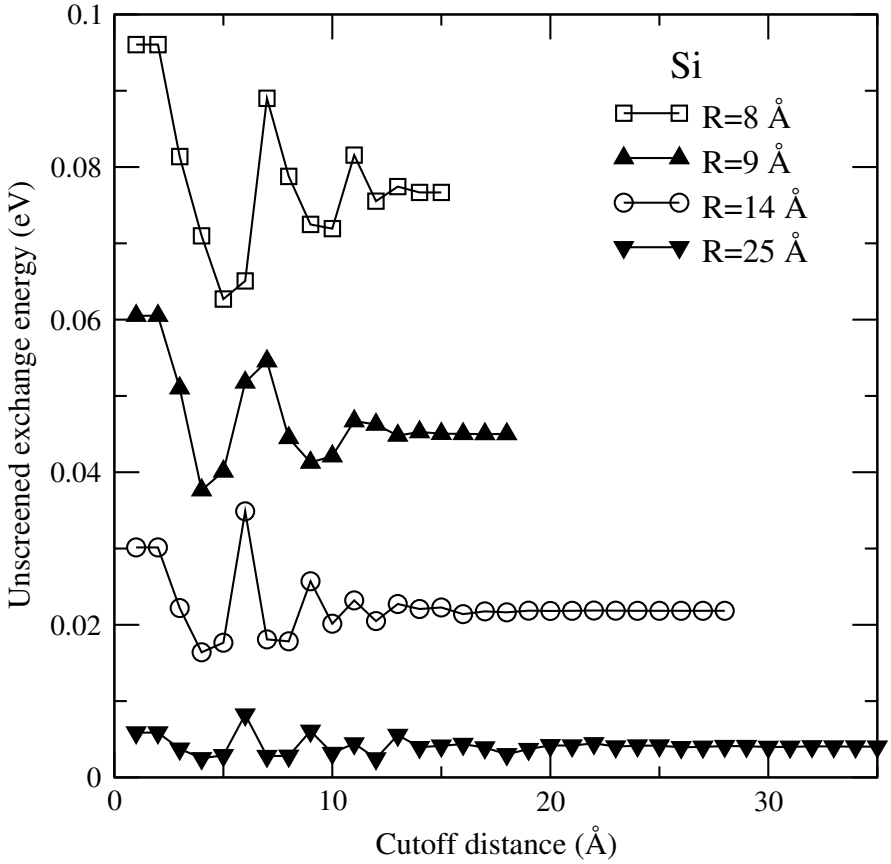

Figure 3.4: Unscreened exchange energy, Eq. (3.29), as a function of the cutoff distance, with the Coulomb potential replaced by a cutoff potential for various radii of Si spherical quantum dots. The energies are for the lowest electron and hole wave functions. All the curves show that there is an oscillation region for small cutoff distances followed by a saturation region beyond 15 Å. This saturation suggests that the effective range of the exchange interaction in Si quantum dots is around 15 Å regardless of the dot radius.

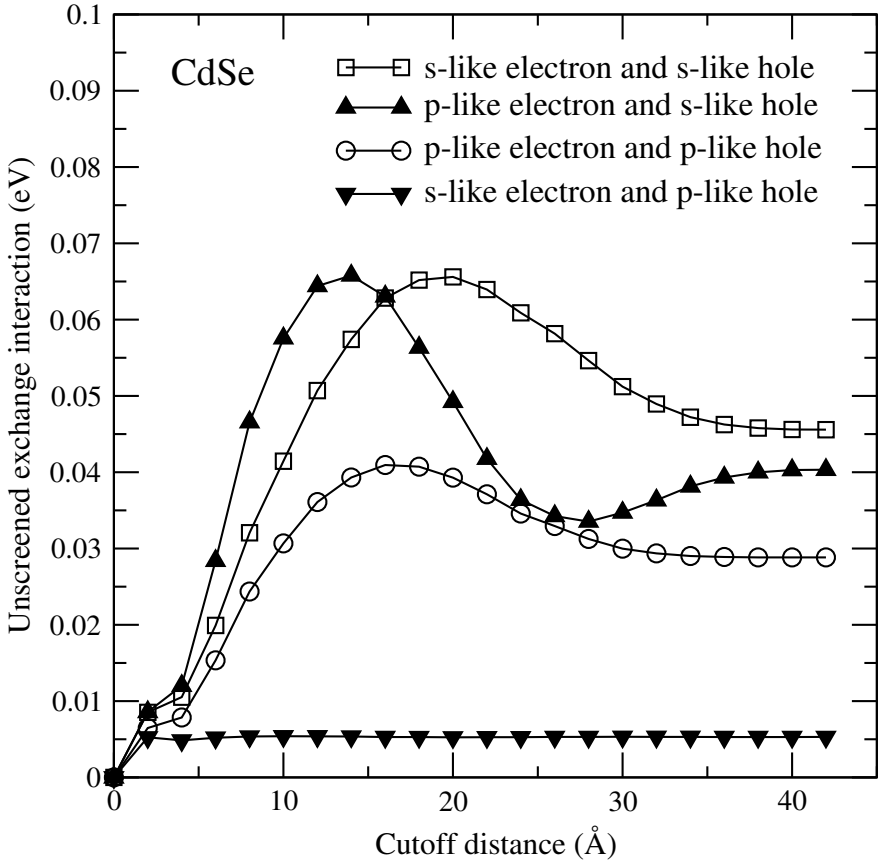

Figure 3.5: Unscreened exchange energy, Eq. (3.29), as a function of cutoff distance, with the Coulomb potential replaced by a cutoff potential for the CdSe spherical quantum dot of radius R=21 Å. The unscreened exchange energy of four different types of electron-hole configurations is shown. The electron and hole configurations are labeled by the dominant angular-momentum component of their envelope functions [58]. Except for the s-like electron and p-like hole configuration, the variation of the exchange interaction extends over the whole dot.

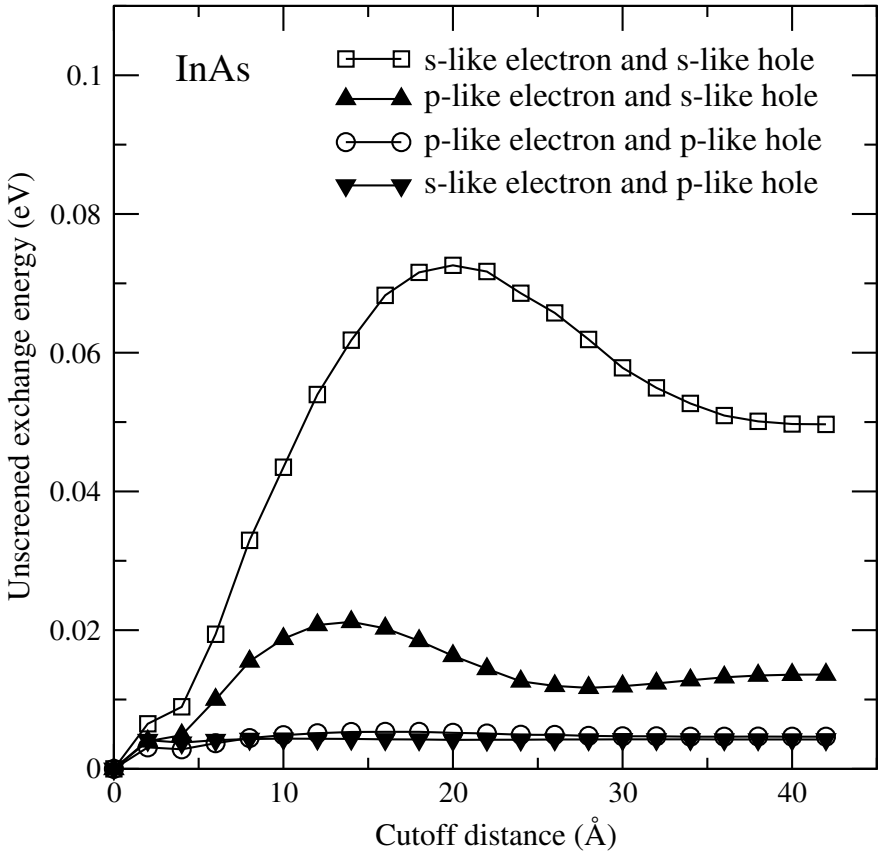

Figure 3.6: Unscreened exchange energy, Eq. (3.29), as a function of cutoff distance, with the Coulomb potential replaced by a cutoff potential for the InAs spherical quantum dot of radius R=21 Å. The unscreened exchange energy of four different types of electron-hole configurations is shown. The electron and hole configurations are labeled by the dominant angular-momentum component of their envelope functions [58]. Long-range exchange interactions appear for the s-like hole with both s-like electron and p-like electron.

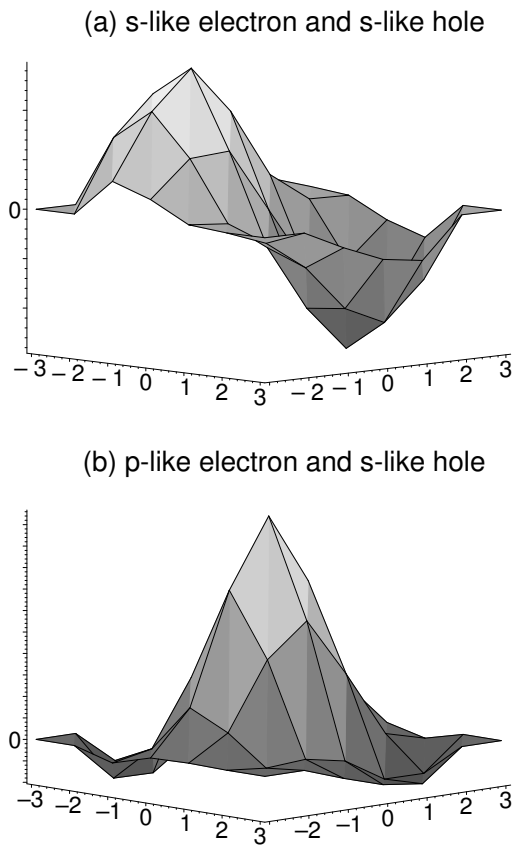

Figure 3.7: Exchange charge densities $q(\vec{R})_{eh}$ from Eq. (3.31) of (a) the s-like electron and s-like hole configuration, and of (b) the p-like electron and s-like hole configuration for the CdSe quantum dot with radius 21 Å. The exchange charge density is plotted in a plane through the center of the dot. The unit of the horizontal axes is the lattice constant of CdSe. The plots show that the orthogonality between the electron and hole wave functions is global not local, with a p-like oscillation or a $2s$-like oscillation. These global oscillations of the exchange charge density lead to the long-range variation of the exchange energies in Fig. 3.5.

is decomposed into a discrete position vector operator $\hat{\mathbf{r}}_i$ of atom site i and a relative position vector operator $\delta\hat{\mathbf{r}}_i = (\hat{\mathbf{r}} - \hat{\mathbf{r}}_i)$ [20]. With this decomposition, the dipole moment matrix element becomes

$$\begin{aligned}\langle \mathrm{eh}|\hat{\mathbf{r}}|0\rangle &= \sum_{ii'\gamma\gamma'\sigma} c^*_{\mathrm{e};i'\gamma'\sigma} c^*_{\mathrm{h};i\gamma-\sigma}[\mathbf{r}_i\delta_{ii'}\delta_{\gamma\gamma'} + \langle i'\gamma'|\delta\hat{\mathbf{r}}_i|i\gamma\rangle] \\ &\approx \sum_{i\gamma\gamma'\sigma} c^*_{\mathrm{e};i\gamma'\sigma} c^*_{\mathrm{h};i\gamma-\sigma}[\mathbf{r}_i\delta_{\gamma\gamma'} + \langle i\gamma'|\delta\hat{\mathbf{r}}_i|i\gamma\rangle]. \qquad (3.35)\end{aligned}$$

The second part of the dipole moment is approximated by including only the matrix elements between the basis orbitals on the same atom site. This approximation is reasonable since the retained matrix elements are dominant. The first part of the dipole moment is the dipole moment between the envelope functions of the same orbital, while the second part is that between the envelope functions of different orbitals. From here on, we call the former an *intra-orbital* dipole moment and the latter an *inter-orbital* dipole moment.

In both intra- and inter-orbital dipole moments, the total angular momentum difference ΔJ between electron and hole states should be unity. However, the rule $\Delta J = 1$ is satisfied differently. The decomposition of the dipole moment operator into $\hat{\mathbf{r}}_i$ and $\delta\hat{\mathbf{r}}_i$ leads to the decomposition of the total angular momentum operator $\vec{J}$ into two operators; $\vec{J} = \vec{L} + \vec{j}$ where $\vec{L}$ and $\vec{j}$ are the global angular momentum operator of an envelope function and the local total angular momentum operator of a basis orbital, respectively. The operator $\vec{j}$ is further given by $\vec{l} + \vec{s}$, where $\vec{l}$ and $\vec{s}$ are the angular momentum and spin operator of a basis orbital. With respect to the global L and local j angular momentum eigenvalues, the optical selection rules of the intra- and inter-orbital dipole moments become

$$\Delta L = 1 \text{ and } \Delta j = 0, \qquad \text{for intra-orbital,} \qquad (3.36)$$

Dipole moment	Si (Å)	Cd(Å)	Se(Å)	In(Å)	As(Å)
$\langle s\|\delta\hat{\mathbf{z}}\|p_z\rangle$	0.773 $\hat{z}$	1.264 $\hat{z}$	0.679 $\hat{z}$	1.106 $\hat{z}$	0.754 $\hat{z}$
$\langle s^*\|\delta\hat{\mathbf{z}}\|p_z\rangle$	0.195 $\hat{z}$	0.281 $\hat{z}$	0.108 $\hat{z}$	0.196 $\hat{z}$	0.123 $\hat{z}$
$\langle p_z\|\delta\hat{\mathbf{z}}\|d_{3z^2-r^2}\rangle$	0.216 $\hat{z}$	0.196 $\hat{z}$	0.034 $\hat{z}$	0.116 $\hat{z}$	0.049 $\hat{z}$
$\langle p_x\|\delta\hat{\mathbf{z}}\|d_{zx}\rangle$	0.187 $\hat{z}$	0.169 $\hat{z}$	0.029 $\hat{z}$	0.101 $\hat{z}$	0.043 $\hat{z}$
$\langle p_y\|\delta\hat{\mathbf{z}}\|d_{yz}\rangle$	0.187 $\hat{z}$	0.169 $\hat{z}$	0.029 $\hat{z}$	0.101 $\hat{z}$	0.043 $\hat{z}$

Table 3.7: Nonzero local dipole moments between basis orbitals for Si, Cd, Se, In, and As atoms with a dipole operator in z direction. The real space description of the basis orbitals is represented by Slater orbitals [51]. The dipole moments are calculated with a numerical integration with the Simpson's rule [59] for radial parts and an exact integration for angular parts. The unit for the dipole moments is Å.

$$\Delta L = 0 \text{ and } \Delta j = 1, \qquad \text{for inter-orbital.} \tag{3.37}$$

Table 3.7 lists the pairs of basis orbitals that have nonzero local dipole moments because they satisfy the selection rule $\Delta j = 1$. The dipole moments of those pairs are evaluated with a numerical integration with Simpson's rule [59] for the radial part and an exact integration for the angular part. The calculated dipole moments are listed in Table 3.7. An alternative way to determine the dipole moments is to fit them to bulk absorption spectra [20].

3.6 Exciton Levels

Depending on whether to include correlation effects or not, we apply the configuration interaction or the perturbation theory to solve the effective electron-hole Hamiltonian $H_{\mathrm{e-h}}$ given by Eq. 3.4. In the configuration interaction scheme, we include sufficient electron and hole states to converge the lowest exciton energies to within a few meV. The typical number of states included in the configuration interaction is 20 to 30. Within the configuration interaction, the exciton state $|ex\rangle^{\mathrm{CI}}$ is a

linear combination of the electron-hole basis states $|eh\rangle$s, and the exciton energy E_{ex}^{CI} is the eigenvalue of the effective electron-hole Hamiltonian:

$$|ex\rangle^{\mathrm{CI}} = \sum_{eh=1}^{N} c_{eh}|eh\rangle, \tag{3.38}$$

$$E_{ex}^{\mathrm{CI}} = {}^{\mathrm{CI}}\langle ex|H_{\mathrm{e-h}}|ex\rangle^{\mathrm{CI}}, \tag{3.39}$$

where N is the number of electron-hole basis states included in the configuration interaction. In the perturbation scheme, an electron-hole pair state is treated as an exciton state, and an exciton energy is approximated by the sum of the electron and hole energies and the first-order corrections of the electron-hole Coulomb and exchange interactions:

$$|ex\rangle^{\mathrm{PT}} = |eh\rangle, \tag{3.40}$$

$$E_{ex}^{\mathrm{PT}} = E_e + E_h + {}^{\mathrm{PT}}\langle ex|J|ex\rangle^{\mathrm{PT}} + {}^{\mathrm{PT}}\langle ex|K|ex\rangle^{\mathrm{PT}}. \tag{3.41}$$

The energy E_{ex}^{CI} includes correlation effects, while the energy E_{ex}^{PT} excludes. Therefore, we define the difference between the two energies as correlation energy Δ_{corr}:

$$\Delta_{corr} = E_{ex}^{\mathrm{CI}} - E_{ex}^{\mathrm{PT}}. \tag{3.42}$$

Replacing E_{ex}^{PT} with Eq. 3.41 shows the constituents of E_{ex}^{CI}:

$$E_{ex}^{\mathrm{CI}} = E_e + E_h + {}^{\mathrm{PT}}\langle ex|J|ex\rangle^{\mathrm{PT}} + {}^{\mathrm{PT}}\langle ex|K|ex\rangle^{\mathrm{PT}} + \Delta_{corr} \tag{3.43}$$

3.6.1 Si Quantum Dots

The lowest exciton energies calculated with the tight-binding parameters Si^B and Si^C listed in Table 2.1, which gives good effective masses, are in significantly better agreement with experiments than those with the parameters Si^A in Table 2.1. The difference between the two parameter sets lies in effective masses described by the

parameters. The parameters Si^B and Si^C reproduce effective masses close to experiments while Si^A gives poor effective masses (see Table 2.2). Note that Si^B is used for conduction levels while Si^C for valence levels. The lowest exciton energies, namely exciton gaps, are calculated with the configuration interaction to include correlation effects. Figure 3.8 shows that the exciton gap with Si^A gives a discrepancy as large as 0.4 eV compared with experimental data [60]. In contrast, the exciton gaps with Si^B and Si^C agree closely with experiments within an error of <0.1 eV (<5%). This improvement shows that the good description of effective masses is essential to accurately predict exciton energies.

To further examine the effect of changing parameters, we compare the electron-hole interaction energies with the two parameter sets: (i) Si^A and (ii) Si^B and Si^C. In particular, we compare the Coulomb shift defined as the energy difference between the single-particle gap and the exciton gap. Figure 3.9 shows that the Coulomb shifts from the two parameter sets are very similar. This insensitivity indicates that the better description of the exciton gap with the second parameter set is mainly due to the better single-particle energies and not from a change in the Coulomb matrix elements.

3.6.2 CdSe Quantum Dots

Figure 3.10 shows that exciton gaps of CdSe dots calculated with the configuration interaction agree well with experimental gaps [27]. The difference between the calculated and experimental gaps is less than 3% (70 meV). The single-particle gap is also plotted in Fig. 3.10. The Coulomb shift, the difference between the single-particle gap and the exciton gap, ranges from 0.4 eV to 0.1 eV as the dot radius varies from

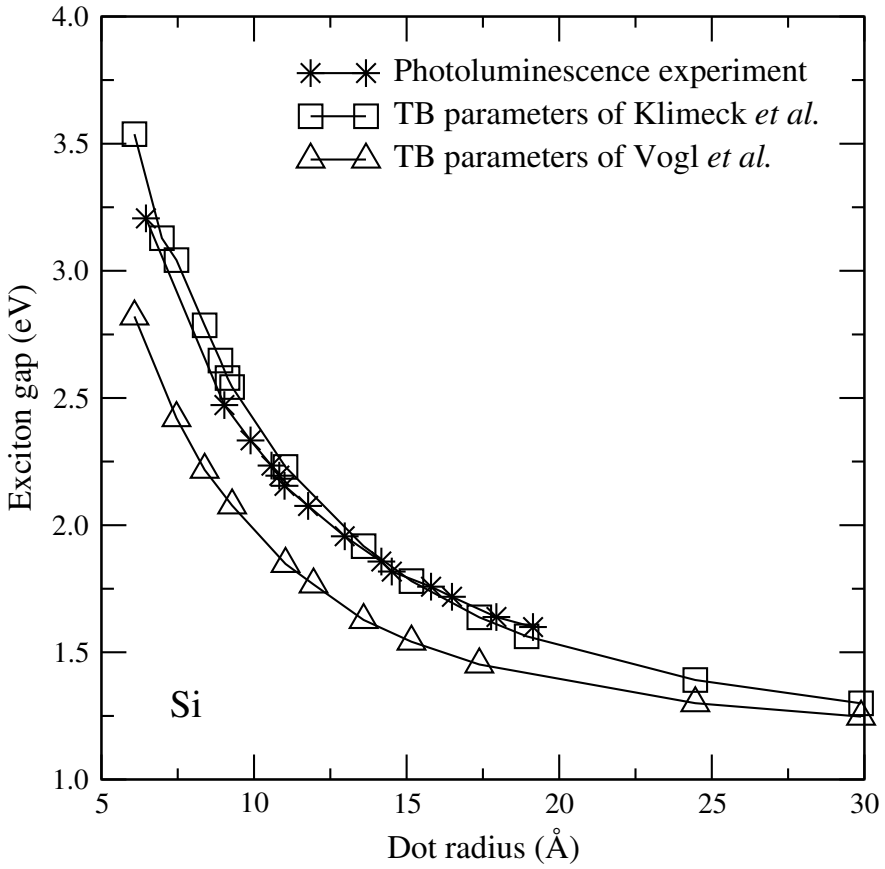

Figure 3.8: Exciton gap of Si spherical quantum dots versus dot radius. The photoluminescence data are taken from Ref. [60]. The other two sets of exciton gaps are calculated with the tight-binding parameters of Vogl *et al.* [36] and Klimeck *et al.* [38] listed in Table 2.1, respectively. The Klimeck parameters give significantly better agreement with the experiment than the Vogl parameters. This good agreement is due to the improved effective masses obtained with the Klimeck parameters.

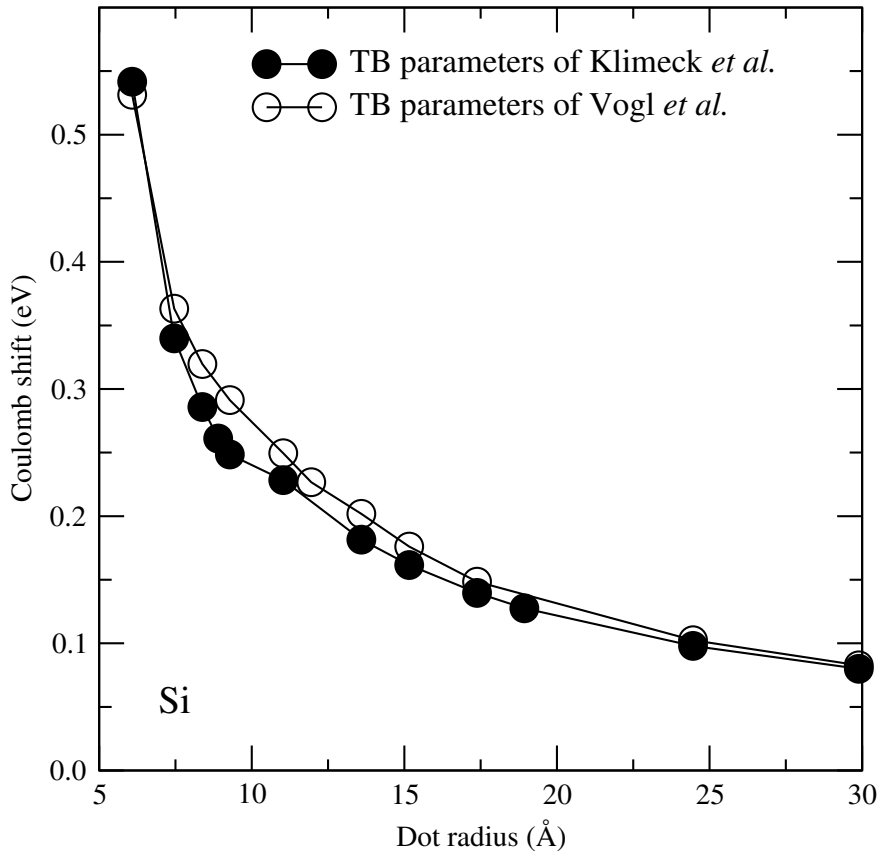

Figure 3.9: Coulomb shift versus dot radius. The Coulomb shift defined as the difference between the single-particle gap and the exciton gap is calculated with two different tight-binding parameter sets: the set of Vogl *et al.* [36] and the set of Klimeck *et al.* [38] listed in Table 2.1. The Coulomb shift does not vary much between the two parameter sets.

10 Å to 40 Å. Pseudo-potential calculations [35] underestimate the exciton gap by ∼0.3 eV. The Coulomb shifts predicted by the pseudo-potential model are comparable with our calculations.

Figure 3.11 plots correlation, Coulomb, and exchange energies contributing to the exciton gap with respect to dot radius R. The correlation energies, defined in Eq. 3.42, are about -10 meV and scales as $-R^{-0.86}$. The Coulomb and exchange energies are the first order corrections of the electron-hole Coulomb and exchange interactions to the exciton gap. The Coulomb energy scales as $-R^{-1.24}$, while the exchange energy as $R^{-3.10}$. These scaling behaviors are similar to those predicted by the effective mass approximation, i.e. $-R^{-1}$ for the Coulomb energy and R^{-3} for the exchange energy. [16] The Coulomb energies are 2-3 orders of magnitude larger than the exchange energies. The exchange energy decreases quickly as the dot size increases, yielding an exchange energy smaller than a correlation energy.

3.6.3 InAs Quantum Dots

For InAs quantum dots, we calculate low-lying exciton energies with the perturbation theory, but not with the configuration interaction since the studies of Si and CdSe dots show that correlation energies are smaller than our accuracy level 10 meV for dot radii we consider (R >10 Å). Within the perturbation theory, we calculate exciton absorption spectra using Eq. 3.34. Figure 3.12 presents the exciton absorption spectra calculated with the $sp^3d^5s^*$ model using the parameter set listed in Table 2.1. As the radius increases, exciton energies decrease and their energy spacings become smaller. However, the absorption rate of each exciton level remains relatively unchanged. The lowest exciton level indicated by the arrow in Fig. 3.12 always shows

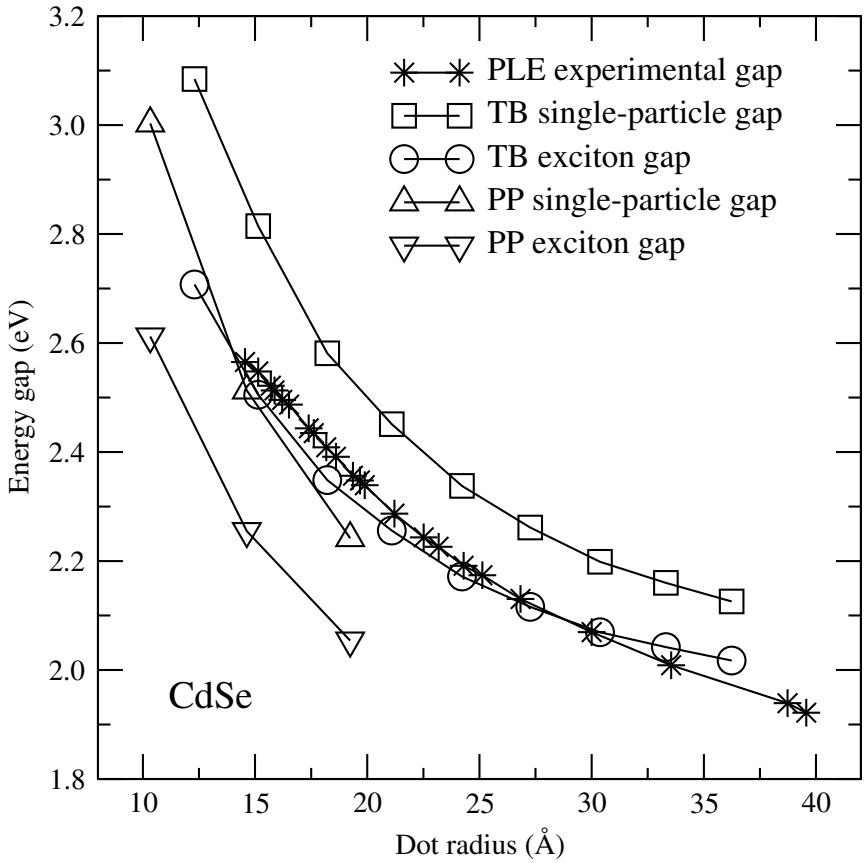

Figure 3.10: Exciton gap and single-particle gap of CdSe dots vs. dot radius. The photoluminescence excitation (PLE) experimental gaps are taken from Ref. [27]. The exciton gaps of the pseudo-potential (PP) calculations [35] are about 0.15 eV smaller than the experimental gaps. Our exciton gaps are in good agreement with the experimental gaps.

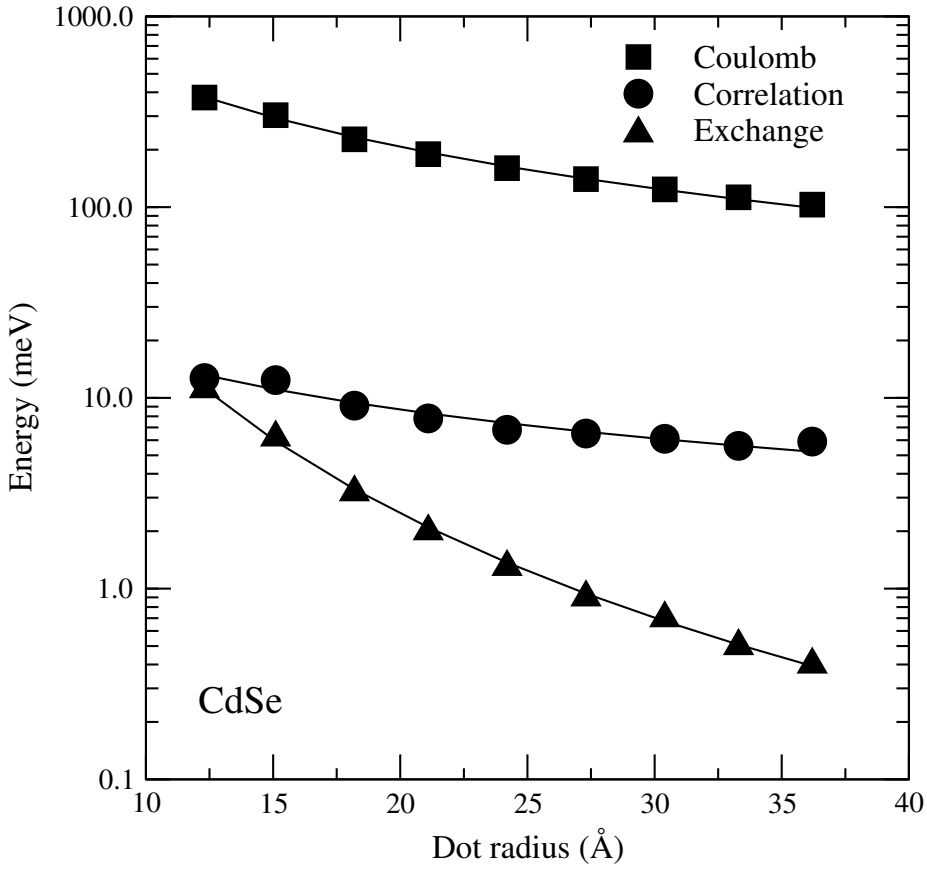

Figure 3.11: Coulomb, exchange, and correlation energies for the exciton gap of CdSe quantum dots vs. dot radius R. The Coulomb and exchange energies are the first-order correction of electron-hole Coulomb and exchange interactions to the exciton gap, and the correlation energy is defined in Eq. 3.42. The Coulomb and correlation energies are negative, but plotted as positive to compare their magnitudes with the positive exchange energy. The lines are $R^{-1.24}$, $R^{-3.10}$, and $R^{-0.86}$ fits for the Coulomb, exchange, and correlation energies, respectively. The correlation coefficients of the fits are >0.97. The scaling laws for the Coulomb and exchange energies are similar to those predicted by the effective mass approximation. [16]

a weak oscillator strength regardless of the dot radius. The first three bright-exciton levels are identified by the first three pronounced peaks of the absorption spectra as shown in Fig. 3.12. We label the first three bright-exciton levels B1, B2, and B3, respectively. Table 3.8 lists the electron and hole levels of B1, B2, and B3.

To examine the effect of the inclusion of spin-orbit coupling and d orbitals, we also calculate exciton absorption spectra with the sp^3s^* tight-binding models including and excluding spin-orbit coupling. Figure 3.13 presents absorption spectra calculated with the two models in comparison with the spectrum calculated with the $sp^3d^5s^*$ model. The dot radius for these absorption spectra is 25 Å. The inclusion of spin-orbit coupling increases the exciton energies by 50–100 meV. The inclusion of d orbitals further increases the energies by ∼100 meV. For all these absorption spectra, the lowest exciton level indicated by the arrow in Fig. 3.13 shows a weak oscillator strength. Especially when spin-orbit coupling is excluded, the oscillator strength of the lowest exciton level is zero.

The increase of the exciton energies due to the inclusion of spin-orbit coupling and d orbitals can be explained by changes in the effective masses of electrons and holes. When spin-orbit coupling is excluded, the highest valence band consists of four-fold heavy-hole band and two-fold light-hole band. In contrast, the inclusion of spin-orbit coupling splits the band into three bands, two-fold heavy-hole band, two-fold light-hole band, and two-fold spin-split band, as shown in Fig. 2.1. The effective-mass of the spin-split band is lighter than that of the heavy-hole band. Therefore, the averaged effective mass of the valence band becomes lighter with spin-orbit coupling included. The effect of the inclusion of d orbitals is subtle as shown in Fig. 2.2. Near the Γ point, the bulk band structure does not change as the d orbitals are included.

However, as k points move away from Γ, the band curvature of the lowest conduction band becomes larger and those of the three highest valence bands become smaller. Therefore, overall lighter electrons from the conduction band give rise to the increase of exciton energies. Likewise, overall heavier holes from the valence band lead to the decrease of exciton energies. The increase of the exciton energies due to the lighter electron is larger than the decrease of the exciton energies due to the heavier hole, yielding the increased exciton energies with d orbitals included.

Figure 3.14 shows the size dependences of the first bright-exciton (B1) energies calculated with the three models, in comparison with PLE experiments [26]. The inclusion of spin-orbit coupling and d orbitals leads to a better agreement with PLE experiments for large dots. For small dots, the three models predict strong curvatures of B1 energies in contrast to the flat curvatures of the experimental energies. The effective mass approximation [26] and the empirical pseudo-potential model [18] also predict strong size dependences of B1 energies in small dots. Since the $sp^3d^5s^*$ model describes the best exciton energies for large dots among the three tight-binding models, we focus on the exciton absorption spectra calculated with the $sp^3d^5s^*$ model from here on.

To understand the origin of the large or small oscillator strengths of several low-lying exciton levels, we analyze the angular momenta of the electron and hole envelope functions of the exciton levels. The envelope function is expanded in terms of spherical harmonics $Y_{lm}(\theta, \phi)$ to determine the dominant angular momenta:

$$c_{a;i\gamma\sigma} \equiv c_{a;\gamma}(\mathbf{R}_i) = \sum_{\ell m} \alpha_{\ell m} Y_{\ell m}(\theta, \phi), \tag{3.44}$$

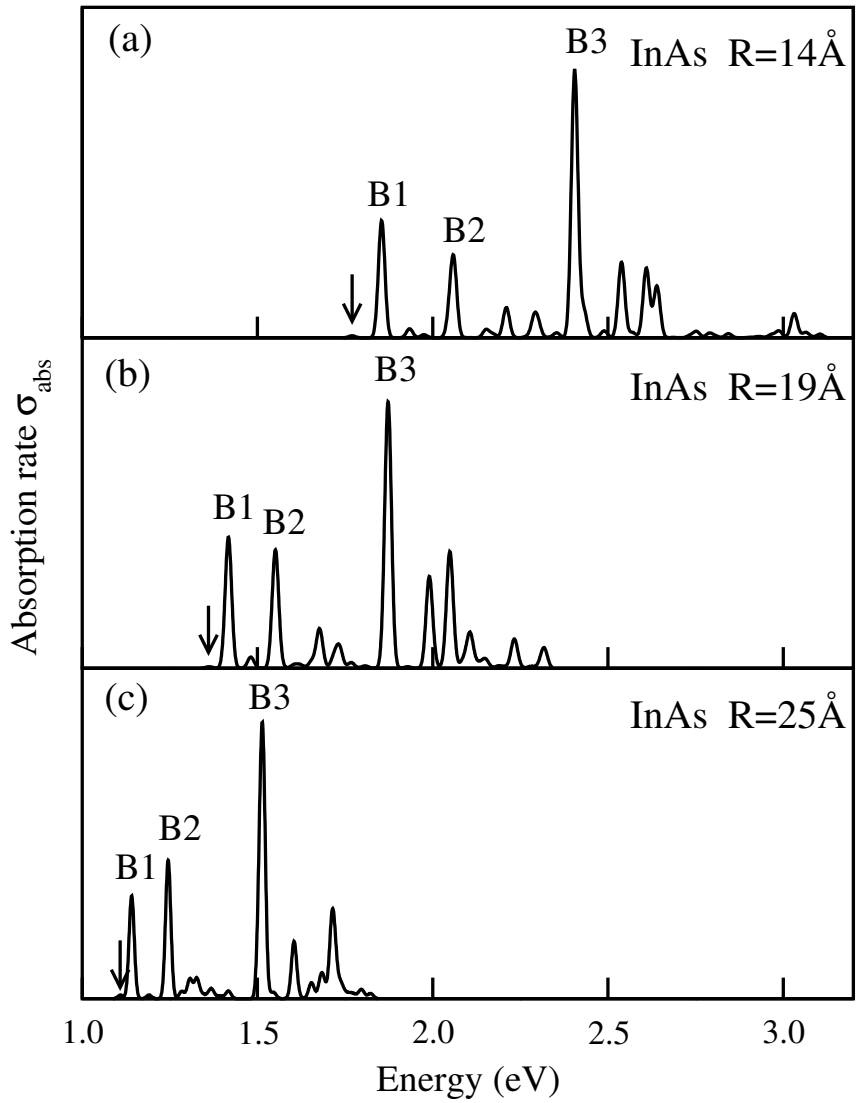

Figure 3.12: Exciton absorption spectra of InAs dots with radius (a) 14 Å, (b) 19 Å, and (c) 25 Å. The absorption spectra are calculated with the nearest-neighbor $sp^3d^5s^*$ tight-binding model using the parameters of Ref. [40]. The arrows indicate the lowest exciton levels which have weak oscillator strengths. The first three pronounced peaks B1, B2, B3 are identified as the first three bright exciton levels.

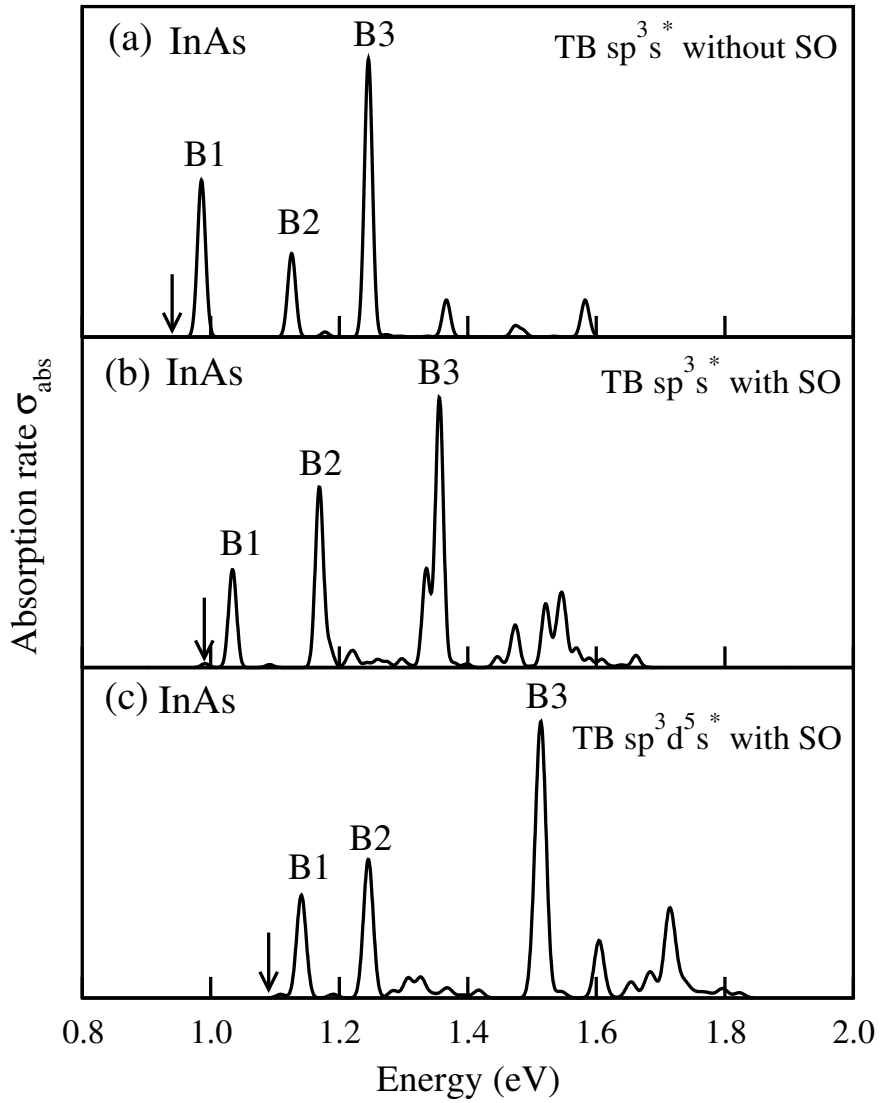

Figure 3.13: Exciton absorption spectra of InAs quantum dots with radius 25 Å, calculated with (a) the sp^3s^* tight-binding (TB) model without spin-orbit (SO) coupling, (b) the sp^3s^* TB model with SO coupling, and (c) the $sp^3d^5s^*$ TB model with SO coupling. Tight-binding parameters for the three models are listed in Table 2.1. The arrows indicate the lowest exciton levels which have weak oscillator strengths. The first three pronounced peaks B1, B2, B3 are identified as the first three bright exciton levels. The inclusion of SO coupling increases exciton energy by 50–100 meV and the inclusion of d orbitals further increases by ∼100 meV.

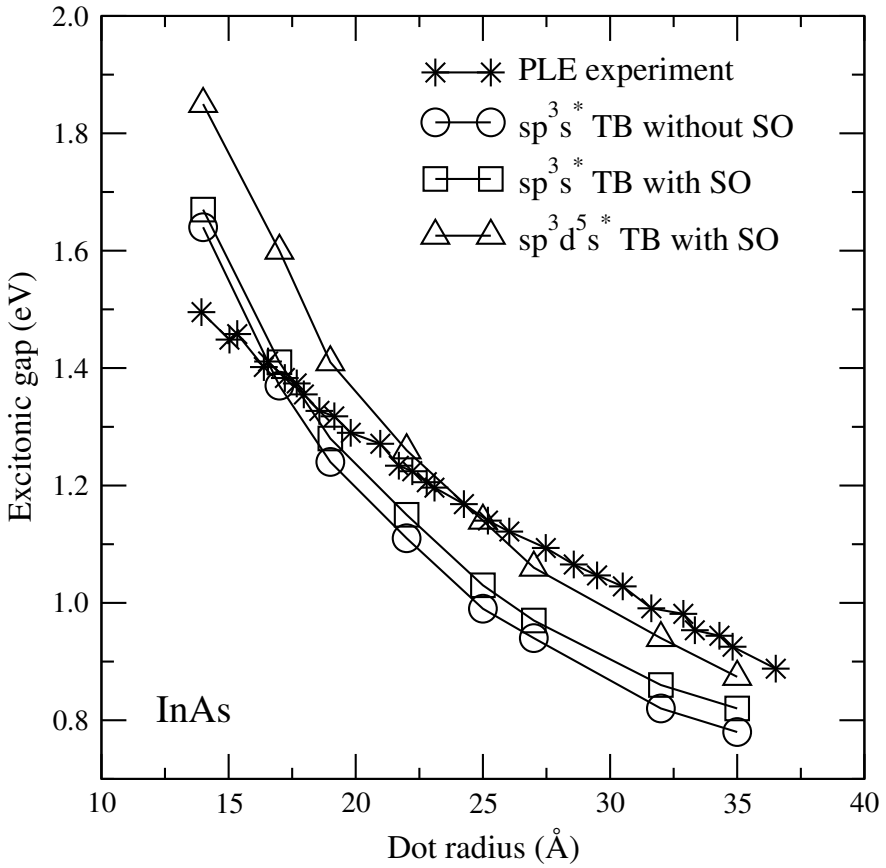

Figure 3.14: Lowest bright-exciton energies of InAs quantum dots versus dot radius. The lowest bright-exciton energies are calculated with the tight-binding (TB) model using three different sets of TB parameters listed in Table 2.1. The inclusion of spin-orbit coupling (SO) and d orbitals raises the energies as much as 0.2 eV, and gives agreement with the gaps measured by photoluminescence excitation (PLE) experiments [26] for large dots. It is not understood why the experimental curve is so much flatter than the theoretical curves.

Level	Composition	$c_{\mathrm{e};s}$	$c_{\mathrm{e};p}$	$c_{\mathrm{h};s}$	$c_{\mathrm{h};p}$
B1	$\mathrm{e}_1 + \mathrm{h}_2$	s-like	p-like	p-like	$(s{+}p)$-like
B2	$\mathrm{e}_1 + \mathrm{h}_5$	s-like	p-like	p-like	$(s{+}p)$-like
B3	$\mathrm{e}_2 + \mathrm{h}_1$	p-like	$(s{+}p)$-like	p-like	p-like

Table 3.8: Electron and hole levels of the first three bright-exciton levels, and the dominant angular momenta of the electron and hole envelope functions. The first three bright-exciton levels are identified by the three pronounced peaks B1, B2, and B3 of absorption spectra shown in Fig. 3.12. The compositions of B1, B2, B3 levels are listed in terms of their electron and hole levels. The nth lowest electron and the nth lowest four-fold hole levels are labeled as e_n and h_n, respectively. The dominant angular momenta of the electron and hole envelope functions are determined by expanding the envelope functions in terms of spherical harmonics. $c_{\mathrm{e};s}$ and $c_{\mathrm{e};p}$ denote the electron envelope function of the s and p orbitals, respectively. Likewise, $c_{\mathrm{h};s}$ and $c_{\mathrm{h};p}$ refer to the hole envelope function of the s and p orbitals, respectively.

where the index a denotes e and h for electron and hole, respectively. The vector $\mathbf{R}_i$ is a position vector of atom site i. The dominant angular momenta of the envelope functions of the three lowest bright-exciton levels are listed in Table 3.8.

The distributions of electron and hole states in terms of orbital types determine which pair of electron and hole envelope functions contributes the most to the oscillator strengths. Table 2.5 shows that the s and p orbitals are the dominant orbitals of electron and hole states, respectively. Moreover, the p orbitals are the most common orbitals between the electron and hole states. Therefore, the principal part of the inter-orbital dipole moment is that between the s-orbital electron and the p-orbital hole envelope functions. Likewise, the principal part of the intra-orbital dipole moment is that between the p-orbital electron and hole envelope functions. These two principal dipole moments contribute the most to the oscillator strengths.

Based on the angular-momentum selection rules of the dipole moments and the dominant angular momenta of the envelope functions, we can answer two important questions: (i) why the lowest exciton level composed of the lowest electron and hole level is dim; and (ii) what makes the bright-exciton levels bright? (Is it the intra-orbital dipole moment, inter-orbital dipole moment, or both?) In the lowest exciton level, the angular momentum selection rules are unsatisfied by the principal parts of the intra- and inter-orbital dipole moments. The small oscillator strength of the lowest exciton level arises from two small parts of dipole moments: (i) the intra-orbital dipole moment between the s-like s-orbital electron and the p-like s-orbital hole envelope function, and (ii) the inter-orbital dipole moment between the p-like p-orbital electron and the p-like s-orbital hole envelope function. Typically, the oscillator strength of the lowest exciton level is smaller by two orders of magnitude than that of bright-exciton levels.

The large oscillator strengths of the bright-exciton levels originate from both large inter- and intra-orbital dipole moments. Unlike the lowest hole level, the second lowest hole level has the (s+p)-like p-orbital envelope function. Therefore, the exciton level B1 made from the first lowest electron and the second lowest hole levels are bright due to the following contributions: (i) the p-like p-orbital electron and the s-like p-orbital hole envelope function yield a large intra-orbital dipole moment; (ii) the s-like s-orbital electron and s-like p-orbital hole lead to a large inter-orbital dipole moment. The intra-orbital dipole moments are typically larger than the inter-orbital dipole moment by a factor of $\sim$10 in terms of their norms [61]. Similar analyses can explain the origin of large oscillator strengths of other bright-exciton levels.

Due to the interplay between quantum confinement and spin-orbit coupling, the order of hole levels changes as a dot size changes. In small dots where level spacings Δ_{qc} due to quantum confinement are larger than spin-orbit splitting energies Δ_{so}, several two-fold hole levels appear in-between four-fold hole levels. However, less two-fold hole levels appear close to the band edges in large dots where Δ_{qc} is smaller than Δ_{so}. In fact, for our biggest dots (R=35 Å) the first four lowest hole levels are four-fold.

The exciton levels composed of the two-fold hole levels near band edges and the lowest electron level are dark. In the exciton levels, the electron and hole envelope functions have the same total local angular momentum ($j = \frac{1}{2}$) and the same global angular momentum ($L = 0$). Since the difference of the total angular momenta between the electron and hole level is zero, the exciton levels are optically forbidden. In higher hole levels, two-fold hole levels with $L = 1$ emerge and they form bright-exciton levels with the lowest electron level. These exciton levels correspond to small peaks between B2 and B3 in Fig. 3.12.

Figure 3.15 presents the size dependences of the three lowest bright-exciton energies identified in the absorption spectra shown in Fig. 3.12. The exciton energies are compared with those of PLE experiments [26]. The calculated energies with radius $R < 20$ Å agree with the experimental energies within a 10% (100 meV) error. However, for smaller dots the calculated energies scale as $R^{-0.8}$ while the experimental energies scale as R^{-n} with $n \approx +0$. Therefore, the discrepancy grows rapidly with decreasing the dot size. The flat curvature of the experimental energies of the small dots

is understood neither by the present tight-binding model nor by other empirical models [18, 26]. The disagreement between our calculations and the experiments in small dots is partly attributed to the uncertainties of experimental size determinations [26].

Since precise experimental size determinations are difficult, it is more reliable to compare exciton energies relative to the lowest bright-exciton energy. Figure 3.16 presents B2 and B3 energies relative to B1 energies with respect to B1 energies. B3 energies agree well with corresponding experimental values, E_5 in Ref. [26], in a wide range of B1 energies. B2 energies agree less well with experimental values, E_3 in Ref. [26], in particular for large B1 energies which correspond to small dots. Moreover, the experimental data for B2-B1 energies show discrete jump around the B1 energy of 1.3 eV, indicating a level crossing. This jump is not predicted by our calculations. The calculated B2 energies agree better with the experiment as a B1 energy decreases, that is, a dot size increases.

Figure 3.16 shows that the present model gives a better description of electron level spacings than hole level spacings. The energy difference between B1 and B2 is roughly the spacing between the second and fifth four-fold hole levels, while the difference between B1 and B3 is the spacing between the first and second electron levels. Since calculated energies B3-B1 agree with experimental values better than B2-B1, the electron level spacing is better described by our model than the hole. This can be explained by the difference between the characters of InAs conduction and valence bands. The lowest conduction band near the Γ point is almost isotropic and has no spin-orbit coupling. In contrast, the highest valence bands are complex due to the anisotropic effective masses of the heavy hole band, and the couplings among the heavy-hole, light-hole, and spin-split bands. Although the coupling between the

conduction and valence bands mixes band contributions to single-particle levels, the main parts of the electron and hole levels are from the conduction and valence bands, respectively. Hence, the complexity of the valence band structure makes it more difficult to obtain a good description for the hole levels than for the electron levels.

3.7 Discussion

In this chapter, we have addressed four relevant questions regarding the modeling of exciton levels near the band edges for both direct-gap and indirect-gap semiconductor quantum dots. First, we examined to what degree the choice of the real-space atomic basis orbitals affects the electron-hole Coulomb interaction. We find that the sensitivity of the Coulomb interaction to the real-space description of the basis orbitals decreases quickly as the dot size increases. Our results shows that tight-binding descriptions of electron-hole Coulomb interactions in quantum dots should be reliable for dots larger than 15–20 Å radius even for simple models for the basis orbitals. More detailed calculations of basis orbitals are required for smaller dots.

Second, we studied the effective range of the electron-hole exchange interaction in a quantum dot. Replacing the Coulomb potential with a cutoff potential, we explored the dependence of the exchange interaction on the cutoff radius. For direct-gap materials, the lack of on-site orthogonality causes the exchange interaction to be long ranged. For an indirect material Si, the calculations show that the exchange interaction is oscillatory and has a range of about 15 Å, regardless of dot radii.

Third, we investigated correlation effects due to the interactions between different electron-hole configurations on exciton energies. For a quantum dot with radius R=10–40 Å, we find that the correlation energy contributing to a low-lying exciton

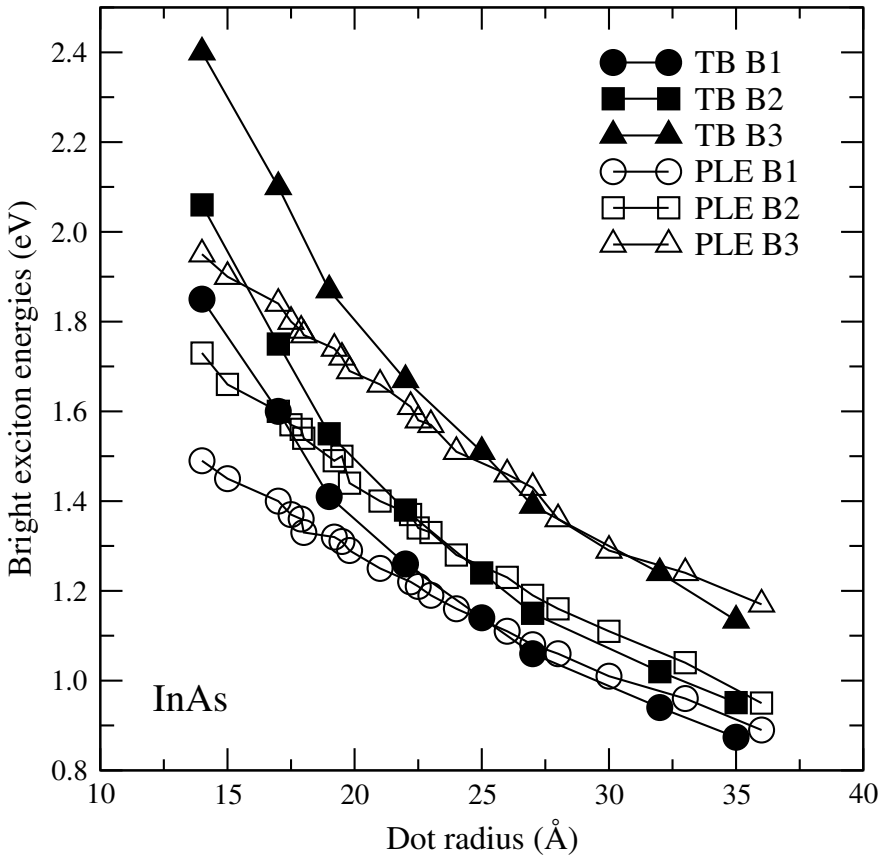

Figure 3.15: Three lowest bright exciton energies of InAs quantum dots vs. dot radius. The three lowest bright exciton energies in the present $sp^3d^5s^*$ tight-binding (TB) model are determined by the energies of the peaks B1, B2, and B3 defined in Fig. 3.12. The present exciton energies are compared with the energies of the first three strong photoluminescence peaks labeled as E_1, E_3, and E_5 in Ref. [26], respectively. The calculated energies agree better with the experimental energies as the dot size increases.

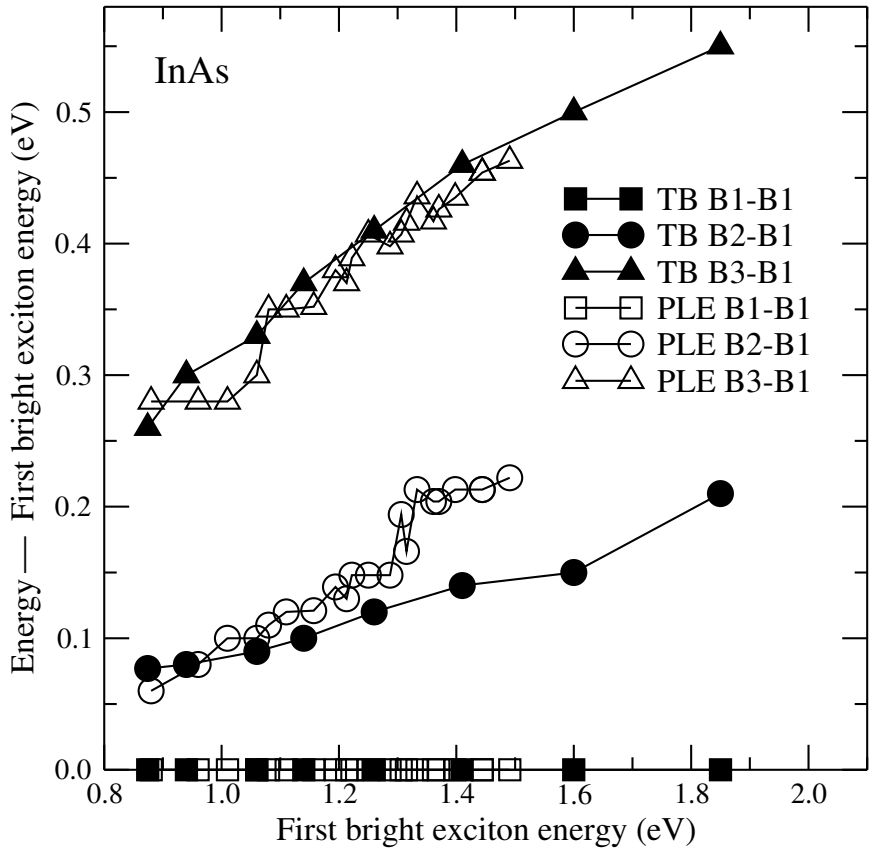

Figure 3.16: First three bright exciton energies relative to the lowest bright exciton energy plotted with respect to the lowest bright exciton energy for InAs quantum dots. The first three exciton energies using the present $sp^3s^5s^*$ tight-binding (TB) model are identified by the peaks B1, B2, and B3 in the absorption spectra shown in Fig. 3.12. The spacings of the identified three exciton energies are compared with the energy spacings of the first three strong photoluminescence peaks labeled as E_1, E_3, and E_5 in Ref. [26], respectively.

energy is about 10 meV. By comparing it with other components of the exciton energy, we find a clear hierarchy of the contributions of the components to the exciton energy for the dot sizes considered in this work. The contribution of a single-particle energy is on the order of 1 eV, that of a Coulomb energy is 100 meV, and that of the exchange energy is 1 meV or smaller. As dot sizes increases, single-particle energy spacings become as small as Coulomb interaction matrix elements between different electron-hole configurations. Therefore, larger correlation energies relative to the other components are expected in larger dots.

Fourth, we tested how well the tight-binding model describes the low-lying exciton levels by comparing with experimental data. For exciton gaps, we obtained good agreement with recent experiments for both Si and CdSe quantum dots. The gaps for InAs quantum dots with radius larger than 20 Å are also in good agreement with experiments. For Si dots, we improved the agreement with experimental data by optimizing the tight-binding parameters to give good effective masses. For InAs dots, we improved the description of exciton energies by including spin-orbit coupling and d orbitals. The inclusion of spin-orbit coupling and d orbitals increases the exciton energies as much as 0.2 eV, yielding better agreement with experiments. We also identified several low-lying bright-exciton energies beyond the exciton gaps for InAs dots by evaluating the oscillator strengths of exciton levels. The identified first three lowest bright-exciton energies are in good agreement with experiments with radius larger than 20 Å. We successfully explained the origins of strong or weak oscillator strengths of the exciton levels in terms of the dominant angular momenta of exciton envelope functions.

CHAPTER 4

MULTIPLY CHARGED QUANTUM DOTS

The whole of science is nothing more than a refinement of everyday thinking.

-Albert Einstein

The success of quantum-dot based, electronic devices relies on the efficiencies and good controls of injecting charge carriers into dots and transporting the carriers between dots. One of the key parameters in controlling the carrier transfer in quantum-dot electronic devices is energies required to transfer charge carriers between metal leads and dots. In this chapter, we model the energies required to add electrons and holes into dots, which are called electron and hole addition energies, respectively. We focus on the addition energies of InAs quantum dots in this work, but the present model can be applied to Si and CdSe dots.

Recently, the electron and hole addition energies of InAs quantum dots were measured by STM experiments.[28] In the experiment, the tunneling current between an STM metallic tip and an InAs dot were measured as a function of bias-voltage. Figure 4.1 shows the STM experimental setup and a schematic diagram of differential conductance of the tunneling current as a function of bias voltage. The STM experimental setup is designed to have most of the bias voltage drop across the junction

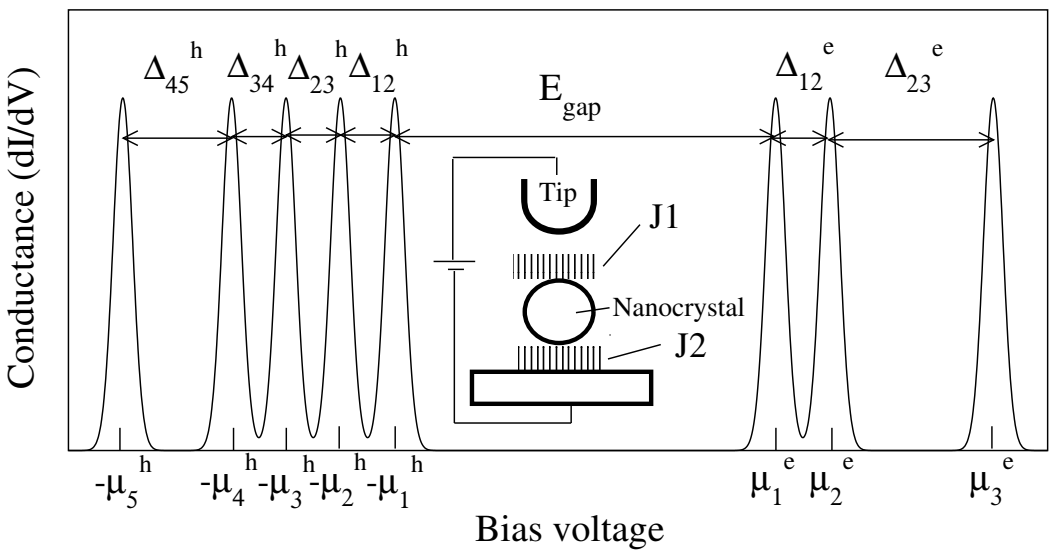

Figure 4.1: Schematic description of a differential conductance spectrum of a quantum dot. Important physical quantities are labeled according to the definitions made in the paper. The inset is a schematic drawing of an STM experimental setup [28].

(J1 in the inset of Fig. 4.1) between the STM tip and the dot [28]. Therefore, we interpret the bias voltage as the STM-tip Fermi energy relative to the dot Fermi energy. Whenever the STM-tip Fermi energy matches the electron and hole addition energies, there is a dramatic increase in the tunneling current. Therefore, the STM-tip Fermi energies (or the bias voltage) of tunneling-conductance peaks correspond to the addition energies.

The addition energies are composed of (i) single-particle energies of a dot and (ii) charging energies for single-electron transfer between a dot and a metal lead [19]. Within the capacitor model, a charging energy for adding an electron or a hole in a system is e^2/C_{eff} where C_{eff} is an effective capacitance of the system. The capacitance C_{eff} depends on the geometry and dielectric constant of the system, but does not

depend on the number of charges nor on the charge distributions in the system. The capacitor model sufficiently describes charging energies when the polarization of a system is a dominant source of the charging energy, and Coulomb interactions between charge carriers are negligible. However, for systems as small as quantum dots, strong quantum confinement enhances the Coulomb interactions. Furthermore, both the polarization and Coulomb energies are sensitive to charge distributions in strongly confined systems. Due to the limits of the capacitor model, we use a different model which includes charge-carrier Coulomb energies and describes charging energies in terms of charge distributions.

4.1 Model

The energy condition for an electron to tunnel from a metal lead to a quantum dot charged with $(n-1)$ electrons is met when the Fermi level of the metal $\mu_{\mathrm{F}}^{\mathrm{M}}$ is resonant with an nth electron addition energy μ_n^{e} of the dot:

$$\mu_{\mathrm{F}}^{\mathrm{M}} = \mu_n^{\mathrm{e}}. \tag{4.1}$$

The nth electron addition energy is composed of three types of energies, i.e.

$$\mu_n^{\mathrm{e}} = E_n^{\mathrm{e}} + \Sigma_n^{\mathrm{pol,e}} + \sum_{i=1}^{n-1} J_{i,n}^{\mathrm{ee}}. \tag{4.2}$$

The first term E_n^{e} is the energy of the nth electron level of the dot. The last two terms account for charging energies due to the polarization of the dot environment and many-body interactions. Specifically, the second term $\Sigma_n^{\mathrm{pol,e}}$ denotes the self-polarization energy of the nth electron. The self-polarization energy is caused by the interaction between one electron and polarized charges at surface included by the electron. Note that the dielectric mismatch between the dot and its surrounding leads

to nonzero net polarized charges at the surface as shown in Fig. 4.2. The third term $J_{i,n}^{\mathrm{ee}}$ represents a Coulomb energy due to the interaction between the nth electron and an electron in the dot. The Coulomb energy $J_{i,n}^{\mathrm{ee}}$ has two components: a direct Coulomb energy $J_{i,n}^{\mathrm{dir}}$ and a polarized Coulomb energy $J_{i,n}^{\mathrm{pol}}$. The direct Coulomb energy results from a Coulomb interaction between two electrons in the absence of the dielectric mismatch at the surface. The polarized Coulomb energy is a correction to $J_{i,n}^{\mathrm{ee}}$ due to the dielectric mismatch. The polarized Coulomb energy is caused by the interaction between one electron and polarized charges at the surface induced by another electron. Figure 4.3 illustrates Coulomb interactions responsible for the self-polarization energy and the polarized Coulomb energy. Note that the exchange interaction between the nth electron and the other electrons in the dot is ignored in the present model since it is smaller than the experimental resolution (~ 10 meV) [28].

An electron can tunnel from a quantum dot charged with $(n-1)$ holes to a metal lead when the Fermi energy of the metal lead is the negative of an nth hole addition energy μ^{h}:

$$\mu_{\mathrm{F}}^{\mathrm{M}} = -\mu_n^{\mathrm{h}}, \tag{4.3}$$

The nth hole addition energy consists of four types of energies:

$$\mu_n^{\mathrm{h}} = E_n^{\mathrm{h}} + \Sigma_n^{\mathrm{pol,h}} + \sum_{i=1}^{n-1} J_{i,n}^{\mathrm{hh}} + W_n. \tag{4.4}$$

Removing an electron from the dot charged with $(n-1)$ holes can be seen as adding an nth hole to the dot. An nth hole level energy E_n^{h} is the negative of the energy of the valence electron removed from the dot. Similar to those in the electron addition energy, the charging energies $\Sigma_n^{\mathrm{pol,h}}$ and $J_{i,n}^{\mathrm{hh}}$ account for a hole self-polarization energy and a hole-hole Coulomb energy, respectively.

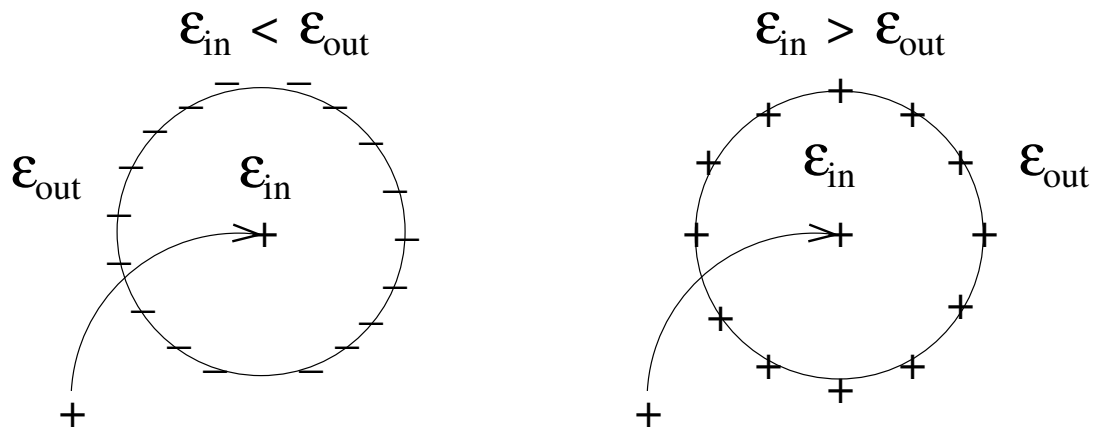

Figure 4.2: Polarized charges at the surface between the dot and its surrounding. When a charge is injected to the dot, a dielectric mismatch between the dot and its surrounding leads to nonzero net polarized charges at the surface. The curved arrow indicates the direction of the charge injection. The sign of the net polarized charges depends on the relative size of the dot's dielectric constant (ϵ_{in}) to the surrounding's dielectric constant (ϵ_{out}).

The last term in Eq. 4.4 represents the work required to remove an electron from the dot and add it to the metal lead in the presence of n holes in the dot. From here on, we call the last term an *electron-removal work function*. The electron-removal work function does not exist in the electron addition energies due to the screening effect of free electrons in the metal. When electrons tunnel from a metal lead to a dot and leave holes in the metal, the electric field generated by the holes is completely screened out by other free electrons in the metal. In other words, the tunneling electron does not see an attractive electric field generated by the holes in the metal. In contrast, when electrons tunnel from a dot to a metal lead, holes left in the dot are only partially screened by valence electrons in the dot. More importantly, the electron-removal work function is different from conventional work functions, which

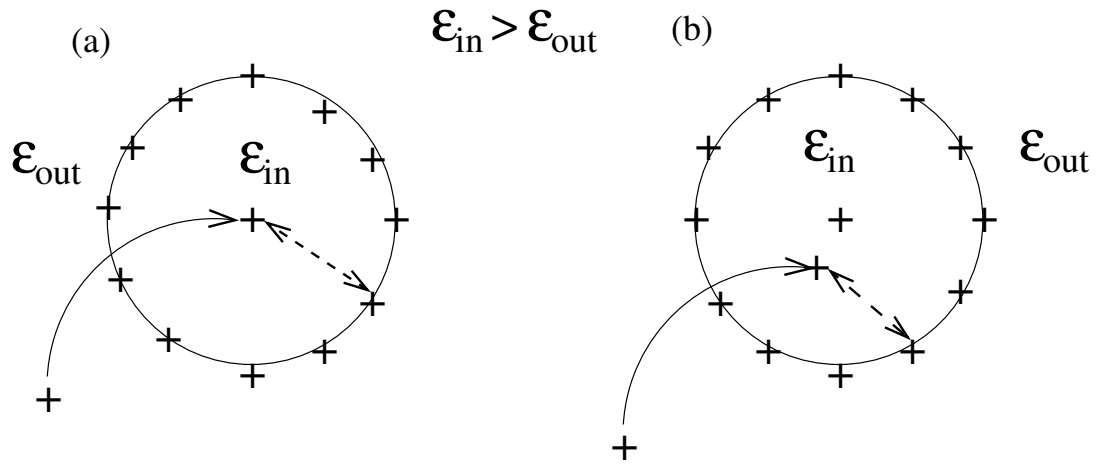

Figure 4.3: Coulomb interactions responsible for (a) self-polarization energies and (b) polarized Coulomb energies. The self-polarization energy results from the Coulomb interaction between one injected electron and polarized charges at the surface included by the injected electron, while the polarized Coulomb energy results from the interaction between one injected electron and polarized charges included by one electron residing in the dot. The curved arrows represents the direction of charge injection. In (b), the symbol + at the center of the dot represents the residing electron while the other + in the dot represents the injected electron. The dashed lines with arrowheads indicate the responsible Coulomb interactions. The polarized charges are illustrated in the case that the dot's dielectric constant ($\epsilon_{\rm in}$) is bigger than the surrounding's dielectric constant ($\epsilon_{\rm out}$). When $\epsilon_{\rm in} > \epsilon_{\rm out}$, the self-polarization energy and the polarized Coulomb energy are positive due to the repulsive Coulomb interaction between the injected electron and the polarized charge. Conversely, when $\epsilon_{\rm in} < \epsilon_{\rm out}$ the energies are negative due to the attractive Coulomb interaction between an injected electron and a polarized charge.

arise from charging distortions at surfaces. Although the conventional work function affects tunneling rates, it does not affect the energy condition of tunneling.

The absolute positions of the conductance peaks measured by STM experiments vary with respect to the Fermi energy of an unbiased STM tip, but spacings between the peaks remain the same. In the present model, the spacings are

$$\begin{aligned}
\Delta^{\mathrm{e}}_{n,n+1} &\equiv \mu^{\mathrm{e}}_{n+1} - \mu^{\mathrm{e}}_{n} \\
&= E^{\mathrm{e}}_{n+1} - E^{\mathrm{e}}_{n} + \Sigma^{\mathrm{pol,e}}_{n+1} - \Sigma^{\mathrm{pol,e}}_{n} + \sum_{i=1}^{n} J^{\mathrm{ee}}_{i,n+1} - \sum_{i=1}^{n-1} J^{\mathrm{ee}}_{i,n}, \qquad (4.5) \\
\Delta^{\mathrm{h}}_{n,n+1} &\equiv \mu^{\mathrm{h}}_{n+1} - \mu^{\mathrm{h}}_{n} \\
&= E^{\mathrm{h}}_{n+1} - E^{\mathrm{h}}_{n} + \Sigma^{\mathrm{pol,h}}_{n+1} - \Sigma^{\mathrm{pol,h}}_{n} + \sum_{i=1}^{n} J^{\mathrm{hh}}_{i,n+1} - \sum_{i=1}^{n-1} J^{\mathrm{ee}}_{i,n} + W_1. \qquad (4.6)
\end{aligned}$$

W_n is roughly n times bigger than W_1, assuming that the charge distribution of holes in the dot is almost spherically symmetric. Therefore, the electron-removal work function difference $W_{n+1} - W_n$ is replaced with W_1 in $\Delta^{\mathrm{h}}_{n,n+1}$. The spacing $\Delta_{n,n+1}$ and the addition energy μ_n are connected with corresponding quantities in a schematic tunneling spectrum plotted in Fig. 4.1.

The single-particle levels of InAs dots for the addition energies are calculated with the tight-binding model described in Chap. 2. We find from the study of exciton levels in Chap. 3 that the inclusion of d orbitals and spin-orbit coupling improves the single-particle energies. Therefore, we choose the $sp^3d^5s^*$ tight-binding model including the spin-orbit coupling to calculate single-particle energies and states. Tight-binding parameters for the model are listed in Table 2.1.

4.2 Charging Energies

The calculation of the charging energies requires a description of the electrostatic potential of a charged dot and the polarized environment. The potential is sensitive to the system geometry. However, since details of the geometry of experimental systems are unavailable [28] we approximate an inhomogeneous dot environment with an infinite uniform dielectric medium [19, 62]. Although this idealized model is not realistic, it captures the effects of a dielectric mismatch at the dot surface on the charging energies [19]. Figure 4.4 shows both realistic and idealized models for the polarization of a charged quantum dot and the dot environment.

When a dot is embedded in an infinite dielectric medium with dielectric constant ϵ_{out}, an electrostatic potential generated by an elementary charge e at point $\mathbf{s}$ inside the dot with dielectric constant ϵ_{in} and radius R is

$$V(\mathbf{r};\mathbf{s}) = V^{\text{dir}}(\mathbf{r};\mathbf{s}) + V^{\text{pol}}(\mathbf{r};\mathbf{s}) \tag{4.7}$$

$$= e\left[\frac{1}{\epsilon_{\text{in}}|\mathbf{r}-\mathbf{s}|} + \frac{\epsilon_{\text{in}}-\epsilon_{\text{out}}}{\epsilon_{\text{in}}R}\sum_{\ell=0}^{\infty}\left(\frac{r}{R}\right)^{\alpha_\ell}\left(\frac{s}{R}\right)^{\ell}\frac{(\ell+1)\mathrm{P}_\ell(\mathbf{r}\cdot\mathbf{s}/rs)}{\epsilon_{\text{out}}+\ell(\epsilon_{\text{in}}+\epsilon_{\text{out}})}\right], \tag{4.8}$$

where α_ℓ is ℓ for r smaller than R, and $-\ell-1$ for r larger than R [62]. The function $\mathrm{P}_\ell(x)$ is a ℓth Legendre polynomial. The first term $V^{\text{dir}}(\mathbf{r};\mathbf{s})$ is a Coulomb potential of the source charge when there is no dielectric mismatch at the surface. The second term $V^{\text{pol}}(\mathbf{r};\mathbf{s})$ results from the polarization of the dielectric medium different from the dot polarization. In connection with the STM experimental setup [28] (see the inset of Fig. 4.1), the second term is attributed to the polarization of the ligands, and the image charges of the STM tip and the metal substrate.

For the potential $V(\mathbf{r};\mathbf{s})$, the dielectric constants of the dot and the dot environment need to be determined. The dielectric constant ϵ_{in} of the dot is modeled

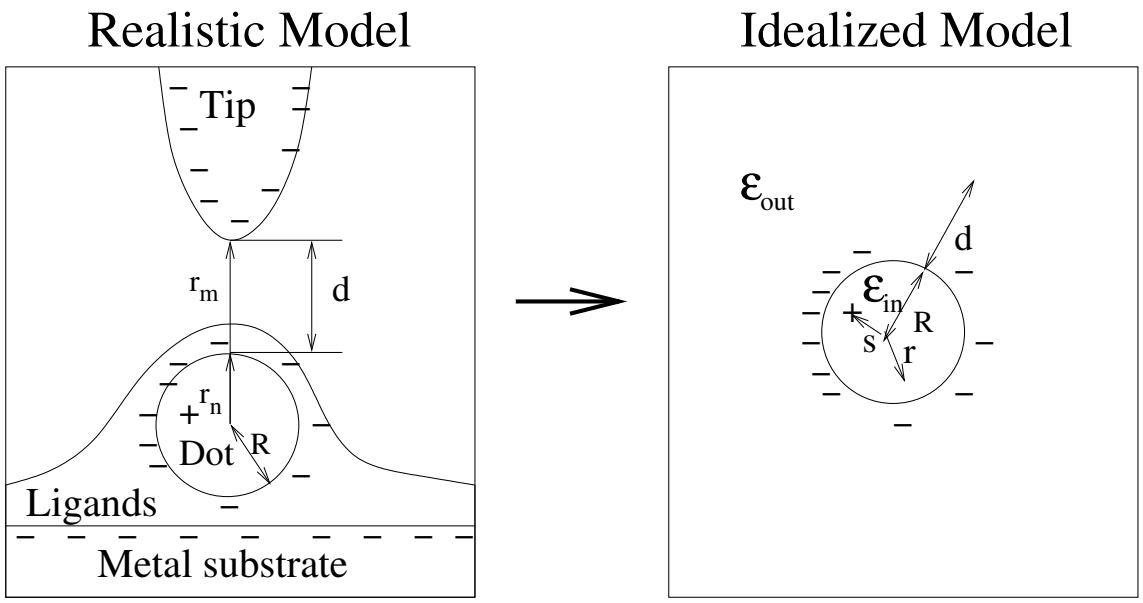

Figure 4.4: Schematic diagrams of the polarization of a charged quantum dot and the dot environment in a realistic and an idealized model. In the realistic model, the polarization strongly depends on the geometry of the dot environment such as the shape of the STM tip and ligands, and distances between these components. In the idealized model, the inhomogeneous dot environment is replaced with a uniform dielectric medium characterized by an effective dielectric constant ϵ_{out}.

with the dielectric function defined in Chap. 3.2. For $V^{\rm dir}(\mathbf{r};\mathbf{s})$, we replace $\epsilon_{\rm in}$ with $\epsilon(|\mathbf{r}-\mathbf{r}'|,R)$ to include the size and particle-separation dependence. For $V^{\rm pol}(\mathbf{r};\mathbf{s})$, we replace $\epsilon_{\rm in}$ with $\epsilon(\infty,R)$ to treat the dot as a uniform dielectric medium. Note that $\epsilon(|\mathbf{r}-\mathbf{r}'|,R)$ saturates to $\epsilon(\infty,R)$ as $|\mathbf{r}-\mathbf{r}'|$ approaches to ~ 2 Å. The dielectric constant $\epsilon_{\rm out}$ of the dot environment is adjusted to fit $\Delta^{\rm e}_{1,2}$ to an experimental value.

The three types of charging energies are calculated with charge densities given by the tight-binding wave function $\psi(\mathbf{r},\sigma)$ and with electrostatic potentials given by Eq. (4.8). First, the self-polarization energy results only from $V^{\rm pol}(\mathbf{r};\mathbf{s})$ because the source charge does not interact with itself. The self-polarization energy of a ith electron or hole is written as

$$\Sigma_i^{\rm pol} = \frac{e}{2}\sum_\sigma \int {\rm d}^3 r V^{\rm pol}(\mathbf{r};\mathbf{r})|\psi_i(\mathbf{r},\sigma)|^2, \tag{4.9}$$

where $\psi_i(\mathbf{r},\sigma)$ is the wave function of the ith electron or hole. Second, the Coulomb energy between a pair of electrons or holes is given by

$$J_{i,j} = e\sum_{\sigma\sigma'}\int {\rm d}^3 r_1 {\rm d}^3 r_2 V(\mathbf{r}_1;\mathbf{r}_2)|\psi_i(\mathbf{r}_1,\sigma)|^2|\psi_j(\mathbf{r}_2,\sigma')|^2. \tag{4.10}$$

The Coulomb energy has two components: the direct Coulomb energy attributed to $V^{\rm dir}(\mathbf{r};\mathbf{s})$ and the polarized Coulomb energy to $V^{\rm pol}(\mathbf{r};\mathbf{s})$. Finally, the electron-removal work function is approximated as

$$\begin{aligned} W_1 &= -e\sum_\sigma \int {\rm d}^3 r \left[V(\mathbf{r}_{\rm M};\mathbf{r}) - V(\mathbf{r}_{\rm N};\mathbf{r})\right]|\psi_{\rm h}(\mathbf{r},\sigma)|^2 \\ &\approx \frac{e^2}{\epsilon_{\rm out}}\left[\frac{1}{R}-\frac{1}{R+d}\right], \end{aligned} \tag{4.11}$$

where $\mathbf{r}_{\rm M}$ and $\mathbf{r}_{\rm N}$ are the position vector of the closest outer surface of the metal lead to the dot and that of the dot to the metal lead, respectively (see Fig. 4.4). The final equation is obtained by approximating the charge density of a hole with that

of a point charge e at the dot center and by ignoring higher order terms $\ell > 0$ of $V^{\rm pol}(\mathbf{r};\mathbf{s})$. The symbol d is the closest distance between the dot and the metal lead as shown in Fig. 4.4.

4.3 Zero-Current Energy Gap

One important physical value in the tunneling spectra is the spacing between the first conductance peaks in a positive and a negative bias-voltage sides, which is labeled as $E_{\rm gap}$ in Fig. 4.1. This spacing is called a zero-current energy gap since a tunneling current is suppressed within a voltage region between these two peaks. In the present model, the zero-current energy gap is the sum of the first electron and the first hole addition energies:

$$\begin{aligned} E_{\rm gap} &\equiv \mu_1^{\rm e} + \mu_1^{\rm h} \\ &= E_1^{\rm e} + E_1^{\rm h} + \Sigma_1^{\rm pol,e} + \Sigma_1^{\rm pol,h} + W_1. \end{aligned} \tag{4.12}$$

The zero-current energy gap differs from a single-particle energy gap by the sum of the electron and hole self-polarization energies and the electron-removal work function.

To calculate the charging energies, the effective dielectric constant $\epsilon_{\rm out}$ of the dot environment and the closest distance d between the STM tip and the dot are estimated. The dielectric constant $\epsilon_{\rm out}$ is determined by fitting $\Delta_{1,2}^e$ to the corresponding experimental value of an InAs dot with radius R=32 Å. The best fit of $\Delta_{1,2}^e$ is obtained with $\epsilon_{\rm out} = 4.5$. For d, we use the distance of the tip closest approach to the dot given by the length ($\sim$ 5 Å) of ligands surrounding the dot, since the accurate geometry of the STM setup is not available [28]. This approach provides the lower limit of the electron-removal work function.

Figure 4.5 presents the size dependences of the charging energies for the zero-current energy gaps and that of the gaps with dot radii ranging from 15 Å to 35 Å. Single-particle gaps contributing to the gaps range from 1.9 to 0.9 eV as the dot size increases, while total charging energies vary from 220 to 90 meV. Within the total charging energy, the electron and hole self-polarization energies are 80 to 40 meV each, and the work functions are 60 to 10 meV. The calculated zero-current gaps are compared with STM experimental gaps [28, 63]. As shown in Fig. 4.5(b), the calculated gaps agree well with the experiment for a full experimental range of InAs dot radii.

4.4 Electron and Hole Addition Energies

The electron and hole addition energies beyond the zero-current energy gap contain charge-carrier Coulomb energies and excited single-particle energies. The lowest electron level of InAs dots is two-fold, while the lowest hole level is four-fold. As a result, the first two tunneling electrons are assigned to the lowest electron level. Similarly, the first four tunneling holes are assigned to the lowest hole level. Therefore, the spacing between the first two electron addition energies and those between the first four hole addition energies are determined solely by the charging energies. In contrast, the third electron and the fifth hole addition energies contain the energies of the second lowest electron and hole levels in addition to charging energies, respectively. The third tunneling electron is assigned to the second lowest electron level since the lowest electron level is fully occupied by the first two tunneling electrons. Likewise, the fifth hole is assigned to the second lowest hole level. Therefore, the spacing between the second and third electron addition energies and that of the fourth

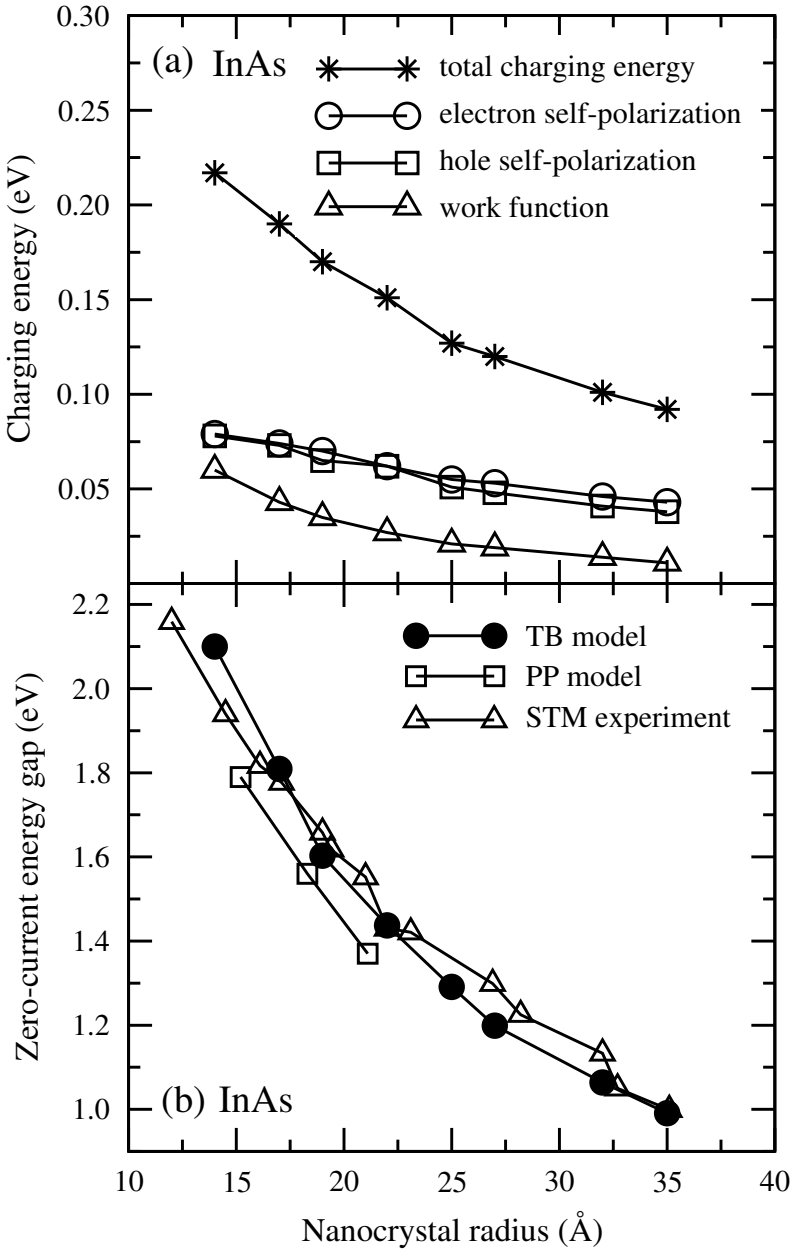

Figure 4.5: (a) Calculated charging energies for zero-current energy gaps versus InAs quantum dot radius R. (b) Zero-current energy gaps versus R. The size dependence of each component of the charging energy – electron and hole self-polarization energies and electron-removal work functions – is plotted. The zero-current gaps calculated with the present tight-binding (TB) model are plotted with respect to dot radius in comparison with those of pseudo-potential (PP) calculations [19] and STM experiments [28]. The present TB gaps are in good agreement with the experiment for a full range of dot radii (R=10–40 Å).

electron addition energy spacing	hole addition energy spacing
$\Delta^{\mathrm{e}}_{1,2} \approx J^{\mathrm{ee}}$	$\Delta^{\mathrm{h}}_{1,2} = \Delta^{\mathrm{h}}_{2,3} = \Delta^{\mathrm{h}}_{3,4} \approx J^{\mathrm{hh}} + W^{\mathrm{h}}_1$
$\Delta^{\mathrm{e}}_{2,3} \approx E^{\mathrm{e}}_3 - E^{\mathrm{e}}_2 + J^{\mathrm{ee}}$	$\Delta^{\mathrm{h}}_{4,5} \approx E^{\mathrm{h}}_5 - E^{\mathrm{h}}_4 + J^{\mathrm{hh}} + W^{\mathrm{h}}_1$

Table 4.1: Main contributions to addition energy spacings. The addition energy spacings are mainly determined by the Coulomb energy of one pair of charge carriers and a single-particle level spacing, since the variation of the self-polarization energies of different charge-carriers and that of the Coulomb energies of a different pair of charge-carriers are smaller than 10 meV. J^{ee} (J^{hh}) is the Coulomb energy of one pair of electrons (holes). $E^e_3 - E^e_2$ ($E^h_5 - E^h_4$) is the spacing between the first two lowest electron (hole) levels.

and fifth hole addition energies are the sum of the level spacing and the charging energies. The spacings between these low-lying electron and hole addition energies are listed in Table 4.1.

Calculated addition energy spacings for InAs dots with various radii are compared with those of STM experiments [28] in Fig. 4.6. The spacing $\Delta^e_{1,2}$ is in good agreement with the experiment. Note that only $\Delta^{\mathrm{e}}_{1,2}$ with dot-radius 32 Å is fitted to experiments to determine ϵ_{out}. This agreement indicates that the present model provides a good description of the Coulomb energy J^{ee}. The spacing $\Delta^e_{2,3}$ agrees with the experiment within a difference of less than 50 meV. This difference may result from the experimental uncertainties of dot size determinations [28]. The relatively good agreement in $\Delta^e_{2,3}$ shows that the second lowest electron level is well described by the $sp^3d^5s^*$ nearest-neighbor tight-binding model.

The spacing $\Delta^h_{1,2}$ is overestimated by ∼25 meV in the present model as shown in Fig. 4.6. The electron-removal work function may be the main cause of the small discrepancy in $\Delta^h_{1,2}$, since the work function is modeled with a simplified description

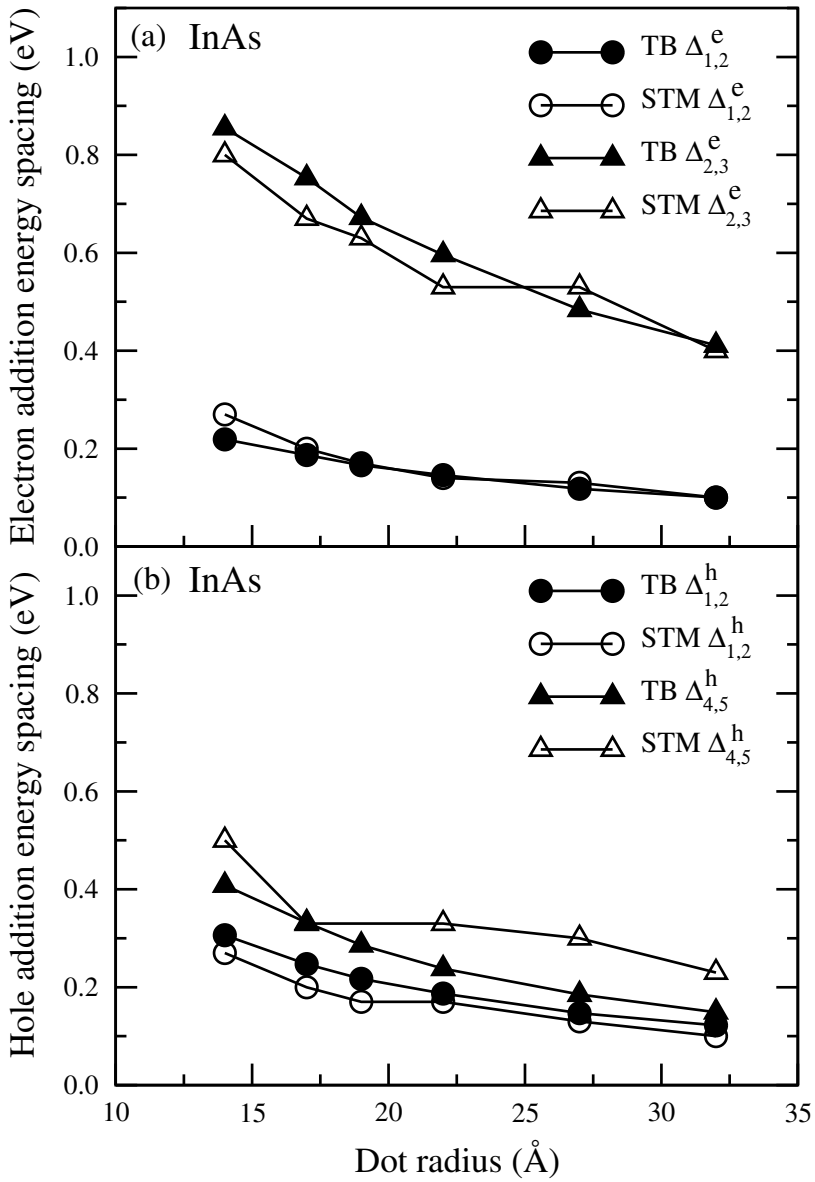

Figure 4.6: (a) Electron addition energy spacings $\Delta^{e}_{1,2}$ and $\Delta^{e}_{2,3}$ versus dot radius R. (b) Hole addition energy spacings $\Delta^{h}_{1,2}$ and $\Delta^{h}_{4,5}$ versus R. The spacings are calculated with Eqs. (4.5) and (4.6). The spacing $\Delta^{e}_{1,2}$ at R=32 Å is a fitted quantity to determine the effective dielectric constant ϵ_{out} of the dot environment. The best fit is obtained with $\epsilon_{\text{out}} = 4.5$. Addition energy spacings of STM experiments [28] are plotted for comparison.

of the dot environment, illustrated in Fig. 4.4. Unlike other types of charging energies, the work function requires a good description of the electrostatic potential in a region between the dot and the STM tip as shown in Eq. (4.11). To improve the work function, an electrostatic potential of the inhomogeneous dot environment shown in Fig. 4.4 needs to be calculated.

Figure 4.6(b) shows that the present model underestimates the spacing $\Delta^{\mathrm{h}}_{4,5}$ by $\sim$100 meV (30%). The charging energy of $\Delta^{\mathrm{h}}_{4,5}$ is the same as $\Delta^{\mathrm{h}}_{1,2}$, and the charging energy agrees with the experiment within an error of only a few tens of meV. Therefore, the big discrepancy in $\Delta^{\mathrm{h}}_{4,5}$ is attributed to the underestimation of the spacing between the two lowest hole levels.

4.5 Discussion

In this chapter, we studied the quantum confinement and charging effects on the transport properties of quantum dots by modeling the electron and hole addition energies of InAs dots. The electron and hole addition energies consist of the single-particle energies of the dots and the charging energies of single-electron transfer. The charging energies are described in terms of (i) self-polarization energies, (ii) Coulomb energies of excess charges, (iii) electron-removal work functions. Calculated zero-current gaps, electron addition energies, and the first four hole addition energies are in good agreement with STM experiments [28] within 10% error. However, the present model underestimates the fifth hole addition energies by $\sim$100 meV, yielding a 25% discrepancy with experimental values. This underestimation indicates that the hole effective masses of bulk InAs in the present model are heavier than those of the real material.

The discrepancy in the fifth hole addition energy partly results from the perturbative treatment of charging energies and the neglect of an external electric field in the present model. The effects of charging and the external electric field on the single-particle levels are ignored in the present and other models [19, 22]. Those models assume that the single-particle levels of charged dots in an applied electric field are the same as those of uncharged, unperturbed dots. The charging and electric field effects are expected to be larger on higher addition energies which involve more excess-charge-carriers and stronger electric fields. This expectation is consistent with our results that show good agreement for zero-current gaps and several low-lying addition energies with experiments but disagreement for the fifth hole addition energy.

CHAPTER 5

CONCLUSIONS

My books are water; those of the great geniuses are wine. (Fortunately) Everybody drinks water. -Mark Twain

This work demonstrated the success of the tight-binding model for describing the many-body levels of optically excited and multiply charged quantum dots. First, the calculated lowest exciton energies of Si and CdSe dots with 10–40 Å radius are in good agreement with photoluminescence experiments within a less than 5% error (see Figs. 3.8 and 3.10). Second, the calculated three lowest bright-exciton energies of InAs dots with 20–40 Å radius show good agreement with photoluminescence excitation experiments within a 5% error (see Fig. 3.15). Third, calculated several low-lying electron and hole addition energies of InAs dots with 10–40 Å radius agree with scanning tunneling microscope experiments within a 10% error (see Figs. 4.5 and 4.6).

In contrast to the success, the present tight-binding model does not agree well with experiments for two following quantities. First, the bright exciton energies of InAs dots with radius $R < 20$ Å are overestimated by as much as 0.5 eV or 25% (see Fig. 3.15). The calculated exciton energies scale as $R^{-0.8}$, while the experimental data

scale as R^{-n} with $n \sim +0$. Hence, the calculated exciton energies rapidly increase with decreasing the dot radius, yielding bigger discrepancies with experimental energies. Second, the spacing between the fourth and fifth hole addition energies of InAs dots with all radii (10-40 Å) considered in this work is underestimated by 0.1 eV or 30% (see Fig. 4.6). Experimental uncertainties of size determinations [64] and bias-voltage drop distributions [65, 66] make it difficult to identify the main causes of the disagreements. Despite the difficulty, we focus on the possible causes of the disagreements resulting from the limits of the present model, and point out the ways to improve the model for future work. The discrepancies between our model and the experiments can be explained by three possible reasons.

First, surface reconstruction and surface chemistry become important as quantum-dot sizes cross from the mesoscopic scale to the molecular scale. The effects are excluded in the present model as we model the dot as a perfect zinc-blende structure with all dangling bonds at the surface terminated. Tight-binding studies for CdSe quantum dots show that the inclusion of the surface reconstruction decreases the lowest bright-exciton energy by 100 meV for a dot with radius 12 Å [67]. Moreover, recent first-principle calculations for Si nanoclusters show that imperfect surface passivation can reduce the gap by as much as 1.6 eV [15]. Since the better surface descriptions reduce excition energies, including surface reconstruction and realistic surface passivation can improve the excition energies of small InAs dots, which are overestimated by the present model.

Second, the transferability of bulk tight-binding parameters to describe the single-particle Hamiltonian of quantum dots is limited within the present model due to the difference between local charge densities of the dot and the bulk. The present model

uses bulk parameters, which are fitted to bulk band structures, without correcting them for quantum dots with respect to the change of the local charge density. The density change arises from the difference between ionic potentials near the dot surface and those in the bulk. Therefore, the density difference between the dot and the bulk becomes larger as the ratio of surface to volume increases. Making the parameters a functional of the charge density and achieving the self-consistency of the charge density and the parameters improve the transferability for the tight-binding model to describe solids with impurities, dislocations, and defects [68]. The same scheme can be applied to improve the single-particle Hamiltonian of quantum dots.

Third, the single-particle levels of charged dots with an electric field applied are different from those of uncharged dots in the absence of an electric field. The differences are neglected within the present model and other models [19, 22]. Self-consistent calculations of single-particle levels in the presence of excess charges and an applied electric field are needed to resolve the charging and the electric field effects on the single-particle levels.

The success of the tight-binding model to describe the many-body levels of relatively large chemically synthesized dots suggests that the tight-binding model can quantitatively describe the optical and transport properties of larger quantum dots such as self-assembled dots and vertical dots. The present model for electron-hole interactions, electron-hole dipole moments, and charging energies, which are incorporated into the tight-binding model, can be extended to study the properties of the large dots. The suitability of the tight-binding model for describing small dots remains unresolved. Our results suggest that local effects, such as surface relaxation

and the change of local charge densities, must be included more carefully as the dot size crosses from the mesoscopic scale to the molecular scale.

APPENDIX A

ELECTRON AND HOLE LEVELS

This appendix presents how to connect single-particle energies (E_i) and wave functions ($|\psi_i\rangle$) obtained by diagonalizing the effective single-particle Hamiltonian (Eq. 2.1) to electron and hole energies (E_e and E_h) and wave functions ($|e\rangle$ and $|h\rangle$) which are used in the modeling of exciton levels and electron and hole addition energies. The electron level is the level with one electron added into the dot, while the hole level is that with one electron removed from the dot. Therefore, the electron and hole levels can be described by the single-particle levels with its energy higher and lower than a Fermi energy. The Fermi energy of undoped semiconductors is somewhere in the gap between the highest valence band and lowest conduction band.

By dividing the single-particle levels into two groups with respect to the Fermi energy E_F, the electron and hole energies and wave functions are defined as

$$|\mathrm{e}\rangle = |\psi_i\rangle \text{ and } \mathrm{E_e} = \mathrm{E_i}, \text{ if } \mathrm{E_i} > \mathrm{E_F} \tag{A.1}$$

$$|\mathrm{h}\rangle = |\overline{\psi_i}\rangle \text{ and } \mathrm{E_h} = -\mathrm{E_i}, \text{ if } \mathrm{E_i} < \mathrm{E_F}, \tag{A.2}$$

where $|\overline{\psi_i}\rangle$ is related to $|\psi_i\rangle$ as follows.

$$\langle \mathbf{r}, \sigma | \overline{\psi_i} \rangle = \langle \mathbf{r}, -\sigma | \psi_i \rangle^*. \tag{A.3}$$

The hole wave function is the conjugate of the corresponding single-particle wave function with its spin opposite to the single-particle's spin. This relation is based on the second quantization theory where a hole state is a state resulting from an annihilation operator applied to an occupied level[69].

Within the tight-binding model, the electron and hole wave functions are linear combinations of tight-binding basis orbitals $|i\gamma\sigma\rangle$:

$$|e\rangle = \sum_{i\gamma\sigma} c_{e;i\gamma\sigma}|i\gamma\sigma\rangle, \tag{A.4}$$

$$|h\rangle = \sum_{i\gamma\sigma} c_{h;i\gamma\sigma}|\overline{i\gamma\sigma}\rangle, \tag{A.5}$$

where

$$\langle \mathbf{r}, \sigma|\overline{i\gamma\sigma}\rangle = \phi^*_{i\gamma}(\mathbf{r})\chi^*_{-\sigma}. \tag{A.6}$$

The function $\phi_{i\gamma}(\mathbf{r})$ is a tight-binding basis orbital centered at atomic site i and with orbital type γ, while χ_σ is a spin state, respectively. The coefficients c_{e} and c_{h} describe global variations of the wave functions from one atomic site to another atomic site, while the tight-binding basis orbitals $|i\gamma\sigma\rangle$ and $|\overline{i\gamma\sigma}\rangle$ describe local variations of the wave functions near one atomic site.

BIBLIOGRAPHY

[1] L. E. Brus. *J. Chem. Phys.*, 80:4403, 1984.

[2] M. A. Kastner. *Phys. Today*, 46:24, 1993.

[3] A. P. Alivisatos. *Science*, 271:933, 1996.

[4] D. Bimberg, M. Grundmann, and N. Ledentsov, editors. *Quantum Dot Heterostructures*. Wiley, Chichester, 1998.

[5] D. L. Klein, R. Roth, A. K. L. Lim, A. P. Alivisatos, and P. L. McEuen. *Nature*, 389:699, 1997.

[6] S. Tarucha, D. G. Austing, T. Honda, R. J. van der Hage, and L. P. Kouwenhoven. *Phys. Rev. Lett.*, 77:3613, 1996.

[7] P. G. Eliseev, H. Li, A. Stintz, G. T. Liu, T. C. Newell, K. J. Malloy, and L. F. Lester. *Appl. Phys. Lett.*, 77:262, 2000.

[8] H. Drexler, L. Leonard, W. Hansen, J. P. Kotthous, and P. M. Petroff. *Phys. Rev. Lett.*, 73:2252, 1994.

[9] T. Lundstrom, W. Schoenfeld, H. Lee, and P. M. Petroff. *Science*, 286:2312, 1999.

[10] S. Kim, H. Mohseni, M. Erdtmann, E. Michel, C. Jelen, and M. Razeghi. *Appl. Phys. Lett.*, 73:963, 1998.

[11] P. Michler, A. Kiraz, C. Becher, W. V. Schoenfeld, P. M. Petroff, L. Zhang, E. Hu, and A. Lmamoglu. *Science*, 290:2282, 2000.

[12] E. Biolatti, R. C. Iotti, P. Zanardi, and F. Rossi. *Phys. Rev. Lett.*, 85:5647, 2000.

[13] F. Pederiva, C. J. Umrigar, and E. Lipparini. *Phys. Rev. B*, 62:8120, 2000.

[14] S. Ogut Igor Vasiliev and J. R. Chelikowsky. *Phys. Rev. Lett.*, 85:5647, 2000.

[15] A. Puzder, A. J. Williamson, J. C. Grossman, and G. Galli. *Phys. Rev. Lett.*, 88:97401, 2002.

[16] Al. L. Efros and M. Rosen. *Annu. Rev. Mater. Sci.*, 30:475, 2000.

[17] R. Sakhel, L. Jönsson, and J. W. Wilkins. *Phys. Rev. B*, 64:155322, 2001.

[18] A. J. Williamson and A. Zunger. *Phys. Rev. B*, 61:1978, 2000.

[19] A. Franceshetti and A. Zunger. *Phys. Rev. B*, 62:2614, 2000.

[20] K. Leung and K. B. Whaley. *Phys. Rev. B*, 56:7455, 1997.

[21] G. Allan, Y. M. Niquet, and C. Delerue. *Appl. Phys. Lett.*, 77:639, 2000.

[22] Y. M. Niquet, C. Delerue, M. Lannoo, and G. Allan. *Phys. Rev. B*, 64:113305, 2001.

[23] S. Lee, L. Jönsson, J. W. Wilkins, G. W. Bryant, and G. Klimeck. *Phys. Rev. B*, 63:195318, 2001.

[24] S. Fafard, M. Spanner, J. P. McCaffrey, and Z. R. Wasilewski. *Appl. Phys. Lett.*, 76:2268, 2000.

[25] C. B. Murray, D. J. Norris, and M. G. Bawendi. *J. Am. Chem. Soc.*, 115:8706, 1993.

[26] U. Banin, C. J. Lee, A. A. Guzelian, A. V. Kadavanich, A. P. Alivisatos, W. Jaskolski, G. W. Bryant, Al. L. Efros, and M. Rosen. *J. Chem. Phys.*, 109:2306, 1998.

[27] D. J. Norris and M. G. Bawendi. *Phys. Rev. B*, 53:16338, 1996.

[28] U. Banin, Y. Cao, D. Katz, and O. Millo. *Nature*, 400:542, 1999.

[29] E. P. A. M. Bakkers and D. Vanmaekelbergh. *Phys. Rev. B*, 62:R7743, 2000.

[30] L. Goldstein, F. Glas, J. Y. Marzin, M. N Charasse, and G. L. Roux. *Appl. Phys. Lett.*, 47:1099, 1985.

[31] M. Kuno, J. K. Lee, B. O. Dabbousi, F. V. Mikulec, and M. G. Bawendi. *J. Chem. Phys.*, 106:9869, 1997.

[32] E. P. A. M. Bakkers, Z. Hens, Z. Zunger, A. Franceschetti, L. P. Kouwenhoven, L. Gurevich, and D. Vanmaekelbergh. *Nano Letters*, 1:551, 2001.

[33] J. M. Luttinger. *Phys. Rev.*, 102:1030, 1956.

[34] C. R. Pidgeon and R. N. Brown. *Phys. Rev.*, 146:575, 1966.

[35] A. Franceshetti, H. Fu, L. W. Wang, and A. Zunger. *Phys. Rev. B*, 60:1819, 1999.

[36] P. Vogl, H. P. Hjalmarson, and J. D. Dow. *J. Phys. Chem. Solds.*, 44:365, 1983.

[37] Otfried Madelung, editor. *Semiconductors-Basic Data*. Springer, New York, 2nd revised ed. edition, 1996.

[38] G. Klimeck, R. C. Bowen, T. B. Boykin, C. Salazar-Lazaro, T. A. Cwik, and A. Stoica. *Supperlattice Microst.*, 27:77, 2000.

[39] This algorithm uses an analogy between optimizing the multi-dimensional tight-binding parameters and finding the optimal genes of species through biological evolutions and selections over many generations.

[40] J.-M. Jancu, R. Scholz, F. Beltram, and F. Bassani. *Phys. Rev. B*, 57:6493, 1998.

[41] W. A. Harrison. *Electronic Structure and the Properties of Solids*. W. H. Freeman and Company, 1980.

[42] P. E. Lippens and M. Lannoo. *Phys. Rev. B*, 41:6079, 1990.

[43] F. Reboredo, A. Franceschetti, and A. Zunger. *Appl. Phys. Lett.*, 75:2972, 1999.

[44] L.-W. Wang and A. Zunger. *J. Phys. Chem.*, 102:6449, 1998.

[45] R. Magri, S. Froyen, and A. Zunger. *Phys. Rev. B*, 44:7947, 1991.

[46] A. Franceshetti, L. W. Wang, H. Fu, and A. Zunger. *Phys. Rev. B*, 58:13367, 1998.

[47] E. Martin, C. Delerue, G. Allan, and M. Lannoo. *Phys. Rev. B*, 50:18258, 1994.

[48] R. Resta. *Phys. Rev. B*, 16:2717, 1977.

[49] D. R. Penn. *Phys. Rev.*, 128:2093, 1962.

[50] R. Tsu, L. Ioriatti, J. Harvey, H. Shen, and R. Lux. volume 283. Materials Research Society, Pittsburgh, 1993.

[51] J. C. Slater. *Phys. Rev.*, 36:57, 1930.

[52] K. Ohno. *Theor. Chim. Acta*, 2:219, 1964.

[53] MOLPRO is a package of ab initio programs written by H.-J. Werner and P.J. Knowles, with contributions from R. D. Amos, A. Bernhardsson, A. Berning, P. Celani, D.L. Cooper, M.J.O. Deegan, A.J. Dobbyn, F. Eckert, C. Hampel, G. Hetzer, T. Korona, R. Lindh, A.W. Lloyd, S.J. McNicholas, F.R. Manby, W. Meyer, M.E. Mura, A. Nicklass,P. Palmieri, R. Pitzer, G. Raubut, M. Schütz, H. Stroll, A.J. Stone, R. Tarroni, and T. Thorsteinsson. The integral evaluation (SEWARD) is described in R. Lindh, U. Ryu, and B. Liu, J.Chem.Phys.95, 5889 (1991).

[54] We can obtain only unscreened integrals in the quantum chemistry packages[53], since there is no way to include a spatially varying screening function.

[55] P. J. Hay and W. R. Wadt. *J. Chem. Phys.*, 82:270, 1985.

[56] T. Takagahara. *Phys. Rev. B*, 47:4569, 1993.

[57] A. Franceschetti and A. Zunger. *Phys. Rev. Lett.*, 78:915, 1997.

[58] To be clear about this notation, 's-like hole' means that the coefficients of the p basis orbital has s symmetry in real space over the whole dot, whereas 'p-like hole' means that the coefficients of the p basis orbital has p symmetry. For electron states, the coefficients of the s basis orbital are used to label the wave functions. For example, 's-like electron' means that the coefficients of the s basis orbital has s symmetry, while 'p-like electron' has p symmetry in the coefficients of the s orbital.

[59] W. H. Press, S. A. Teukolsky, W. T. Vetterling, and B. P. Flannery. *Numerical Recipes in C: The Art of Scientific Computing.* Cambridge Unversity Press, 2nd ed. edition, 1999.

[60] M. V. Wolkin, J. Jorne, P. M. Fauchet, G. Allan, and C. Delerue. *Phys. Rev. Lett.*, 82:197, 1999.

[61] Within the tight-binding model including spin-orbit coupling, the dipole moment is a complex number since electron and hole wave functions are complex functions.

[62] L. Banyai, P. Gilliot, Y. Z. Hu, and S. W. Koch. *Phys. Rev. B*, 45:14136, 1992.

[63] Banin *et al.* claim that the STM tips are retracted from the nanocrystal far enough to make most of the bias-voltage drop across a tip-nanocrystal junction (J1). Therefore, we approximate the voltage drop across J1 with the total bias voltage, that is the upper limit of the voltage drop across J1.

[64] In the PLE experiment, its size measurement with transmission electron microscopy (TEM) may underestimate a nanocrystal radius by approximately 2.5 Å, because TEM is insensitive to a non-periodic layer near the nanocrystal surface [26]. In the STM experiment, STM topographic images may overestimate a nanocrystal size due to the tip-nanocrystal convolution effect [28].

[65] D. Katz, O. Millo, S.-H. Kan, and U. Banin. *Appl. Phys. Lett.*, 79:117, 2001.

[66] Katz *et al.* [65] estimate that the ratio of the voltage drop across J1 to that across J2 is approximately 10 (see the inset of Fig. 4.1 for the definitions of J1 and J2). This estimation is based on the analyses with theoretical tunneling simulations combined with pseudo-potential calculations [18] for single-particle levels, but not based on the experimental measurements, for instance, the capacitances and resistances of J1 and J2. Therefore, the STM measurements without the information on the voltage drop distributions should be considered to have a few tens of percent of uncertainties.

[67] K. Leung and K. B. Whaley. *J. Chem. Phys.*, 110:11012, 1999.

[68] F. Liu. *Phys. Rev. B*, 52:10677, 1995.

[69] A. L. Fetter and J. D. Walecka. *Quantum Theory of Many-Particle Systems*. McGraw-Hill, Inc., 1995.